ABSTRACT

Title of dissertation: A CONTINUUM MODEL FOR FLOCKING: OBSTACLE AVOIDANCE, EQUILIBRIUM, AND STABILITY

Nicholas Alexander Mecholsky,
Doctor of Philosophy, 2010

Dissertation directed by: Professor Edward Ott
Department of Physics

The modeling and investigation of the dynamics and configurations of animal groups is a subject of growing attention. In this dissertation, we present a partial-differential-equation based continuum model of flocking and use it to investigate several properties of group dynamics and equilibrium.

We analyze the reaction of a flock to an obstacle or an attacking predator. We show that the flock response is in the form of density disturbances that resemble Mach cones whose configuration is determined by the anisotropic propagation of waves through the flock.

We investigate the effect of a flock 'pressure' and pairwise repulsion on an equilibrium density distribution. We investigate both linear and nonlinear pressures, look at the convergence to a 'cold' ($T \to 0$) equilibrium solution, and find regions of parameter space where different models produce the same equilibrium.

Finally, we analyze the stability of an equilibrium density distribution to long-wavelength perturbations. Analytic results for the stability of a constant density

solution as well as stability regimes for constant density solutions to the equilibrium equations are presented.

A CONTINUUM MODEL FOR FLOCKING: OBSTACLE AVOIDANCE, EQUILIBRIUM, AND STABILITY

by

Nicholas Alexander Mecholsky

Dissertation submitted to the Faculty of the Graduate School of the
University of Maryland, College Park in partial fulfillment
of the requirements for the degree of
Doctor of Philosophy
2010

Advisory Committee:
Professor Edward Ott, Chair/Advisor
Professor Thomas Antonsen
Professor Parvez Guzdar
Professor Michelle Girvan
Professor Brian Hunt

Preface

In this dissertation, I consider aspects of flocking — or swarm — theory. It is a relatively new field, and it is my belief that the main ideas remain undiscovered. One very influential idea that *has* been identified, and permeates the field, is that of behavioral modeling. Using behavioral modeling, researchers have a paradigm through which questions may be attacked. In this dissertation, we investigate the specific questions of obstacle avoidance, equilibria solutions, and stability within the framework of a continuum model.

I do not produce a perfect, general answer to these problems, but rather, I provide a direction toward attacking some of these issues. The utility of this dissertation is as a guide to possible methods of answering questions related to flocking. It is through the use of a specific model, with specific predictions, that general results may be investigated and predicted. It is through general, model-independent results that progress can be made in understanding the true relationships of this field.

Dedication

To my wife, Shaela, my son, Roman, and to my parents, Jack and Sue. Through their love and support they have made this thesis possible.

Acknowledgments

I would first like to thank my advisors Ed Ott and Tom Antonsen. Through their patient guidance, I have learned more in graduate school than I ever thought possible. I appreciate the valuable opportunity they have given me to work with them. They always made time for my many needs, and forced me to be precise and organized when talking to them and other scientists. The lessons I have learned will last me a lifetime.

Dr. Parvez Guzdar has been very patient and understanding in his many hours of conversation regarding numerical methods of computational physics. I appreciate the respect that he showed for me and I hope my questions weren't too much of a burden.

I would also like to thank Professors Girvan, and Hunt for agreeing to be on my thesis committee and for their careful reading of my thesis. I appreciate the time they have given to attend to my research.

In the many interactions with graduate students at the University of Maryland, I have gained about as much experience and insight as I did from my research. My office mates Matt Cornick, Young-noh Yoon, and James Hart have had the most influence on my academic thinking. It has been through their many questions, problems, and comments that I have made the most progress. I would like to thank Andy Pearson for listening to my many side projects; Francesco Sorrentino for his engaging scientific style; Kyle Gustafson and Chris Stark for their grounded attitude toward science and sense of humor; Andy Yorke and Ben Cooper for their inspira-

tional and inspired conversations and ideas; Andrew Pomerance and Colin McCaan for their intelligence and high scientific standards; Tommy Willis for his enthusiastic approach to everything he does; Matt Beeler for his quiet, collected demeanor; John Platig and Kimbie Glass for their friendship and conversations; Tom Bing, Renee Michelle Goertzen, Rolando Valdes Aguilar and Beatriz Burrola, and Mattie Lau and Jonathan Goldstein for their weekly anticipated Star Trek/beer/social gathering; Ryan Artuso for his interesting conversations; Tracy Moore for her friendship and unique perspectives on graduate school; Ellie and Kevin Twedt for the many times they have had us over for dinner; David Norris for his sushi and music, Will Ray and Chris Danforth for their conversations and example; Jonathon Ozik, Seungyoung Baek, and Juan Restrepo for their encouragement and advice; and finally my friend Ben Wall for many interesting hours of fixing his car, discussing everything, and not beliving anything I say unless I could prove it.

Additionally, I would like to thank Ed Condon, Janet Wolfsheimer, Mohini Kaul for their many favors and assistance, Dr. Raj Roy, for the nice discussion about scientific careers, and Dr. Bill Dorland, Dr. Margetis, Dr. Bill Goldman, and Dr. Howard Elman for showing me many tips, tricks, and for many great interactions with these excellent educators.

Finally, I would like to acknowledge and thank the kind, cheerful, and caring support of Jane Hessing. Her under-appreciated help has saved many graduate students from the perils of the University administrative system. Her genuine concern for each of the students she helps is very clear and very refreshing.

The people to whom I owe the most gratitude are my wife, Shaela, and my

son, Roman. They have supported me, encouraged me, and sacrificed for me my entire graduate career. In Roman's case, it has been his entire life! I also owe much to my father, Jack, mother, Susan, brothers Kristopher and John and their families, my sister, Sarah, and my Grandmother. They have been instrumental in shaping the person that I am. Their constant support has made this possible. They are the foundation and inspiration of my life and what I am I owe to them.

It is impossible to remember all, and I apologize to those I've inadvertently left out. My life truly is affected by all around me, and it is not always clear how to distinguish the effect in my experience from the cause.

Lastly, I would like to thank God for my life and for the opportunity I have been given to grow in the past six years.

Table of Contents

List of Figures

Chapter 1

Introduction

1.1 Group Dynamics

Groups of autonomous organisms, interacting with each other and the environment, can produce collective behavior. There are many examples in nature. Flocks of birds, schools of fish, herds of quadrupeds, swarms of insects, bacterial colonies, and crowds of people are just some of the many examples of this type of phenomenon [28, 5, 35, 17, 44, 14, 4, 45]. Even collections of certain robots and unmanned aerial vehicles (UAVs) can exhibit this behavior by design or sometimes as an unexpected consequence of underlying programming [19]. In this discussion, we refer to each of these groups as 'flocks'. Even though this type of group behavior may have always existed, it has been only recently that scientists outside of biology have turned their attention to flocks. Mathematical biologist have been modeling group dynamics for many years, most notably Akira Okubo [30, 31], but it seems that only recently have physicists and engineers been interested in the basic questions of flocking. Perhaps a key paper to throw light on this phenomenon from a more abstract perspective was a paper by a computer scientist, Craig Reynolds, interested in producing animations of realistic flocks of birds. In his paper, Reynolds [36] used the familiar concept —to mathematical biologists, anyway— of a behavioral force to produce the dynamics of his flocks. Three 'steering behaviors', separation, alignment, and cohesion, allowed

the individuals of his flock to avoid close neighbors, move in a common direction, and keep the collective from breaking apart. This initial model started a wave of interest in several fields; physics, mathematical biology, and engineering, to name a few. Each of these areas had their own perspective on the problem and importance of group dynamics. There were, and are still, many questions to be answered. What types of flocks can be formed? What determines when the flock will break apart? What forces or behaviors are necessary for flocking? How can we predict the behavior of groups just knowing the individual's behavior? How will the flock respond to an obstacle or a predator? This dissertation is a partial answer to the first and last questions.

In the decade after Reynolds' paper, seminal papers in mathematical biology, physics, and engineering were published to answer some of these questions. Tomas Vicsek, et al. [43], a group of physicists, simulated autonomous agents in a two-dimensional geometry and added noise to the trajectories of individual agents to find a phase transition from a flock to scattered individuals. Iain Couzin, et al. [7], produced a phase diagram that predicted four types of flocks in his model; a 'swarm', a 'torus', a 'dynamic parallel group', and the 'highly parallel group'. The paper further described that by changing the parameters of the basic laws that produced the flock, a flock may be able to transition between types of flocks. Hence, by changing the individual's local behavior, the global behavior might be modified. Other papers in physics [8, 25, 9, 2, 40, 43, 12, 33], mathematical biology [7, 15], and engineering [20, 38, 16, 35, 24, 29], provided answers to some questions and opened plenty of other questions using a variety of approaches to modeling flock behavior.

Since then, papers on many other areas related to collective behavior have appeared. However, even with all of this work, we are still far from a theory that unifies it all. With many different fields come many different notations, perspectives, and directions. Even within the field of physics, there are many approaches to modeling flocking.

1.2 Approaches to Modeling Flocking Behavior

There are several important classifications for flock modeling, two of which are

1. Discrete vs. Continuous

2. Stochastic vs. Deterministic

We will discuss these classifications briefly below. In the first case, there are two main approaches to flocks modeling: discrete models, and continuum models. Both are important for the full description of flocking, but they involve very different paradigms and can answer different questions.

In discrete models, each individual is given its own position and velocity. Some examples of discrete modeling can be seen in [30, 36, 43, 7]. There is a finite number of individuals. This makes it relatively straight-forward to simulate. Additionally, since real flocks have discrete members, it is more realistic than a continuum approach. However, there are some drawbacks to discrete models. Large flocks are computationally difficult to simulate. Also, for most models, a simulation run needs specific parameters. Initial conditions must be chosen, and, depending on the application, a large number of simulations must be undertaken. For example, in [7]

each point in the parameter-space phase diagram needed to be averaged over 30 separate runs of random initial condition that would eventually settle down to a specific equilibrium. Continuum models mitigate some of these problems.

Continuous models have the distinct disadvantage that taking the continuum limit is an abstraction from the real case of discrete flock members. However, models that are continuous in space as well as time provide a framework for studying flocking that allows much work to be done at once. The continuum description economically treats very large numbers of individuals and is, in some cases, easier to manipulate analytically than the discrete description. Some examples of this type of model can be found in [39, 42, 25]. This dissertation will adopt the continuum perspective.

Another major classification between models is the introduction or exclusion of stochastic terms. In a continuum description, stochastic terms necessitate more complicated and cumbersome mathematical machinery than a deterministic description. Okubo et al., in [31], provide the example of swarming mosquitoes that shows that the stochastic paradigm was present from the earliest mathematical models. The seemingly random flight paths are not in fact completely random since random paths would disperse the swarm, whereas a mosquito swarm can persist for quite a long time. They conclude that an "unknown factor operates against the power of diffusion" to produce statistically stationary swarms. Most randomness enters through an assumption of the individuals behavior, for example in [43, 27]. Either the individual has imperfect faculties or it has an imperfect locomotion, accounted for by adding some noise to the model. It would seem that stochasticity is a fundamental part of any biological flock. However, Chapter 3 investigates velocity

dispersion that is the result of a pressure-like term in the continuum model, which creates stochastic effects without the use of stochastic terms. Thus even though randomness might be an integral part of an individual, it may not mean that stochastic differential equations are necessarily needed. Thus, the models developed in this dissertation will be deterministic.

1.3 Outline of Dissertation

Chapter 2 will investigate obstacle avoidance of a flock using a continuum model and identify the key features avoidance. Our goal in this chapter is to provide some model independent features through which we can understand obstacle avoidance. To accomplish this, we first identify the dispersion relation of waves through this model to identify the modes by which information may be propagated. Using a construction analogous to the Mach construction for supersonic flows, we derive a simple result that provides basic information about the avoidance event. Numeric and analytic work provide a solid foundation for this prediction which is relatively independent of parameters. Because of the insensitivity to the parameters, we may conclude that the result is more universal than our original model that it came from.

Chapter 3 investigates the affect of a repulsive potential and pressure terms in a model for flocking. First, with the pressure term off, but a repulsive potential added to an attractive potential, a flock with a finite extent is found analytically. A parameter space for this type of equilibrium is identified. Finally, the equilibria

for a model with a non-zero temperature (a finite pressure) is found and shown to limit to the case of the localized zero-temperature (no pressure) solution.

Chapter 4 compares a theory of a linear pressure with a repulsive potential to a theory with a nonlinear pressure and no repulsive potential. The goal of this chapter is to begin to identify the key features of comparing different models. The equilibria for a linear pressure theory with both attractive and repulsive potentials and a nonlinear pressure theory with only an attractive term are examined. A general procedure that fits both models is presented, and it is claimed that a general class of models can be analyzed with this approach. Finally a comparison between the equilibria of the nonlinear and linear models is completed to identify parameters where both models produce the same equilibria.

Chapter 5 investigates stability of equilibria. Through the full dispersion relation, we are able to do a linear stability analysis to investigate which constant density solutions are unstable to long-wavelength perturbations. Finally, the non-constant density solutions of the model are briefly analyzed. A numerical scheme is developed to check the analytic work throughout the chapter.

Chapter 2

Obstacle and Predator Avoidance by a Flock

2.1 Introduction

In this chapter, we will consider the response of a flock to a stationary or moving 'obstacle'. In the case of a moving obstacle, our considerations might also be considered as modeling the avoidance response of a flock to a predator. Past research investigating obstacle avoidance has employed a discrete approach [36, 23, 22, 49]. As compared to a discrete description, the continuum description has the advantage of economically treating very large numbers of individuals and is, in some cases, easier to treat analytically and to interpret. Its disadvantage is primarily that taking the continuum limit is an abstraction from the real case of discrete flock members.

The current chapter introduces a moving obstacle into a large flock and studied the effect of this obstacle on the flow around the obstacle. We model the obstacle as a localized region exerting a repulsive 'pseudo-force' on the flock continuum. Using our description, we are able to describe the propagation of information in terms of a few parameters in the model. To do this, we use a fluid characterization of a flock. For a review of this type of approach, as well as other approaches to modelling flocks, see [39].

To facilitate our analysis we will utilize a linearized theory in which the flock response to the obstacle/predator pseudo-force is assumed to be proportional to

the pseudo-force strength. That is, the obstacle/predator is treated as a linear perturbation. Results obtained through this type of analysis are expected to yield qualitative insights to the dynamics of the full nonlinear problem, and may also yield quantitative understanding in the region far enough from the obstacle/predator where the perturbations become small. In the next section, we will introduce our continuum description of the flock. In the following sections, we explore the small amplitude wave dispersion relation and derive an expression for the disturbances that propagate through the flock. Next, a linearized response is investigated and the resulting density perturbation is analyzed analytically. Finally, results of numerical evaluation of the density perturbation are presented and compared to the theory.

2.2 Continuum Flocking Equations

The equations we consider for flocking in three dimensions are

$$\frac{\partial \mathbf{v}}{\partial t} + \mathbf{v} \cdot \nabla \mathbf{v} = \frac{1}{\tau}\left(1 - \frac{v^2}{v_0^2}\right)\mathbf{v} - \frac{1}{\rho}\nabla P(\rho) - \nabla U - \mathbf{W}(\mathbf{v}) \tag{2.1}$$

$$\frac{\partial \rho}{\partial t} + \nabla \cdot (\rho \mathbf{v}) = 0, \tag{2.2}$$

where ρ is the number density of flocking individuals, $\mathbf{v}$ is the macroscopic vector velocity field of the flock, v is its magnitude, and v_0 and τ are constants. The basic structure of these partial-differential equations includes terms that define the acceleration of the fluid density of the flock, along with continuity of flock members. The right-hand side of Eq. (2.1) consists of four 'pseudo-forces' representing speed regulation, pressure, pairwise attraction, and a 'non-local viscosity' term. These terms are discussed below.

The first term on the right-hand side of Eq. (2.1) acts as a speed-regulation term used commonly in the literature [10, 11, 26] and apparently first used by Rayleigh [34] as cited by [11]. This term either increases or reduces the magnitude of the velocity depending on how the velocity compares to v_0. If $v > v_0$, the acceleration is negative in the direction of $\mathbf{v}$, and thus $|\mathbf{v}| = v$ is reduced. If $v < v_0$, the acceleration is positive in the direction of $\mathbf{v}$, hence v is increased. Thus v_0 can be regarded as modeling the average preferred natural speed of an individual. The time scale for this velocity clamping is τ. Note that this speed-regulation term is frame dependent and applies when considering the frame in which the medium (e.g., air for birds, water for fish, or land for ungulates), through which the flock individuals move, is stationary.

In order to model the presumed tendency of nearby flock members to repel each other to avoid collision, some past models have introduced a pressure-like term, as in the second term on the right-hand side of Eq. (2.1). Examples can be found in [39]. In addition, another means to model repulsion is via a general repulsive potential; i.e., a pairwise non-local soft-core potential (see [29, 25, 9]). We model repulsion using a pressure term, $P(\rho)$. For future reference, we write the pressure as a Taylor series around a density ρ_0 as

$$P(\rho) = c_s^2 \delta\rho + \left.\frac{\partial^2 P}{\partial \rho^2}\right|_{\rho=\rho_0} \delta\rho^2 + \dots \tag{2.3}$$

where $c_s^2 = \left.\frac{\partial P}{\partial \rho}\right|_{\rho=\rho_0}$ and $\delta\rho = \rho - \rho_0$.

The third term on the right-hand side of Eq. (2.1) is a long-range attractive pseudo-force where long-range attraction is used to model the tendency for flocks

to form. This force is taken to be due to an attractive pseudo-potential, U, which is of the form

$$U(\mathbf{x}) = \int \hat{u}(\mathbf{x} - \mathbf{x}')\rho(\mathbf{x}')d\mathbf{x}'. \tag{2.4}$$

It proves convenient to choose the kernel $\hat{u}(\mathbf{x}-\mathbf{x}')$ to satisfy the modified Helmholtz equation,

$$\left(\nabla^2 - \kappa_\rho^2\right)\hat{u}(\mathbf{x} - \mathbf{x}') = u_0\delta\left(\mathbf{x} - \mathbf{x}'\right), \tag{2.5}$$

where $u_0 > 0$ is the strength of the potential. In three dimensions $u(\mathbf{x}-\mathbf{x}')$ has the form of an attractive exponentially-screened Coulomb potential,

$$\hat{u}(\mathbf{x} - \mathbf{x}') = -\frac{u_0}{4\pi}\frac{e^{-\kappa_\rho|\mathbf{x}-\mathbf{x}'|}}{|\mathbf{x} - \mathbf{x}'|}. \tag{2.6}$$

The quantity κ_ρ^{-1} provides a long-distance cutoff to the attractive pseudo-force. This type of attractive potential has been used in previous continuum flocking models [29, 25, 9].

Similar to the non-local attractive potential, we model the presumed tendency for nearby flock members to attempt to align their velocities by use of the term

$$\mathbf{W}(\mathbf{x}) = \int \hat{w}(\mathbf{x} - \mathbf{x}')[\mathbf{v}(\mathbf{x}') - \mathbf{v}(\mathbf{x})]d\mathbf{x}', \tag{2.7}$$

with the kernel $\hat{w}(\mathbf{x} - \mathbf{x}')$ satisfying an equation similar to that for the attractive kernel,

$$\left(\nabla^2 - \kappa_w^2\right)\hat{w}(\mathbf{x} - \mathbf{x}') = w_0\delta\left(\mathbf{x} - \mathbf{x}'\right), \tag{2.8}$$

with strength $w_0 > 0$ and screening length scale κ_w^{-1}. This term reorients the velocity vector, $\mathbf{v}(\mathbf{x})$, toward the average velocity of the other flock members, weighting velocities of flock members closer to $\mathbf{x}$ more strongly than those farther away. These

are our general equations that model flocking. Various dynamical behaviors and flocking equilibria can be explored using this framework. In the rest of the dissertation, this basic model gives us the means to attack the problems introduced in Chapter 1. To that end, in the rest of this chapter we consider perturbations around a specific equilibrium density defined below.

We consider the following simplified situation. A particular spatially- homogeneous steady-state solution to Eqs. (2.1) and (2.2) is

$$\rho(\mathbf{x}) = \rho_0 = \text{const.} \quad \text{and} \quad \mathbf{v}(\mathbf{x}) = \mathbf{v}_0 = \text{const.} \tag{2.9}$$

Alternatively, we may think of this equilibrium as a localized approximation of a more complicated solution where the density is not everywhere constant. For example, in the middle of a nonuniform flock, the density in equilibrium will be nearly constant (see [25]).

To the general equations Eqs. (2.1) and (2.2), we will add an additional, external, localized, repulsive potential that we view as modeling the effect of a stationary obstacle or a predator moving through the flock with velocity $\mathbf{v}_p$. In the next section, we treat this problem within the framework of linearized theory and consider how perturbations propagate through the flock.

2.3 Heuristic Discussion of Interaction with an Obstacle

2.3.1 Dispersion Relation and Plane Waves

By looking at the dispersion relation of linear waves in the full system, we may determine how such waves propagate within the flock. This will inform us as to the relationship between the frequency, wavelength, and propagation direction of the waves. In our case, we will find that this will predict a disturbance cone when an obstacle or predator is encountered by a flock. For convenience we make a transformation of independent variables such that $\mathbf{x}' = \mathbf{x} - \mathbf{v}_p t$ and $t' = t$ where $\mathbf{v}_p$ is the velocity of the obstacle or predator relative to the stationary frame in which the preferred flock speed is $\mathbf{v}_0$. This is similar to a Galilean frame transformation except that the velocity $\mathbf{v}$ remains the velocity in the stationary frame. After making this transformation we drop the primes on $\mathbf{x}'$ and t'. Writing Eqs. (2.1) and (2.2) in this new frame gives

$$\frac{\partial \mathbf{v}}{\partial t} - \mathbf{v}_p \cdot \nabla \mathbf{v} + \mathbf{v} \cdot \nabla \mathbf{v} = \frac{1}{\tau}\left(1 - \frac{v^2}{v_0^2}\right)\mathbf{v} - \frac{1}{\rho}\nabla P(\rho) - \nabla U - \mathbf{W} \tag{2.10}$$

$$\frac{\partial \rho}{\partial t} - \mathbf{v}_p \cdot \nabla \rho + \nabla \cdot (\rho \mathbf{v}) = 0. \tag{2.11}$$

Setting $\rho = \rho_0 + \delta\rho$ and $\mathbf{v} = \mathbf{v}_0 + \delta\mathbf{v}$, with $|\delta\rho| \ll \rho_0$ and $|\delta\mathbf{v}| \ll \mathbf{v}_0$, we substitute these into Eqs. (2.10) and (2.11) and only keep linear terms in $\delta\rho$ and $\delta\mathbf{v}$. Taking Fourier transforms in both space and time we obtain

$$-i\omega\delta\tilde{\mathbf{v}} + i\mathbf{k}\cdot\mathbf{v}_r\,\delta\tilde{\mathbf{v}} = -\frac{2}{\tau v_0^2}\left(\mathbf{v}_0 \cdot \delta\tilde{\mathbf{v}}\right)\mathbf{v}_0 - i\mathbf{k}\left(c_s^2\frac{\delta\tilde{\rho}}{\rho_0} + \tilde{u}\delta\tilde{\rho}\right) - \nu_w\delta\tilde{\mathbf{v}} \tag{2.12}$$

$$0 = -i\omega\delta\tilde{\rho} + i\mathbf{k}\cdot\mathbf{v}_r\,\delta\tilde{\rho} + \rho_0 i\mathbf{k}\cdot\delta\tilde{\mathbf{v}}, \tag{2.13}$$

where we define $\mathbf{v}_r = \mathbf{v}_0 - \mathbf{v}_p$, and $\tilde{f} = \tilde{f}(\mathbf{k}, \omega)$ denotes the Fourier transform of $f(\mathbf{x}, t)$ given by

$$\tilde{f} = \tilde{f}(\mathbf{k}, \omega) = \int f(\mathbf{x}, t) \exp(i\omega t - i\mathbf{k} \cdot \mathbf{x}) d\mathbf{x} dt. \tag{2.14}$$

Hence we have

$$\tilde{u}(k^2) = \frac{-u_0}{k^2 + \kappa_\rho^2}, \tag{2.15}$$

$$\tilde{w}(k^2) = \frac{-w_0}{k^2 + \kappa_w^2}, \tag{2.16}$$

$$\nu_w(k^2) = \tilde{w}(k^2) - \tilde{w}(0) = \left(\frac{w_0}{\kappa_w^2}\right) \frac{k^2}{k^2 + \kappa_w^2}, \tag{2.17}$$

$$c_s^2 = \left.\frac{\partial P}{\partial \rho}\right|_{\rho=\rho_0}. \tag{2.18}$$

Using Eq. (2.13) to eliminate $\delta\tilde{\rho}/\rho_0$ from Eq. (2.12), we arrive at

$$\left[(\omega - \mathbf{k} \cdot \mathbf{v}_r) + i\nu_w\right] \delta\tilde{\mathbf{v}} = -\frac{2i\mathbf{v}_0 \cdot \delta\tilde{\mathbf{v}}}{\tau v_0^2} \mathbf{v}_0 + \frac{(c_s^2 + \rho_0 \tilde{u})\mathbf{k} \cdot \delta\tilde{\mathbf{v}}}{\omega - \mathbf{k} \cdot \mathbf{v}_r} \mathbf{k}. \tag{2.19}$$

Restricting our attention to the case where $\tau \to 0$ and $\nu_w \to 0$ (the limit in which speed regulation occurs instantaneously and the non-local viscosity is absent), we obtain particularly simple results describing the propagation of waves within the flock. Note that to accommodate the $\tau \to 0$ limit in Eq. (2.19), we must have that $\mathbf{v}_0 \cdot \delta\tilde{\mathbf{v}} \to 0$. Without loss of generality, we choose $\mathbf{v}_0$ to be in the x direction, which means that $\delta\tilde{\mathbf{v}} = \delta\tilde{v}_y \, \hat{\mathbf{y}} + \delta\tilde{v}_z \, \hat{\mathbf{z}}$. If we now project Eq. (2.19) onto the y and z directions, we get two coupled equations for $\delta\tilde{v}_y$ and $\delta\tilde{v}_z$. These yield the dispersion relation,

$$(\omega - \mathbf{k} \cdot \mathbf{v}_r)^2 = k_\perp^2 c_s^2, \tag{2.20}$$

where we have taken $\nu_w \to 0$, and defined $\mathbf{k}_\perp = k_y \hat{\mathbf{y}} + k_z \hat{\mathbf{z}}$ giving the magnitude as $k_\perp^2 = k_y^2 + k_z^2$. Also, we have replaced $c_s^2 + \rho_0 \tilde{u} \to c_s^2$, which is true for large k. We

can write the final dispersion relation as

$$\omega = \mathbf{k} \cdot \mathbf{v}_r \pm k_\perp \, c_s. \tag{2.21}$$

Thus, the group velocity of waves, in the frame moving at a velocity $\mathbf{v}_p$, within the flock is given by

$$\mathbf{v}_g = \frac{\partial \omega}{\partial \mathbf{k}} = \mathbf{v}_r + \frac{\mathbf{k}_\perp}{k_\perp} c_s, \tag{2.22}$$

In the next section, we use this result to derive a disturbance cone that propagates through the flock when the flock encounters an obstacle or predator.

2.3.2 Mach Cones

Following Mach's well-known construction (see for example [13]) for the cone produced in supersonic velocities through a fluid, we may develop a prediction for the information cone that is propagating though the flock using the dispersion relation derived above. In the case of a *stationary* object (Fig. 2.1(a)), the only way that information can travel is perpendicular to the direction of motion with the propagation speed of c_s, in the frame of the obstacle, as can be seen in Eq. (2.22) with $\mathbf{v}_r = \mathbf{v}_0$ (or equivalently $\mathbf{v}_p = 0$). Accordingly, we get a right-circular cone in three dimensions (a wedge in two dimensions) of cone angle θ, measured from the direction of the flock, given by

$$\tan \theta = \frac{c_s}{v_0}, \tag{2.23}$$

where c_s is defined above (Eq. (2.18)). Notice that this is valid for all velocities, contrary to a usual acoustic Mach cone which only exists for velocities of the moving

object that are above the sound speed. Equation 2.23 limits to an angle of $\theta = \pi/2$ for small v_0, and $\theta \cong 0$ for large $v_0 \gg c_s$.

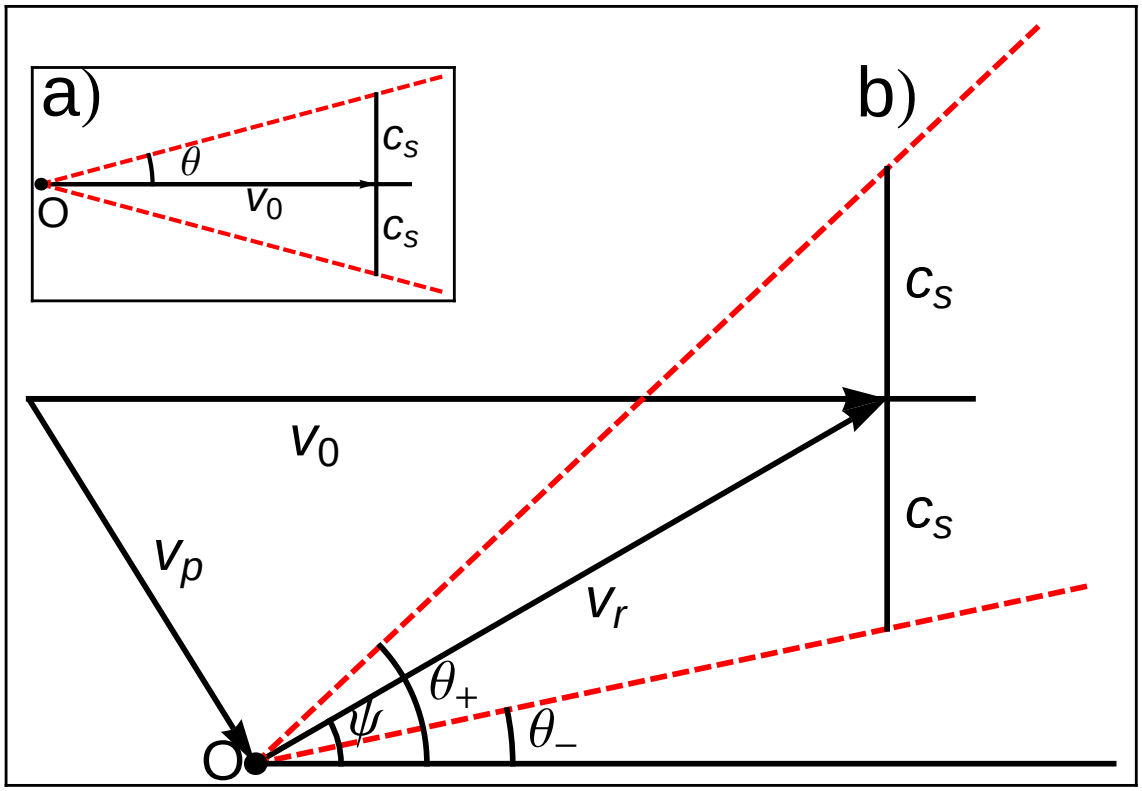

Figure 2.1: Diagram for a density disturbance caused by flock moving past an obstacle in steady state. a) Static obstacle: Obstacle is stationary (at point O), the dashed red lines indicate the intersection of a plane passing through the axis of the cone of disturbance and a large-density fluctuation wake that would exist downstream of the flock/obstacle interaction. The angle θ is referred to as the 'wedge' angle. b) Moving obstacle: In the frame of the obstacle at point O, the density disturbance is indicated by the dashed lines. $\mathbf{v}_0$ is the velocity of the flock and $\mathbf{v}_p$ is the velocity of the obstacle, both in the frame of the medium.

For the case of a moving obstacle or predator, Eq. (2.22) implies the construction shown in Fig. 2.1(b). From this construction, we obtain the wedge angles, $\theta_\pm$,

in a plane passing through the cone's axis (defined by $\mathbf{v}_0$ and $\mathbf{v}_p$), given by

$$\tan\theta_\pm = \pm\frac{1}{\cos(\psi)}\left(\frac{c_s}{v_r}\right) + \tan(\psi). \tag{2.24}$$

Cross sections for the wedge shapes of both the static and moving obstacle are shown in Fig. 2.1. In three dimensions, a moving obstacle produces an oblique circular cone as illustrated in Fig. 2.2. If $\mathbf{v}_0$ and $\mathbf{v}_p$ are co-linear, the the cone is a right-circular cone with $\theta_+ = \theta_-$, and $\psi = 0$.

2.4 Linearized Theory in a Two-Dimensional Flock

In order to assess the extent to which these predictions apply more generally, we consider a two-dimensional case for both the static and moving obstacle situations. We first solve a linearized version of Eqs. (2.10) and (2.11) for the density fluctuation $\delta\rho/\rho_0$ in terms of an integral. We then specialize to a static case to analyze $\delta\rho/\rho_0$ analytically. Following that, we numerically evaluate our integral-expression solution for both the static and moving cases and compare the results to our simple predictions above.

To specialize to two dimensions, we consider a flock equilibrium that is spatially uniform in the z direction. Suppose that an obstacle (call it a predator) is moving through the flock at constant velocity, $\mathbf{v}_p$, relative to the fixed frame of the medium (e.g. air or water) in which the flock moves. We assume that there is no motion in the z direction. We model the obstacle by a moving, localized, repulsive potential, $\eta(\mathbf{x}, t)$, and add the term $-\nabla\eta$ to the right-hand side of Eq. (2.10). We

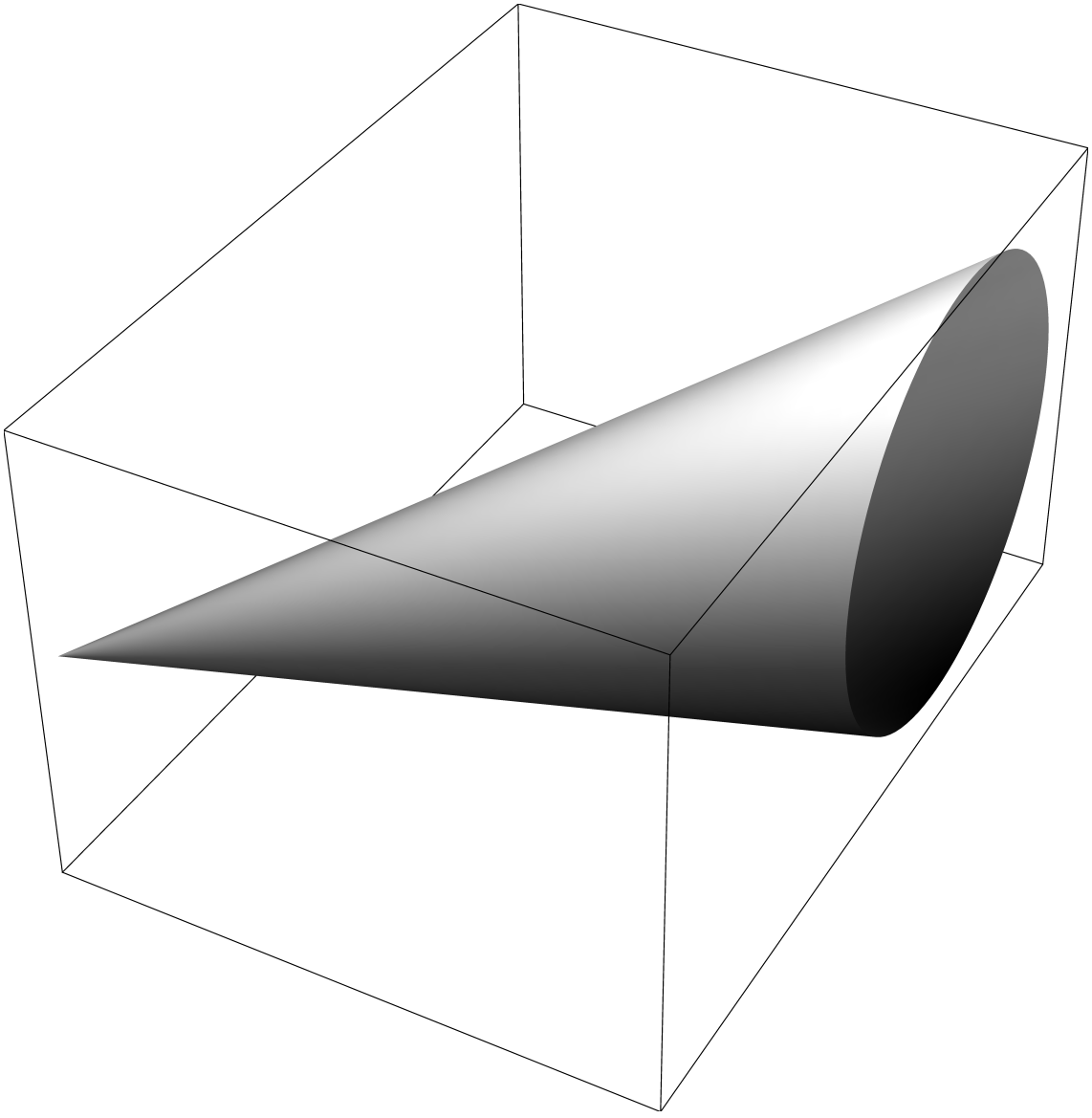

Figure 2.2: An oblique circular cone.

take η to be Gaussian in space and given by

$$\eta = \eta(\mathbf{x}, t) = \eta_0 \exp\left[-\frac{(x - v_{px}t)^2 + (y - v_{py}t)^2}{l^2}\right], \tag{2.25}$$

where η_0 is the strength of the obstacle, l is the length scale over which the obstacle acts, and v_{px} and v_{py} are the components of is the predator's velocity, $\mathbf{v}_p$, in the x-y plane. In two dimensions, this can roughly be thought of as a kind of moving flagpole around which the flock must navigate. Without loss of generality, we set $\mathbf{v}_0 = v_0\,\hat{\mathbf{x}}$. Given this situation we consider the steady-state flock response in the approximation of infinite flock size. The dynamics of a finite-size flock as it impinges on an obstacle hitting a flock has not been considered in the present work. For a simulation of such a situation, see [23].

We add the obstacle potential to Eq. (2.10) and, in the frame of the obstacle, linearize around the constant density, as we did in §2.3.1. Taking a spatial Fourier transform of Eqs. (2.10) and (2.11) (including the obstacle), we obtain the following steady-state (i.e., $\partial/\partial t = 0$) equations,

$$(-i\mathbf{k}\cdot\mathbf{v}_p + i\mathbf{k}\cdot\mathbf{v}_0)\,\delta\tilde{\mathbf{v}} = -\frac{2}{\tau v_0^2}\,(\mathbf{v}_0\cdot\delta\tilde{\mathbf{v}})\,\mathbf{v}_0 - i\mathbf{k}\left(c_s^2\frac{\delta\tilde{\rho}}{\rho_0} + \tilde{u}\delta\tilde{\rho} + \tilde{\eta}\right) - \nu_w\delta\tilde{\mathbf{v}} \tag{2.26}$$

$$-i\mathbf{k}\cdot\mathbf{v}_p\,\delta\tilde{\rho} + i\mathbf{k}\cdot\mathbf{v}_0\,\delta\tilde{\rho} + \rho_0 i\mathbf{k}\cdot\delta\tilde{\mathbf{v}} = 0, \tag{2.27}$$

with

$$\tilde{\eta}(k^2) = \eta_0 l^2 \pi e^{-\frac{1}{4}\left(k_x^2 + k_y^2\right)l^2}, \tag{2.28}$$

and the other quantities defined in Eqs. (2.15 - 2.18). Using Eq. (2.27) to eliminate $\delta\tilde{\rho}/\rho_0$ from Eq. (2.26), we arrive at

$$i\mathbf{k}\cdot\mathbf{v}_r\,\delta\tilde{\mathbf{v}} + \frac{2}{v_0^2\tau}\,(\mathbf{v}_0\cdot\delta\tilde{\mathbf{v}})\,\mathbf{v}_0 + \nu_w\,\delta\tilde{\mathbf{v}} - i\mathbf{k}\left(c_s^2 + \rho\tilde{u}\right)\frac{\mathbf{k}\cdot\delta\mathbf{v}}{\mathbf{k}\cdot\mathbf{v}_r} = -i\mathbf{k}\tilde{\eta}. \tag{2.29}$$

where, again, $\mathbf{v}_r = \mathbf{v}_0 - \mathbf{v}_p$. Since there is no disturbance along the z-direction, we set $\mathbf{k} = k_x\hat{\mathbf{x}} + k_y\hat{\mathbf{y}}$. Introducing an orthonormal basis $\{\hat{\mathbf{a}}_1, \hat{\mathbf{a}}_2, \hat{\mathbf{a}}_3\}$ such that

$$\hat{\mathbf{a}}_1 = \hat{\mathbf{k}} = \frac{\mathbf{k}}{k}, \quad \hat{\mathbf{a}}_2 \cdot \hat{\mathbf{z}} = 0, \quad \hat{\mathbf{a}}_3 = \hat{\mathbf{z}}, \tag{2.30}$$

we project Eq. (2.29) onto these three directions. Defining

$$\delta\tilde{\mathbf{v}} = \delta\tilde{v}_1\,\hat{\mathbf{a}}_1 + \delta\tilde{v}_2\,\hat{\mathbf{a}}_2 + \delta\tilde{v}_3\,\hat{\mathbf{a}}_3, \tag{2.31}$$

Eq. (2.29) yields

$$ikv_r\cos(\psi-\phi)\delta\tilde{v}_1 + \frac{2}{\tau v_0^2}v_0\cos(\phi)\left(v_0\cos(\phi)\delta\tilde{v}_1 - v_0\sin(\phi)\delta\tilde{v}_2\right) + \nu_w\delta\tilde{v}_1 - ik(c_s^2+\rho_0\tilde{u})\frac{\delta\tilde{v}_1}{v_r\cos(\psi-\phi)} = -ik\tilde{\eta} \tag{2.32}$$

$$ikv_r\cos(\psi-\phi)\delta\tilde{v}_2 - \frac{2}{\tau v_0^2}v_0\sin(\phi)\left(v_0\cos(\phi)\delta\tilde{v}_1 - v_0\sin(\phi)\delta\tilde{v}_2\right) + \nu_w\delta\tilde{v}_2 = 0 \tag{2.33}$$

and $\delta\tilde{v}_3 = 0$, where we have changed coordinates from (k_x, k_y) to (k, ϕ). Here ϕ is the angular orientation of $\mathbf{k}$, measured from the x axis, and ψ is the angle between $\mathbf{v}_r$ and the x axis. We can obtain general results for $\delta\mathbf{v}(x,y)$ and $\delta\rho(x,y)$ by solving Eqs. (2.32), (2.33), and (2.27) for $\delta\tilde{v}_1$, $\delta\tilde{v}_2$, and $\delta\tilde{\rho}$ and then inverse Fourier transforming the result. However, for simplicity in what follows, we again take $\tau \to 0$, clamping all of the flocking individuals to the same speed. Equations (2.32), (2.33), and (2.27) then yield

$$\frac{\delta\tilde{\rho}(k,\phi)}{\rho_0} = \frac{k^2\tilde{\eta}\sin^2(\phi)}{k^2v_r^2\cos^2(\psi-\phi) - k^2\bar{c}^2\sin^2(\phi) - ik\nu_w v_r\cos(\psi-\phi)}, \tag{2.34}$$

with

$$\bar{c}^2(k) = c_s^2 + \rho_0\tilde{u}(k) = c_s^2 + \frac{\rho_0 u_0}{k^2+\kappa_\rho^2}. \tag{2.35}$$

By inverse Fourier transforming, we obtain the density perturbation at any point (r, θ) in the flock,

$$\frac{\delta\rho(r,\theta)}{\rho_0} = \frac{1}{(2\pi)^2}\int_0^\infty\int_0^{2\pi} \frac{\delta\tilde{\rho}(k,\phi)}{\rho_0}\, e^{ikr\cos(\phi-\theta)} k d\phi dk, \tag{2.36}$$

where $\delta\tilde{\rho}(k,\phi)/\rho_0$ is defined in Eq. (2.34). In the next section, we explore Eq. (2.36) analytically in the case of a static obstacle. After that, we evaluate Eq. (2.36) numerically for both a static and a moving obstacle/predator.

2.5 Analytical Results for a Static Obstacle

To evaluate the integral, we consider the following illustrative case. We take $\mathbf{v}_r = \mathbf{v}_0$, which corresponds to a stationary obstacle or predator. This implies that $\psi = 0$. Also, assume that the parameters are such that for most values of k, the quantities $\bar{c}$ and ν_w can be approximated by their large k limits. We have

$$\bar{c} \approx \lim_{k\to\infty} \bar{c}(k) = c_s, \tag{2.37}$$

$$\nu_w \approx \lim_{k\to\infty} \nu_w(k) = \frac{w_0}{\kappa_w^2}. \tag{2.38}$$

The range over which this approximation is good will be investigated in §2.6. With these approximations we can integrate (2.36) to obtain the density perturbation $\delta\rho/\rho_0$. The full analysis is done in Appendix A. Fig. 2.3 displays the density perturbation for a particular choice of the parameters. Note that the main feature is a wedge formed from the information of the obstacle propagating through the flock. We find, in Appendix A, that density will be large when y is near $\pm y_0$, where

$$y_0(x) = \frac{1}{\gamma}\left(x - \frac{l^2}{2\gamma}\epsilon\right). \tag{2.39}$$

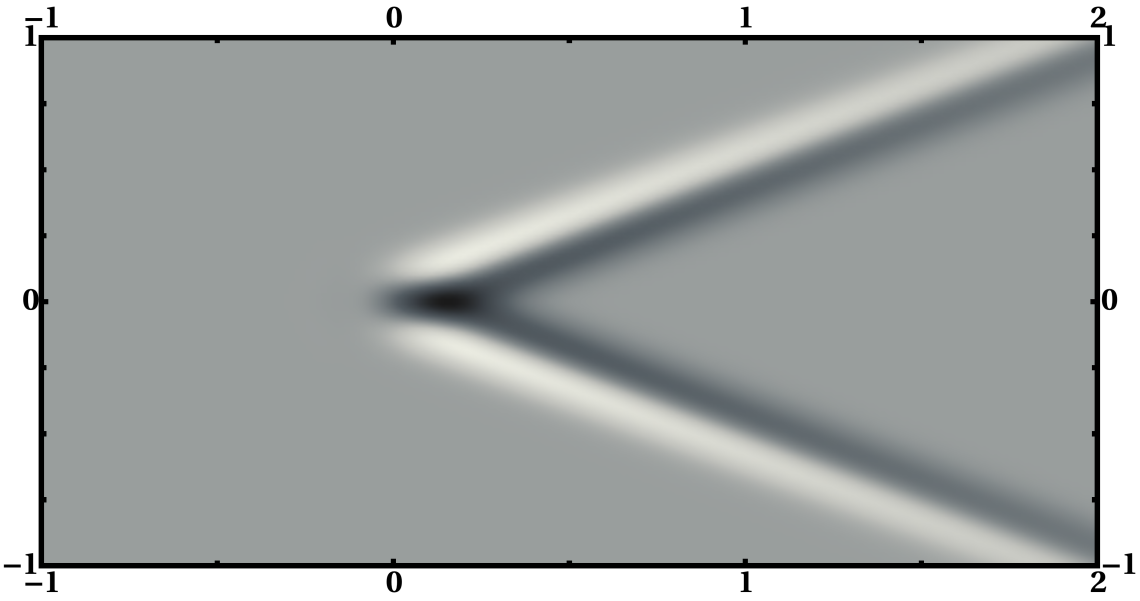

Figure 2.3: Plot of the density fluctuations. Parameters used for the figure are: $c_s = 15$, $\eta_0 = 1$, $\epsilon = 0.838$, $\gamma = 2$, and $l = 0.1$. The x axis is horizontal, the y axis is vertical.

where we have introduced the quantities $\epsilon = \nu_w/2\bar{c}$ and $\gamma = v_0/\bar{c}$. The first term in Eq. (2.39), x/γ, corresponds to the wedge condition, Eq. (2.23).

Figure 2.4 shows $\delta\rho(x, y)/\rho_0$ versus y for several fixed values of x. Numerical data (computed in §2.6) are plotted as open circles, and the theory obtained in Appendix A is plotted as a solid curve. They agree well. Further approximations (see Appendix A) result in analytic expressions for the height, $\mathcal{H}$, and width, $\mathcal{W}$, of these profiles (illustrated in Fig. 2.4(a)). The height, $\mathcal{H}$ ($\delta\rho/\rho_0$ at maximum), and width, $\mathcal{W}$ (distance between maximum and minimum), are

$$\mathcal{H}(x) = \frac{\eta_0\gamma}{\bar{c}^2(1+\gamma^2)}\sqrt{\frac{\pi}{2}}\exp\left[-\frac{1}{2} + \frac{\epsilon^2 l^2 - 4x\gamma\epsilon}{4\gamma^2}\right] \tag{2.40}$$

$$\mathcal{W} = \frac{2}{\sqrt{2}}\frac{\sqrt{1+\gamma^2}}{\gamma}l. \tag{2.41}$$

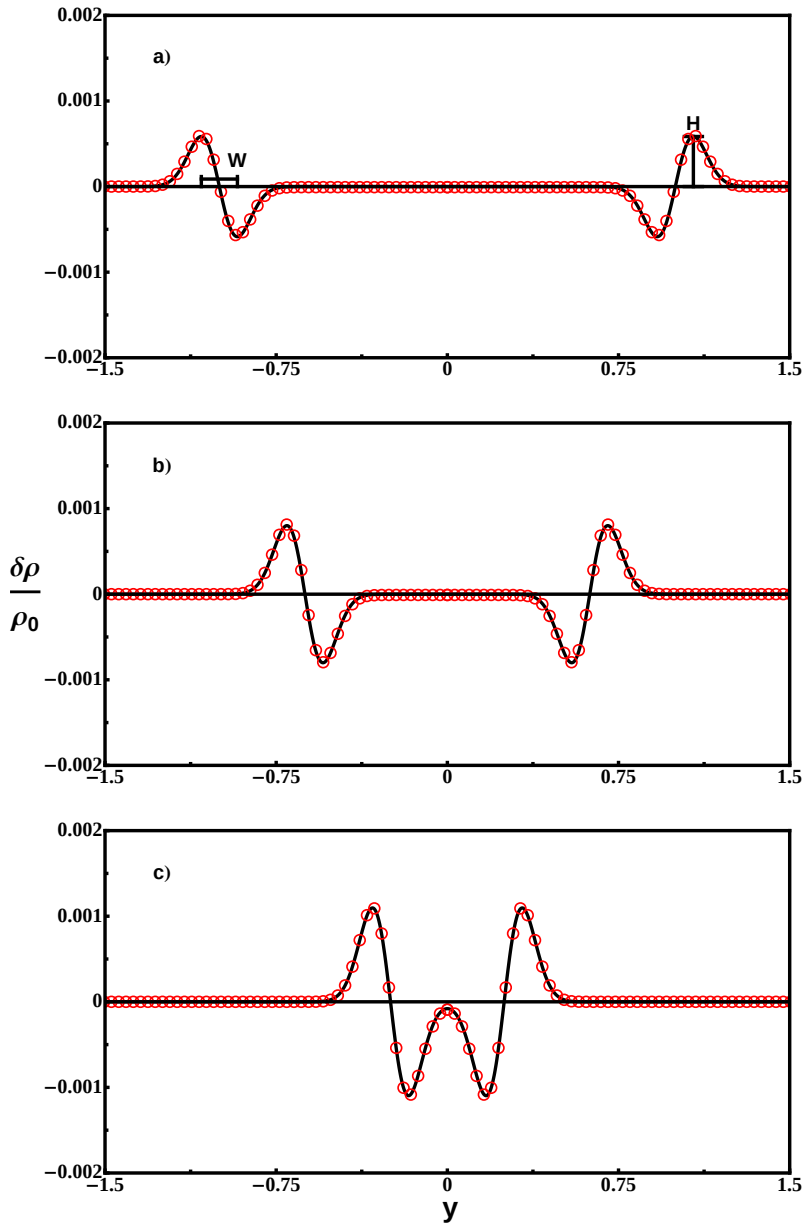

Figure 2.4: Plot of the density fluctuation for constant values of x for the same parameters in Fig. 2.3. The red circles are numerical values (computed via §2.6 methods) and the solid curve is the theory. a) $x = 2$. The definitions for height and width are displayed on the plot. b) shows $x = 1.25$, and c) $x = 0.5$.

From these expressions we see that the width is predicted to be insensitive to many of the parameters of our problem except l and γ. For example, the width does not increase far from the source of the disturbance (i.e., W in Eq. (2.41) does not depend on x). A main feature of Eq. (2.40) is its prediction of the exponential decay of the height of the disturbance with increasing x. In the next section, we compare numerical simulations with these predictions.

2.6 Numerical Results

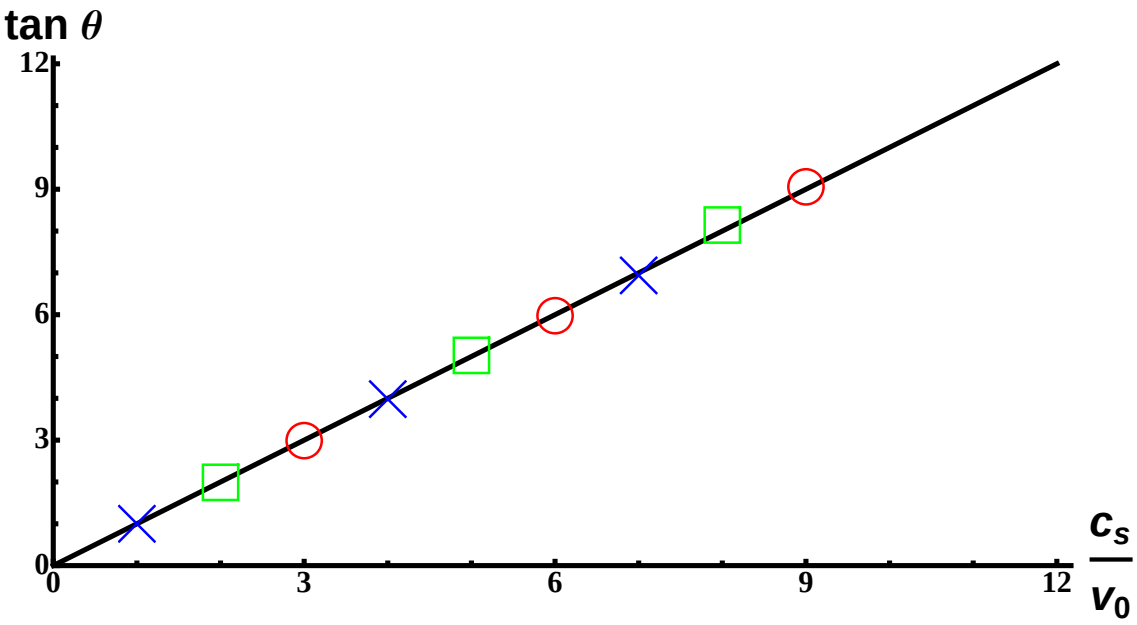

Figure 2.5: Plot showing the wedge angle θ vs. the quantity $\frac{c_s}{v_0}$, for $c_s = 15$. This shows the agreement of the numerical data for $w_0/4\pi = 0.001$ (red circles), $w_0/4\pi = 0.01$ (green boxes), and $w_0/4\pi = 0.1$ (blue crosses). The solid line is the theoretical prediction for the wedge angle from Eq. (2.24). The other parameters for the plot are $u_0/4\pi = 0.1$, $\kappa_\rho = 0.1$, and $\kappa_w = 0.5$, $l = 0.1$, $\eta_0 = 1$, and $\rho_0 = 0.8$.

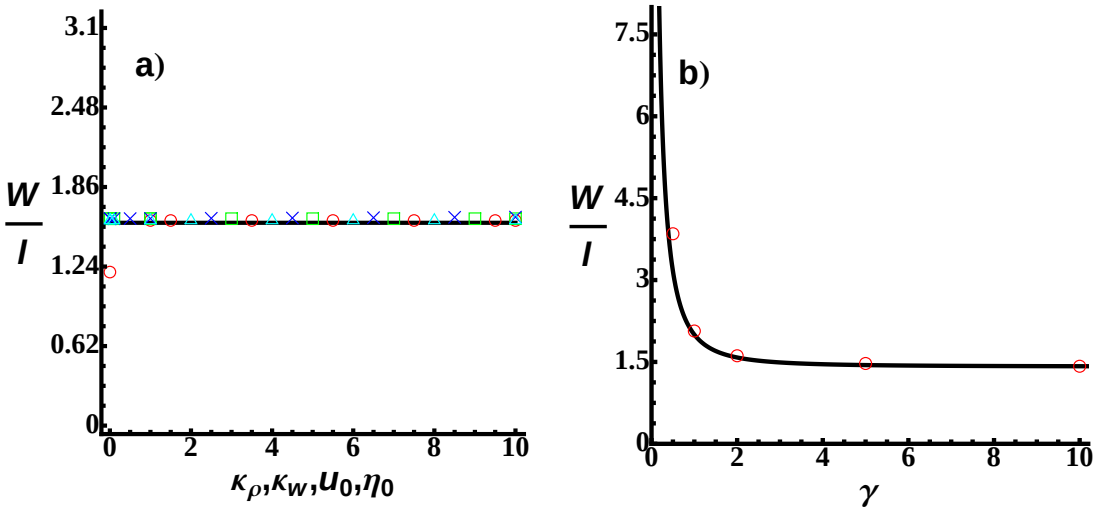

Figure 2.6: Graphs showing the dependence of the width on various parameters of the model. The solid curves is the expression in Eq. (2.41). The colored markers are numerical values obtained using the processes described in §2.6. a) $\mathcal{W}/l$ vs. κ_ρ (squares), κ_w (circles), u_0 (crosses), and η_0 (triangles). b) $\mathcal{W}/l$ vs. γ. If a parameter is not varied then it has the value: $\rho_0 = 0.8$, $c_s = 15$, $\gamma = 2$, $\eta_0 = 1$, $u_0/4\pi = 0.001$, $w_0/4\pi = 0.5$, $\kappa_w = 0.5$, $\kappa_\rho = 0.1$, $l = 0.1$, and $x = 2$.

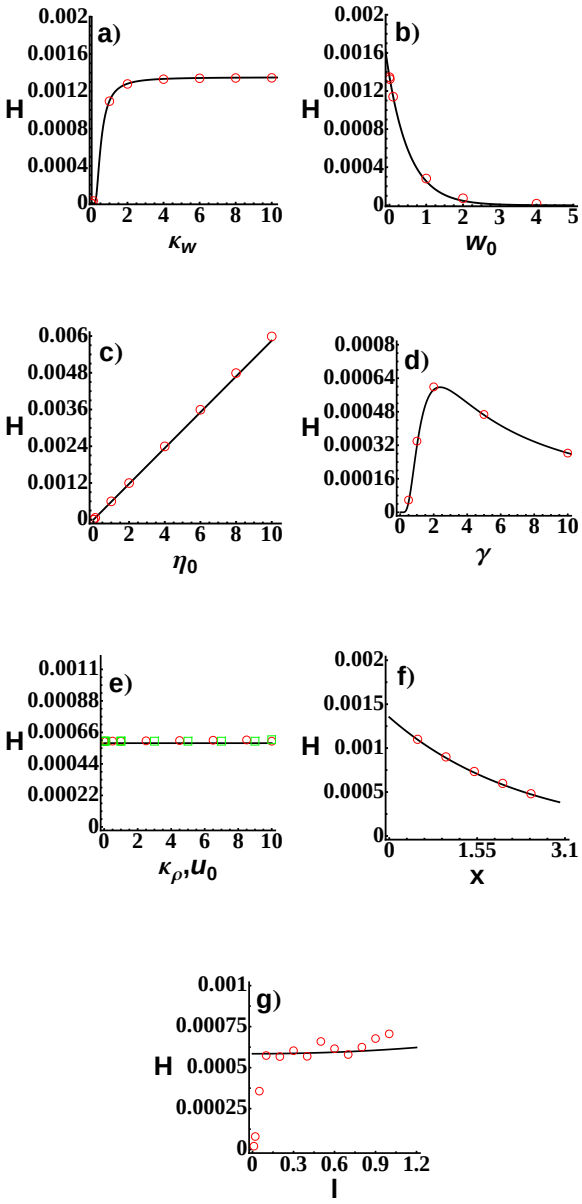

Figure 2.7: Various graphs showing the dependence of the height of the wedge on various parameters of the model. The solid curves is the expressions in Eq. (2.40). The colored markers are numerical values obtained using the processes in §2.6. a) $\mathcal{H}$ vs. κ_w. b) $\mathcal{H}$ vs. w_0. c) $\mathcal{H}$ vs. η_0. d) $\mathcal{H}$ vs. γ. e) $\mathcal{H}$ vs. κ_ρ (boxes), and u_0 (circles). f) $\mathcal{H}$ vs. x. g) $\mathcal{H}$ vs. l. If a parameter is not varied then it has the value: $\rho_0 = 0.8$, $c_s = 15$, $\gamma = 2$, $\eta_0 = 1$, $u_0/4\pi = 0.001$, $w_0/4\pi = 0.5$, $\kappa_w = 0.5$, $\kappa_\rho = 0.1$, $l = 0.5$, and $x = 2$.

2.6.1 The Static Obstacle

In order to evaluate the integral in Eq. (2.36) numerically, we need to do a two-dimensional infinite integral at each point in physical space. To do this, we express the kernel of the inverse Fourier transform as a sum of Bessel functions using the Jacobi-Anger expansion (see, for example, [1]). This allows us to do one of the iterated integrals via contour integration. We then obtain an infinite sum of single integrals at each real space point that we evaluate numerically. An example of the density fluctuation evaluated using these methods looks very similar to Fig. 2.3. Similar to the analytic result in Appendix A, the numerical density fluctuation shows a prominent wedge emanating from near the origin. The correspondence to the analytic work is excellent and can be seen in Fig. 2.4. We now compare the numerical results to theoretical predictions for $\theta_{\pm}$, $\mathcal{H}$, and $\mathcal{W}$.

Using the relation in Eq. (2.23), we can test the above results to determine the accuracy of the numerical fit to the wedge angle predicted earlier. Visually determining the angle from the numerical output gives a well defined wedge angle to about 0.5° accuracy. The tangent of this angle, Eq. (2.23), can then be compared with the quantity c_s/v_0. Figure 2.5 shows that this comparison yields very good agreement for the static case. The parameters used in Fig. 2.5 are $w_0/4\pi = 0.1$ (blue crosses), $w_0/4\pi = 0.01$ (green boxes), and $w_0/4\pi = 0.001$ (red circles). It is seen that changing w_0 leaves the wedge angle essentially unchanged.

Figure 2.6 shows comparisons between results for $\mathcal{W}$ from the numerical simulations (colored markers) with the predictions given in Eq. (2.41) (solid curves).

Figure 2.6(a) and shows that, as predicted by the theory, $\mathcal{W}/l$ is insensitive to the values of κ_ρ, κ_w, u_0, and η_0. The only important dependence of the width was on the parameter γ as seen in Fig. 2.6(b). Here we see that the wedge width approaches a constant value for large γ. Figure 2.7(a-d) show the dependence of the height, $\mathcal{H}$, on κ_w, w_0, η_0, and γ, respectively. In these figures, as well as in Fig. 2.6, if a parameter is not varied, then it has the value: $\rho_0 = 0.8$, $c_s = 15$, $\gamma = 2$, $\eta_0 = 1$, $u_0/4\pi = 0.001$, $w_0/4\pi = 0.5$, $\kappa_w = 0.5$, $\kappa_\rho = 0.1$, $l = 0.1$, and $x = 2$. As predicted by Eq. (2.40), $\mathcal{H}$ is linear in η_0. Figure 2.7(e) shows that the height is insensitive to both κ_ρ and u_0. The theoretical prediction for the dependence of the height on position, x, is verified in Fig. 2.7(f). Figure 2.7(g) shows that there is agreement with Eq. (2.40) for $l \gtrsim 0.15$, but breaks down at small l since the width is predicted to go to zero in that case. Additionally, the expansion in Appendix A used to obtain Eq. (A.9) implies that our approximations are expected to become invalid at large $\epsilon/\gamma = w_0/2\kappa_w^2 v_0$. For example, at very low κ_w, the width starts deviating from the prediction (Fig. 2.6(a), circles).

2.6.2 The Moving Obstacle

We numerically evaluated Eq. (2.36) using the same method as §2.6.1, but with non-zero predator angle, ψ. The results of the comparison between the theoretical prediction of the wedge angles and the numerics can be seen in Fig. 2.8. The theory, Eq. (2.24), predicts the wedge angles as a function of predator angle, ψ. The figure shows the correspondence to the numerical data for two angles, $\psi = \pi/3$ and

$\psi = \pi/6$, versus various values of c_s/v_0. The agreement is excellent, and, similar to the static case, the wedge angles are insensitive to parameters such as the nonlinear viscosity parameters, w_0 and κ_w.

2.7 Conclusions

In this chapter we have explored the response of a flock to static and moving obstacles. The obstacle is introduced into a flock and the fluctuations about an equilibrium are analyzed. We find that with both the static and the moving obstacles, the flock produces a prominent wedge where the information is propagating away from the disturbance, as shown by Fig. 2.3. The wedge angles can be predicted using a simple geometric construction. The information/disturbance propagates asymmetrically (unless $\psi = 0$), with two angles, θ_+ and θ_-, given by Eq. (2.24). We tested this analytically as well as numerically, and the result is found to agree well with the theoretical prediction. The wedge angles are insensitive to most physical parameters, most notably the velocity viscosity term, $\mathbf{W}$, and, unlike the well-known Mach cone in acoustics, there is no threshold speed for existence. Specifically, the angles only depend on the speed of sound in the flock, c_s, the speed of the flock, v_0, the relative speed of the obstacle to the flock, v_r, and the angle between them ψ. Heights and widths of the Mach cones for $\psi = 0$ are given by the analytic expression in Eq. (2.40) and Eq. (2.41). Numerical results are in good agreement with these expressions. It is also noteworthy that the wedge width, defined in Fig. 2.4(a), is insensitive to many parameters in the model as can be seen in Fig. 2.6(a).

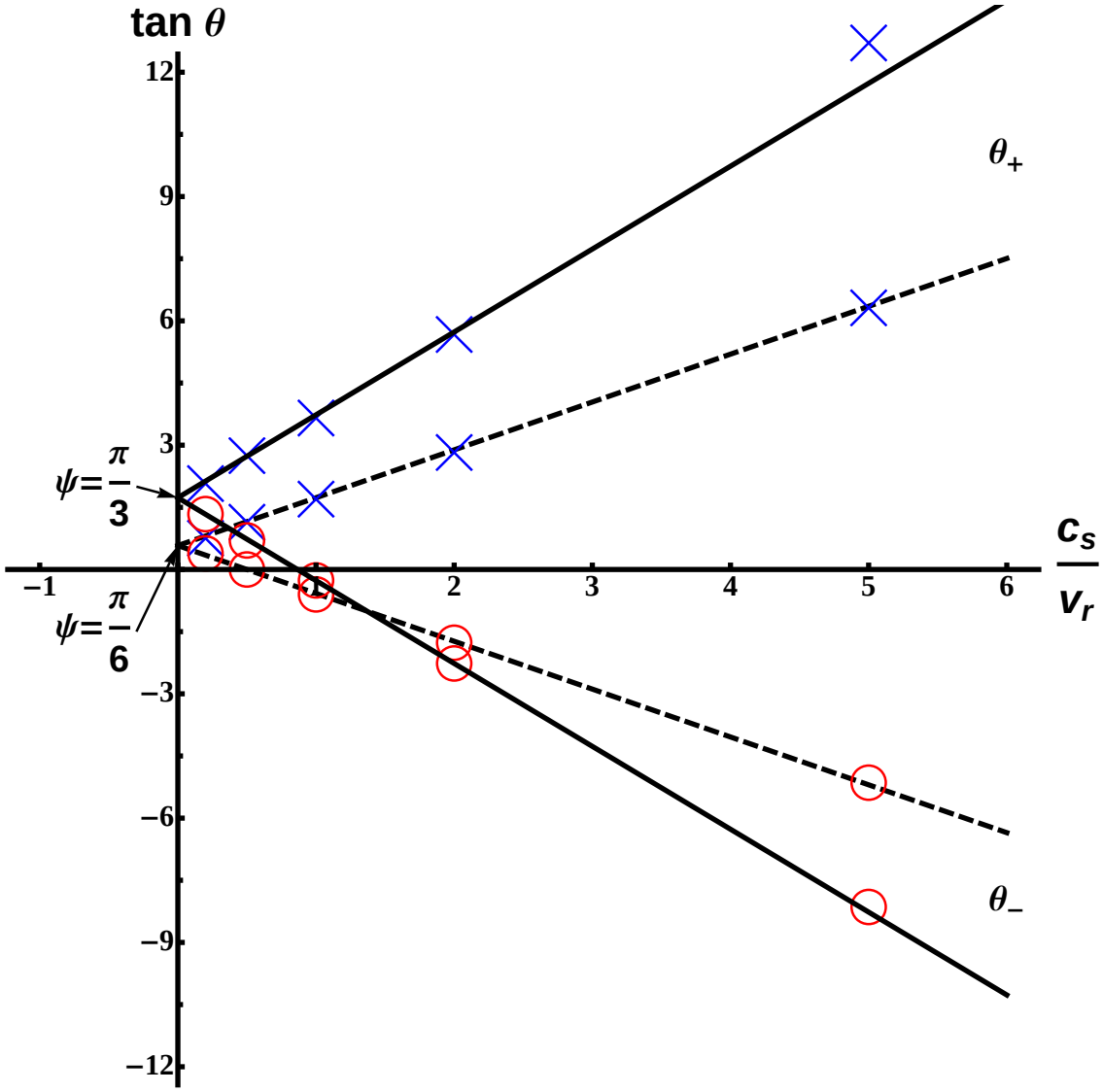

Figure 2.8: Plot showing the wedge angles $\theta_\pm$ vs the quantity $\frac{c_s}{v_r}$. This shows the agreement of the numerical data for two choices of predator angle ψ. The solid lines are the prediction of Eq. (2.24) for $\psi = \pi/3$, whereas the dashed lines are for $\psi = \pi/6$. The lines with the positive slope correspond to θ_+ (blue crosses), and the lines with the negative slope correspond to θ_- (red circles). The lines are the theoretical prediction for the wedge angles. The other parameters for these plots were $w_0/4\pi = 0.001$, $u_0/4\pi = 0.1$, $\kappa_\rho = 0.1$, and $\kappa_w = 0.1$.

Future work should include the dynamics of an obstacle hitting a flock, extension to $\tau \neq 0$, and a physical explanation of the wedge shape and offset from the origin. Finally, the extension to a fully nonlinear treatment of the obstacle is of interest.

Chapter 3

Temperature Effects in a Continuum Model for Flock Equilibria

3.1 Introduction

In this chapter and in the following chapter we will study one-dimensional flock equilibria. That is, in a frame moving with the flock, we will look for one-dimensional steady-state solutions of model equations for flocking. Although unrealistic, one-dimensional equilibria may provide useful insights into the more realistic, but analytically and numerically less accessible, three-dimensional equilibria. In particular, in this chapter, motivated somewhat by previous works of others [25, 7, 41, 6, 21, 33, 37], we consider a simple generalization of our model in Chapter 2, whereby we replace U by the sum of two potentials, $U = U_a + U_r$, where U_a is attractive and U_r is repulsive, and each is linearly related to ρ by an equation of the form of Eq. (2.4) (although the equation for U_r has a minus sign on the right-hand side of Eq. (2.4)). If one regards the attractive potential as spatially longer-range than the repulsive potential, then this corresponds to the idea of Reynolds [36] that flocking individuals experience nearby repulsion to avoid collisions and long-range attraction to preserve cohesion of the flock. Our work in Chapter 2 corresponds to setting $U_r = 0$. To some extent, the pressure term in Chapter 2 acts similarly to U_r in that it creates a repulsive force countering any tendency for high densities to form. For the linearized treatment employed in Chapter 2, any specific nonlin-

ear pressure can be shown to yield the same effect as a very short-range repulsive potential. This will be explicitly demonstrated in Chapter 4. However, when considering the nonlinear problems of obtaining equilibria, as we shall see, there is an important qualitative difference between the effects of U_r and a pressure term. The first part of this chapter (§3.1 – §3.2) studies the limit of zero pressure, $P(\rho) \equiv 0$, with one-dimensional variations in the spatial coordinate, x. This case turns out to be equivalent to previous work in [25] where they solved the problem numerically. We, on the other hand, will show that the problem can be solved analytically. Our solution will yield flock density profiles that go to zero density with a discontinuity at the flock boundary. In the second part of this chapter, §3.3, we introduce a pressure linearly related to the density, $P = T\rho$, with $T > 0$ (which might be regarded macroscopically as modeling random motions of the flocking individuals). We find that the introduction of positive T regularized the $T = 0$ solution, i.e., $\rho(x)$ now becomes everywhere smooth. However, with $T > 0$, we will also find that $\rho(x)$ does not decay to zero far from the flock, but instead approaches a (possibly small) constant value, $\rho(\pm\infty) = \rho_\infty > 0$. Furthermore, it can be argued (§3.4) that this result is not an artifact of the one-dimensional setting employed, and can be expected to persist for 2D and 3D flock equilibria solutions of our basic flocking model with $T > 0$. The situations for $T = 0$ and $T > 0$ are shown schematically in Fig. 3.1(a) and (b), respectively, and the result for $T > 0$ approaches the $T = 0$ result as $T \to 0^+$. The result that $\rho(\pm\infty) > 0$ for $T > 0$ is, perhaps, undesirable in that flocks are commonly believed to be of finite extent. However, if ρ becomes sufficiently small, the continuum approach we employ may be expected to break

down, and it can be argued that our results should only be taken seriously when ρ is not too small.

3.1.1 Continuum Equations of Motion

Following the spirit of Eq. (2.4) in one dimension, our attractive and repulsive potentials are

$$U_{a,r}(x) = \int \hat{u}_{a,r}(x - x')\rho(x')dx', \tag{3.1}$$

where the subscripts a and r denote attractive and repulsive, respectively. As in [25, 9] we take

$$\hat{u}_{a,r}(x) = \mp \frac{u_{a,r}}{2\kappa_{a,r}} \exp(-\kappa_{a,r}|x|), \tag{3.2}$$

where κ_a^{-1} (κ_r^{-1}) is the spatial range of attraction (repulsion) and u_a (u_r) characterizes the strength of the attraction (repulsion). Inserting Eq. (3.2) into Eq. (3.1) and differentiating the result twice with respect to x, we find that U_a and U_r satisfy the differential equations,

$$\frac{d^2}{dx^2}U_a - \kappa_a^2 U_a = u_a \rho, \tag{3.3}$$

$$\frac{d^2}{dx^2}U_r - \kappa_r^2 U_r = -u_r \rho. \tag{3.4}$$

Additionally, we restrict our attention to a linear pressure, $P(\rho) = T\rho$, and $\mathbf{v}$ in the direction, x, of the flock's spatial dependence, $\mathbf{v} = v\hat{\mathbf{x}}$. Thus, similar to Eqns. (2.1) and (2.2), we have

$$\frac{\partial \rho}{\partial t} = -\frac{\partial}{\partial x}(\rho\, v) \tag{3.5}$$

$$\frac{\partial v}{\partial t} + v\frac{\partial v}{\partial x} = -\frac{T}{\rho}\frac{\partial \rho}{\partial x} - \frac{\partial}{\partial x}(U_a + U_r) + \frac{1}{\tau}(1 - \frac{v^2}{v_0^2})v, \tag{3.6}$$

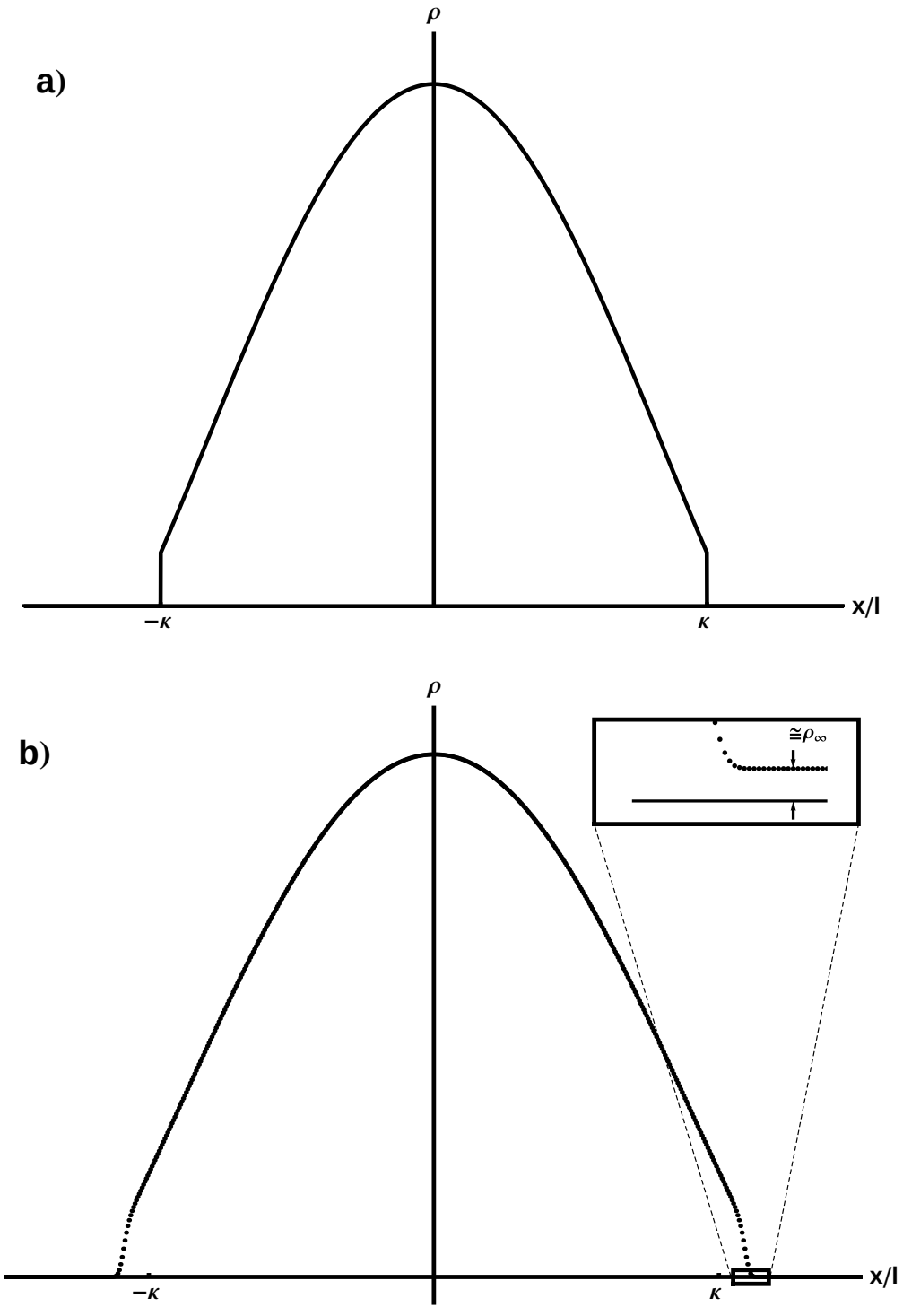

Figure 3.1: Illustration of a density profile for a) $T = 0$ and b) $T > 0$. In (b), $\rho_\infty = \rho(\pm\infty)$.

where we have omitted the term $\mathbf{W}(\mathbf{v})$ which will be zero for the equilibria we will investigate.

Various types of flock equilibria have been noted in [7, 41, 6, 21, 33, 37]. This chapter will study the simplest type of equilibrium; a constant-velocity flock. Taking v as constant and equal to v_0, and changing to a frame moving with velocity v_0, Eqns. (3.5) and (3.6) are satisfied for $\partial\rho/\partial t = 0$. Thus Eq. (3.6) yields a balance equation between the pressure $P(\rho)$ and the total potential $U_a + U_r$,

$$T\frac{d\rho}{dx} + \rho\frac{d}{dx}\left(U_a + U_r\right) = 0. \tag{3.7}$$

Our flock equilibria model thus consists of the three equations, (3.3), (3.4) and (3.7), for the three functions $U_a(x)$, $U_r(x)$, and $\rho(x)$.

3.2 Cold Equilibrium Solution

For $T = 0$, Eq. (3.7) yields the result that the total potential is constant,

$$U_a(x) + U_r(x) = U_0, \tag{3.8}$$

inside the flock ($\rho > 0$). Reference [25] considered the same pressure-less case that we consider here. Their approach was to use Eq. (3.8) and the integral equations

$$U_{a,r}(x) = \mp\frac{u_{a,r}}{2\kappa_{a,r}}\int \exp(-\kappa_{a,r}|x - x'|)\rho(x')dx', \tag{3.9}$$

(see Eq. (3.1)). They then solved these numerically, obtaining solutions like that shown in Fig. 3.1(a) with zero density outside the flock. Apparently, the authors of Ref. [25] did not notice that Eq. (3.9) implies that $U_a(x)$ and $U_r(x)$ satisfy Eqns.

(3.3) and (3.4), and this may be the reason that they did not realize that their problem could be solved analytically.

We seek equilibria that are even about $x = 0$ and are such that the flock has boundaries at $x = \pm l$, outside of which the density, ρ, is zero. Outside the flock (i.e., for $|x| > l$), the potentials satisfy Eqns. (3.3) and (3.4) with $\rho = 0$, but the force-balance constraint, Eq. (3.8), is absent, since, with $\rho = 0$, Eq. (3.7) is trivially satisfied. Thus $U_a + U_r$ is not constrained by Eq. (3.7) to be constant outside the flock ($|x| > l$). We also note that Eq. (3.9) implies that if $\rho(x) = 0$ for $|x| > l$, then $U_{a,r}(x)$ decay with increasing $|x|$ as $\exp(-\kappa_{a,r}|x|)$ for $|x| > l$. Hence, the total potential, $U_a + U_r$, should form a potential well with a flat region in $|x| < l$. We thus require a negative total potential at $x = l$ that, outside the flock boundaries, smoothly increases to zero with increasing $|x|$. Hence, U_0 is a negative constant. The situation is illustrated in Fig. 3.2.

Dividing Eq. (3.3) by u_a, and Eq. (3.4) by u_r and adding the two equations, we obtain

$$\frac{d^2}{dx^2}\left(\frac{U_a(x)}{u_a} + \frac{U_r(x)}{u_r}\right) - \left(\kappa_a^2 \frac{U_a(x)}{u_a} + \kappa_r^2 \frac{U_r(x)}{u_r}\right) = 0. \tag{3.10}$$

Using Eq. (3.8) to eliminate $U_r(x)$ or $U_a(x)$ from Eq. (3.10), we get

$$\frac{d^2 U_{a,r}(x)}{dx^2} + \kappa^2 U_{a,r}(x) = \mp \frac{u_{a,r}\kappa_{r,a}^2}{u_a - u_r} U_0, \tag{3.11}$$

where

$$\kappa^2 = \frac{\kappa_a^2 u_r - \kappa_r^2 u_a}{u_a - u_r}. \tag{3.12}$$

Thus the even solution of Eq. (3.11) for $U_{a,r}$ has the form $U_{a,r} = (\text{constant})\cos(\kappa x) + (\text{constant})$ if $\kappa^2 > 0$ and $U_{a,r} = (\text{constant})\cosh(\kappa' x) + (\text{constant})$ if $0 > \kappa^2 = -\kappa'^2$.

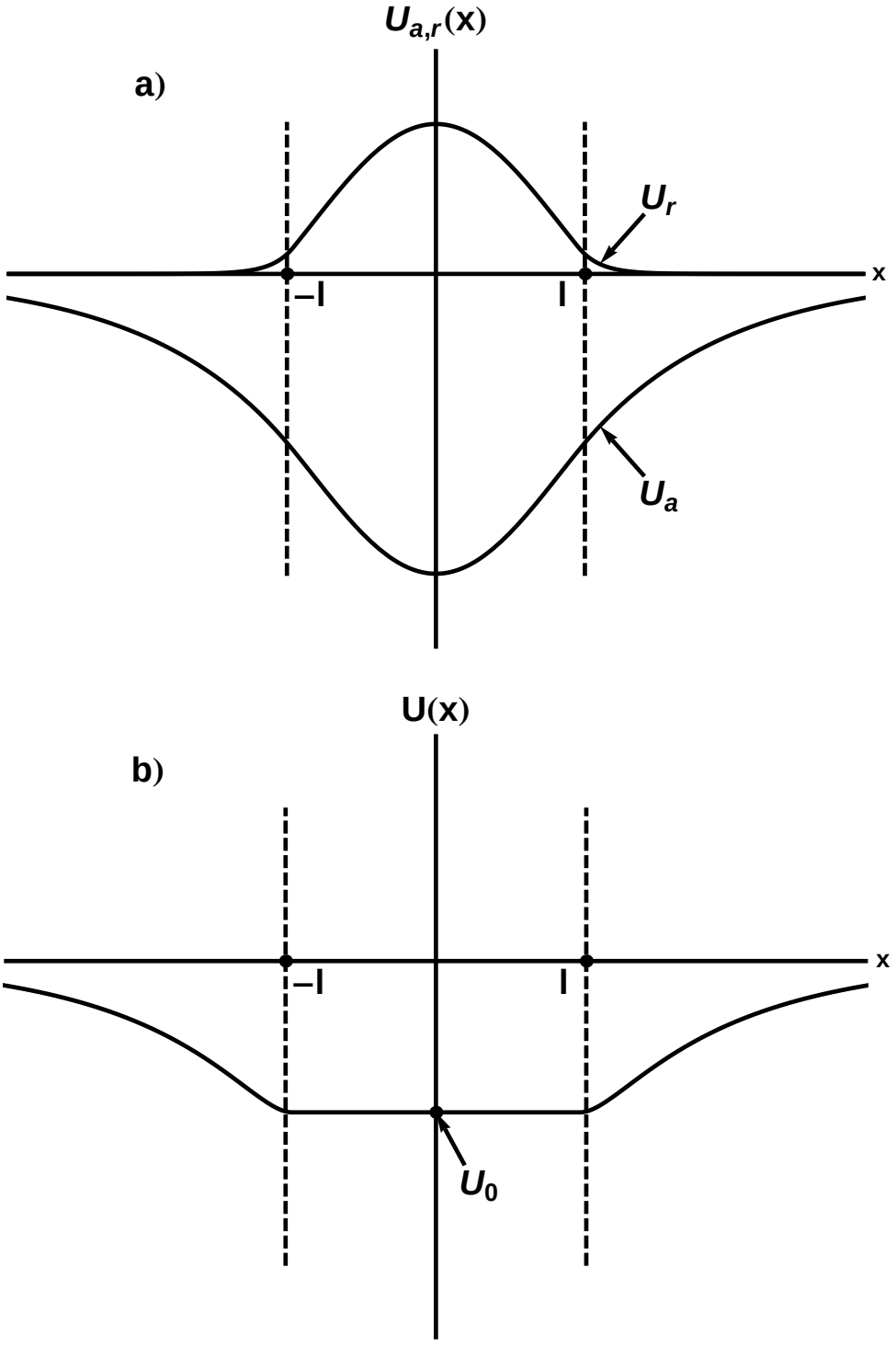

Figure 3.2: a) Illustration of the variation of $U_a(x)$ and $U_r(x)$ versus x. b) $U_a(x) + U_r(x) \equiv U(x)$ versus x.

It then follows from Eq. (3.3) or (3.4) that $\rho(x)$ also has this form, which we write as

$$\rho(x) = \rho_0 \left[1 - q(1 - \cos(\kappa x))\right], \quad \kappa^2 > 0, \tag{3.13}$$

$$\rho(x) = \rho_0 \left[1 - q(\cosh(\kappa' x) - 1)\right], \quad \kappa^2 < 0, \tag{3.14}$$

where we have introduced the two constants $\rho_0 \equiv \rho(0)$ and q. To avoid repetition, we concentrate on the case $\kappa^2 > 0$, since it will turn out that only in this case do solutions exist. For our considerations of the case $\kappa^2 > 0$, we require the parameter q to the range $q > 0$ to make Eq. (3.13) consistent with Fig. 3.1 (a). Substituting Eq. (3.13) into Eqns. (3.3) and (3.4), we obtain

$$U_a = -\rho_0 \left[\frac{u_r - u_a}{\kappa_r^2 - \kappa_a^2} q \cos(\kappa x) + \frac{u_a}{\kappa_a^2}(1 - q)\right] \tag{3.15}$$

$$U_r = \rho_0 \left[\frac{u_r - u_a}{\kappa_r^2 - \kappa_a^2} q \cos(\kappa x) + \frac{u_r}{\kappa_r^2}(1 - q)\right], \tag{3.16}$$

$$U_0 \equiv U_a + U_r = -\rho_0 \left(\frac{u_a}{\kappa_a^2} - \frac{u_r}{\kappa_r^2}\right)(1 - q). \tag{3.17}$$

We emphasize that Eqns. (3.13) – (3.17) apply only in the flock, $|x| < l$, and not in $|x| > l$.

In the range $|x| > l$, the relevant solutions to Eqns. (3.3) and (3.4) are $U_{a,r}(x) \sim \exp(-\kappa_{a,r}|x|)$. Furthermore, integration of Eqns. (3.3) and (3.4) across the flock boundary (i.e., from $x = l - \epsilon$ to $x = l + \epsilon$ with $\epsilon \to 0^+$) shows that $U_{a,r}$ and $dU_{a,r}/dx$ are continuous across the flock boundary. Thus

$$\left.\frac{dU_{a,r}(x)}{dx}\right|_{x=l} = -\kappa_{a,r} U_{a,r}(l). \tag{3.18}$$

As x increases through l, the density goes to zero, in general, discontinuously (as illustrated in Fig. 3.1(a)). Inserting solutions (3.15) and (3.16) for U_a and U_r into

Eq. (3.18), we arrive at two equations for the two unknowns, κl and q,

$$\kappa \sin(\kappa l) = \kappa_a \cos(\kappa l) + \frac{u_a}{u_a - u_r} \frac{\kappa_a^2 - \kappa_r^2}{\kappa_a} \left(q^{-1} - 1\right), \tag{3.19}$$

$$\kappa \sin(\kappa l) = \kappa_r \cos(\kappa l) + \frac{u_r}{u_a - u_r} \frac{\kappa_a^2 - \kappa_r^2}{\kappa_r} \left(q^{-1} - 1\right). \tag{3.20}$$

Combining Eqns. (3.19) and (3.20) to eliminate the factor $(q^{-1} - 1)$, we arrive at the following equation for the flock half-width, l,

$$\frac{\tan(\kappa l)}{\kappa} = \frac{u_r - u_a}{\kappa_r u_a - \kappa_a u_r}. \tag{3.21}$$

Similarly, if $\kappa^2 < 0$, we obtain

$$\frac{\tanh(\kappa' l)}{\kappa'} = \frac{u_r - u_a}{\kappa_r u_a - \kappa_a u_r}. \tag{3.22}$$

We now introduce the two positive dimensionless parameters,

$$\alpha_* = \frac{\kappa_a}{\kappa_r} \qquad \text{and} \qquad \beta_* = \frac{\kappa_r^2/u_r}{\kappa_a^2/u_a}, \tag{3.23}$$

in terms of which, κ^2 can be expressed as

$$\kappa^2/\kappa_r^2 = \alpha_*^2 \left(\frac{\beta_* - 1}{1 - \alpha_*^2 \beta_*} \right), \tag{3.24}$$

which conveniently splits $\alpha_* - \beta_*$ space into four regions where κ^2 has a definite sign. The regions are listed below for reference and are shown in Fig. 3.3.

Region I:	$\beta_* < 1$ and $\alpha_* > \frac{1}{\sqrt{\beta_*}}$ (or $\alpha_*^2 \beta_* > 1$), for which $\kappa^2 > 0$.
Region II:	$\beta_* > 1$ and $\alpha_* < \frac{1}{\sqrt{\beta_*}}$ (or $\alpha_*^2 \beta_* < 1$), for which $\kappa^2 > 0$.
Region III:	$\beta_* < 1$ and $\alpha_* < \frac{1}{\sqrt{\beta_*}}$, for which $\kappa^2 < 0$.
Region IV:	$\beta_* > 1$ and $\alpha_* > \frac{1}{\sqrt{\beta_*}}$, for which $\kappa^2 < 0$.

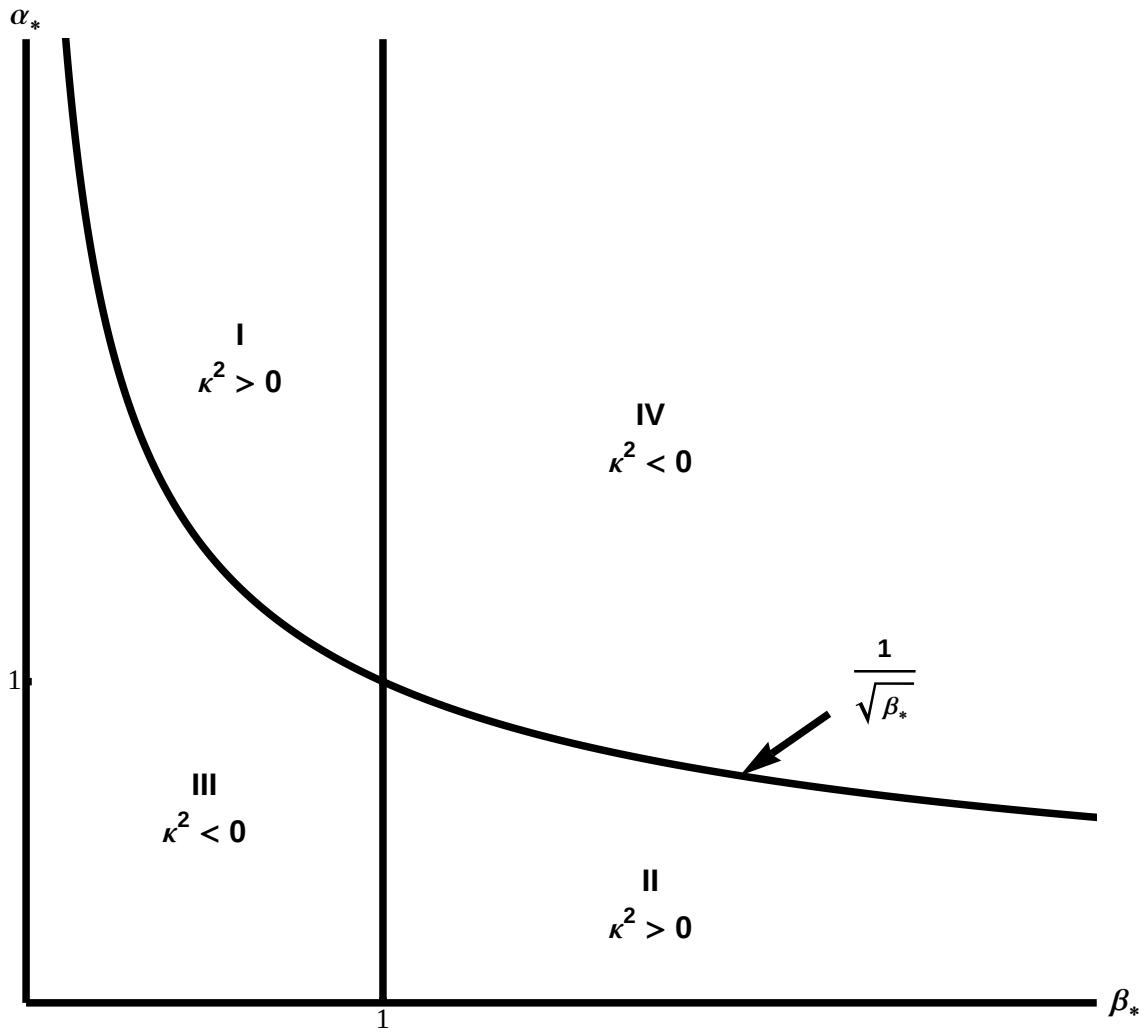

Figure 3.3: Graph of parameter space showing Regions I, II, III, and IV

We note that $[\tanh(\kappa' l)]/\kappa' > 0$ for all $l > 0$, while the right-hand side of Eq. (3.22) can be shown to be negative in Regions III and IV. Thus no solutions exist in Regions III and IV. Now considering Regions I and II for which $\kappa^2 > 0$, we write Eq. (3.21) in terms of the dimensionless variables α_* and β_*, and solve Eqns. (3.19) and (3.20) for the other unknown, q, to give

$$\tan(\kappa l)^2 = \frac{(1-\alpha_*^2\beta_*)(\beta_*-1)}{(\alpha_*\beta_*-1)^2}, \tag{3.25}$$

$$\left(\frac{1-q}{q}\right)^2 = \frac{(1-\alpha_*^2\beta_*)^2}{\beta_*(\alpha_*^2-1)^2}. \tag{3.26}$$

In Regions I and II, the right-hand side of Eq. (3.26) is always less than one. Thus $(1-q)^2 < q^2$ which implies that $q > 1/2$. Note that since q is positive, Eq. (3.13) implies that $\rho(x)$ is maximum at $x = 0$, as drawn in Fig. 3.1 (a). Setting $\kappa x = \pi$ in Eq. (3.13) yields $\rho = \rho_0(1-2q) < 0$ (since $q > 1/2$). Thus, starting from $x = 0$, the expression, Eq. (3.13), crosses zero before the argument of the cosine, κx, reaches π. Hence in order to avoid negative density, κl must be restricted to the range

$$0 < \kappa l \leq \pi. \tag{3.27}$$

We eliminate $\cos(\kappa l)$ from Eqns. (3.19) and (3.20) to obtain

$$\sin(\kappa l) = (1-q)\kappa\frac{\kappa_a + \kappa_r}{q\kappa_a\kappa_r}. \tag{3.28}$$

Since $0 < \kappa l \leq \pi$ and $q > 1/2$, the right-hand side of Eq. (3.28) is positive, and hence $1/2 < q < 1$. In addition, we require that $U_0 < 0$ (e.g., see Fig. 3.2), which, with $q < 1$ and by use of Eq. (3.17), implies that $\beta_* > 1$. Thus, of the four regions shown in Fig. 3.3, the only region for which valid solutions exist is Region II. We also note

that Region II is the only region that explicitly enforces Reynolds' conditions of long-range attraction and short-range repulsion by requiring $\alpha_* = \kappa_a/\kappa_r < 1$. Plots of the density $\rho(x)/\rho_0$ as a function of x/l are shown in Fig. 3.4 for different α_* values with $\beta_* = 4$ fixed. Note, from Fig. 3.3, that the largest α_* can be is $\alpha_* = 1/\sqrt{\beta_*} = 0.5$. Except for the case $\alpha_* = 0$, the flock density jumps discontinuously from a positive value at $x = l^-$ to zero at $x = l^+$.

What happens to our $T = 0$ solution with a sharp discontinuity when a positive temperature, $T > 0$, is introduced? The rest of this chapter investigates solutions of Eqns. (3.3) – (3.7) for low temperature, T.

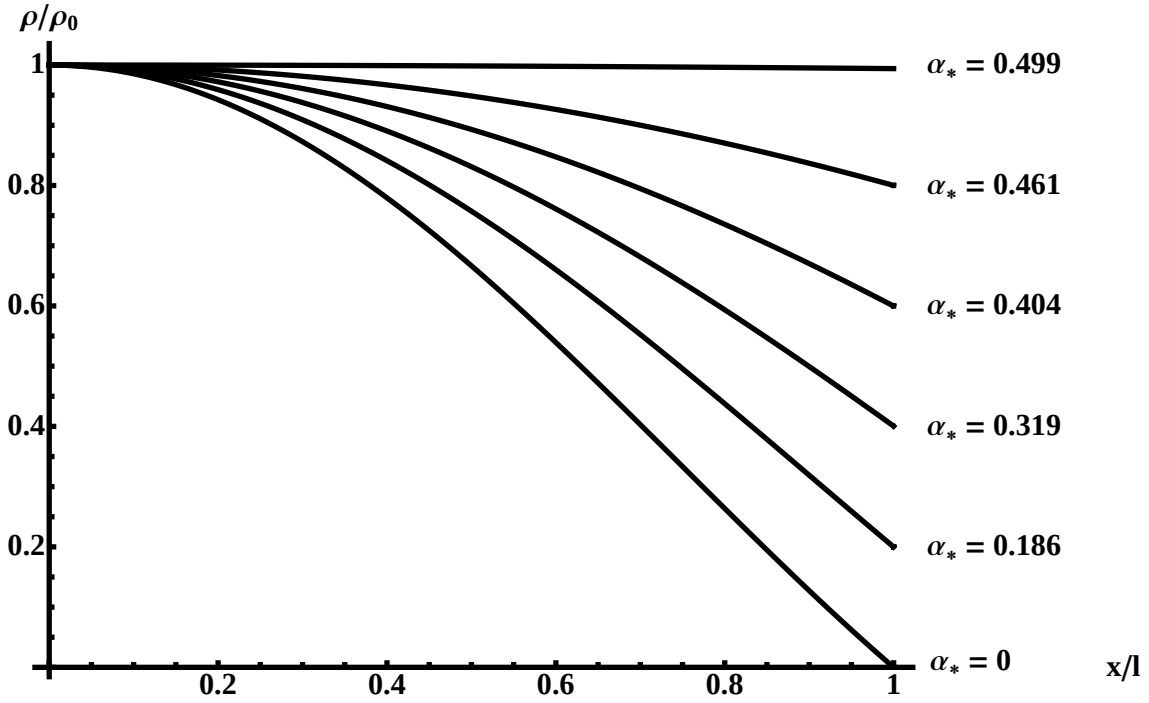

Figure 3.4: $\rho(x)/\rho_0$ versus x/l from solutions of the cold equations ($T = 0$) for various values of the parameter $\alpha_* = \kappa_a/\kappa_r$ and $\beta_* = \kappa_r^2 u_a/\kappa_a^2 u_r = 4$. The flock density at $x = l^-$ is $\rho(l^-)/\rho_0 = \frac{\alpha_*(\beta_*-1)}{1-\alpha_*^2\beta_*+(1-\alpha_*^2)\sqrt{\beta_*}}$.

3.3 Including Pressure

Rewriting Eq. (3.7) in terms of derivatives of ρ, we get

$$\frac{1}{\rho}\frac{dP}{d\rho} = -\frac{dU}{d\rho}, \tag{3.29}$$

where U is the sum of the attractive and repulsive potentials. Thus,

$$U = \text{const.} - \int \frac{P}{\rho^2}\, d\rho. \tag{3.30}$$

For our specific pressure, $P = \rho T$, this gives

$$U = U_a + U_r = U_\infty - T\ln(\rho/\rho_\infty), \tag{3.31}$$

where $U_\infty = U(\pm\infty)$ and $\rho_\infty = \rho(\pm\infty)$. Solving Eq. (3.31) for $\rho(x)$ we obtain

$$\rho(x) = \rho_\infty \exp\left(\frac{U_\infty - (U_a(x) + U_r(x))}{T}\right). \tag{3.32}$$

Defining

$$\hat{U}_{a,r}(\hat{x}) = U_{a,r}(\frac{\hat{x}}{\kappa_a})/T, \tag{3.33}$$

$$u_{r*} = \frac{u_r \rho_\infty \exp(U_\infty/T)}{T\kappa_r^2}, \tag{3.34}$$

$$\hat{x} = \kappa_a x, \tag{3.35}$$

we rewrite Eqns. (3.3) and (3.4) using the relation for the density (Eq. (3.32)), obtaining the following coupled equations for equilibrium,

$$\left(\alpha_*^2 \frac{d^2}{d\hat{x}^2} - 1\right)\hat{U}_r = -u_{r*}\exp\left(-\hat{U}_a - \hat{U}_r\right), \tag{3.36}$$

$$\left(\frac{d^2}{d\hat{x}^2} - 1\right)\hat{U}_a = \beta_* u_{r*}\exp\left(-\hat{U}_a - \hat{U}_r\right). \tag{3.37}$$

3.3.1 Analytical Solution in the Limit of Small $\alpha_* = \kappa_a/\kappa_r$

We can solve Eqns. (3.36) and (3.37) in the limit of a short-range repulsive potential, and a much longer-range, stronger, attractive potential, corresponding to $\alpha_* = 0$. In this limit, Eqns. (3.36) and (3.37) yield

$$\hat{U}_r \exp\left(\hat{U}_r\right) = u_{r*} \exp\left(-\hat{U}_a\right) \tag{3.38}$$

$$\left(\frac{d^2}{d\hat{x}^2} - 1\right) \hat{U}_a = \beta_* \hat{U}_r. \tag{3.39}$$

For $|x|/l \gg 1$, $\hat{U}_a(x)$ and $\hat{U}_r(x)$ become constants denoted $\hat{U}_{a\infty}$ and $\hat{U}_{r\infty}$. From Eq. (3.39),

$$\hat{U}_{a\infty} = -\beta_* \hat{U}_{r\infty}, \tag{3.40}$$

$$\hat{U}_\infty = \hat{U}_{a\infty} + \hat{U}_{r\infty} = -(\beta_* - 1)\hat{U}_{r\infty}. \tag{3.41}$$

Equation (3.38) then gives

$$u_{r*} = \hat{U}_{r\infty} \exp(\hat{U}_\infty) = \hat{U}_{r\infty} \exp\left(-(\beta_* - 1)\, \hat{U}_{r\infty}\right), \tag{3.42}$$

where we recall from §3.2 that $\beta_* > 1$, and from Eq. (3.34) that $u_{r*} > 0$. As $\hat{U}_{r\infty}$ increases from zero, the right-hand side of Eq. (3.42) increases from zero, reaches a maximum value, $u_{r*}^{\max}$, and then decreases to zero as $\hat{U}_{r\infty} \to \infty$. See Fig. 3.5. Thus,

$$u_{r*} < \frac{e^{-1}}{\beta_* - 1} = u_{r*}^{\max}. \tag{3.43}$$

For $0 < u_{r*} < u_{r*}^{\max}$, Eq. (3.42) has two solutions for $\hat{U}_{r\infty}$. We choose the solution that has a stable density at infinity. In Appendix C, using a linear stability analysis, we find that stability at $|x| = \infty$ requires that

$$\rho_\infty < \frac{T\kappa_r^2}{u_r} \left(\frac{1}{\beta_* - 1}\right), \tag{3.44}$$

which, from Eqns. (3.34) and (3.42), becomes

$$(\beta_* - 1)\hat{U}_{r\infty} < 1. \tag{3.45}$$

Now, taking the derivative of Eq. (3.42), we obtain

$$\frac{du_{r*}}{d\hat{U}_{r\infty}} = \left[1 - (\beta_* - 1)\hat{U}_{r\infty}\right] e^{\hat{U}_\infty}. \tag{3.46}$$

Thus, referring to Fig. 3.5, we see that the solution with $du_{r*}/d\hat{U}_{r\infty} > 0$ is stable,

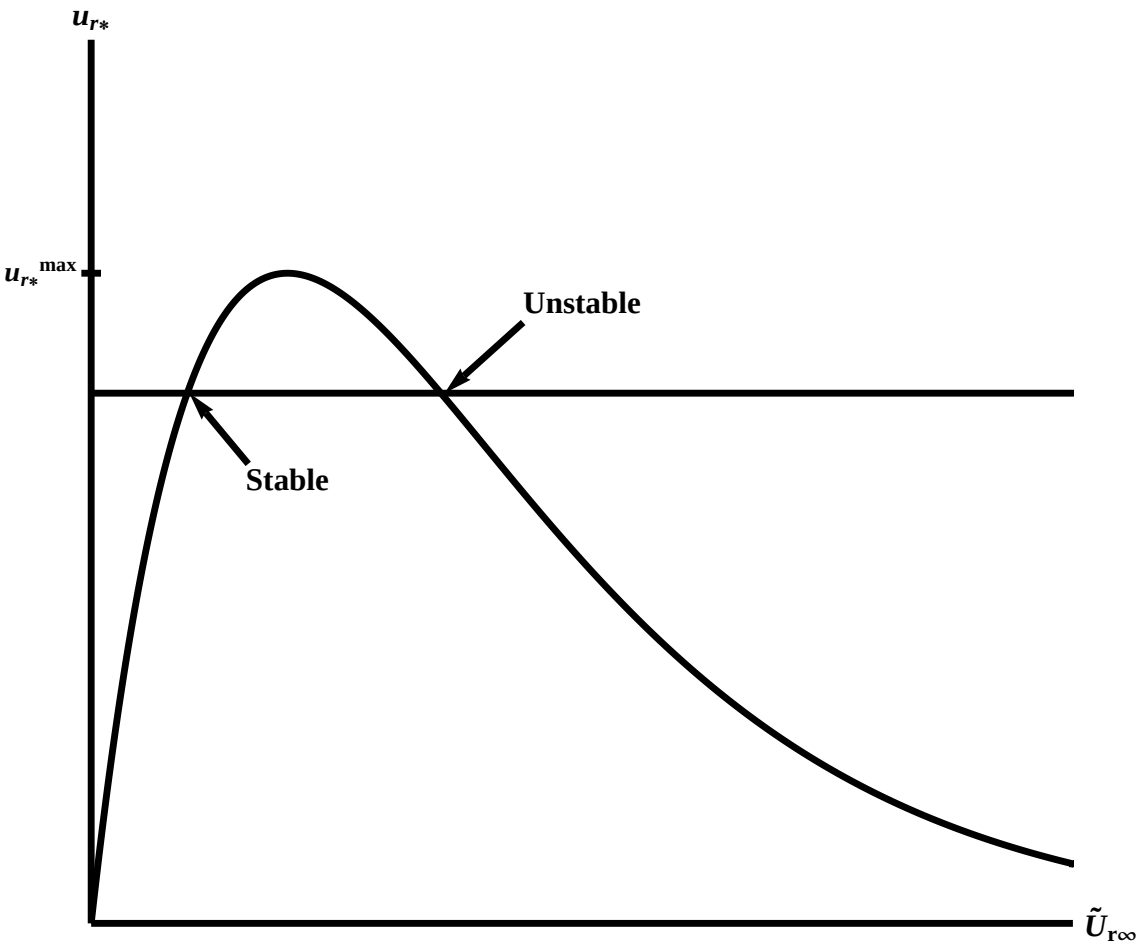

Figure 3.5: Graph of intersection of $u_{r*} = \text{const}$ and $\tilde{U}_{r\infty} \exp\left(-(\beta_* - 1)\,\tilde{U}_{r\infty}\right)$.

while the solution with $du_{r*}/d\hat{U}_{r\infty} < 0$ is unstable.

We now solve Eqns. (3.38), (3.39), and (3.32) for the density via quadrature (See Appendix D). Integrating Eq. (3.39) once, with respect $\hat{U}_a$,

$$\frac{1}{2}\left(\frac{d\hat{U}_a}{d\hat{x}}\right)^2 - \frac{\hat{U}_a^2 - \hat{U}_{a\infty}^2}{2} = \beta_* \int_{\hat{U}_{a\infty}}^{\hat{U}_a} \hat{U}_r \, d\hat{U}_a. \tag{3.47}$$

From Eq. (3.38),

$$\frac{d\hat{U}_a}{d\hat{U}_r} = -\left(1 + \frac{1}{\hat{U}_r}\right). \tag{3.48}$$

Using this in Eq. (3.47),

$$\begin{aligned} &\frac{1}{2}\left(1+\frac{1}{\hat{U}_r}\right)^2\left(\frac{d\hat{U}_r}{d\hat{x}}\right)^2 - \frac{1}{2}\left[\left(\hat{U}_r + \log\left(\frac{\hat{U}_r}{u_{r*}}\right)\right)^2 - \hat{U}_{a\infty}^2\right] \\ &= \beta_* \int_{\hat{U}_{r\infty}}^{\hat{U}_r} \hat{U}_r d\hat{U}_r \left(-\left(1+\frac{1}{\hat{U}_r}\right)\right) = -\beta_*\left(\frac{\hat{U}_r^2}{2} + \hat{U}_r\right)\Bigg|_{\hat{U}_{r\infty}}^{\hat{U}_r}. \end{aligned} \tag{3.49}$$

At the maximum, $\hat{U}_{rm}$, of the potential, $\hat{U}_r$, the derivative is zero and thus Eq. (3.49) reduces to

$$-\frac{1}{2}\left[\left(\hat{U}_{rm} + \log\left(\frac{\hat{U}_{rm}}{u_{r*}}\right)\right)^2 - \beta_*^2 \hat{U}_{r\infty}^2\right] = -\beta_*\left(\frac{\hat{U}_{rm}^2}{2} + \hat{U}_{rm}\right) - \beta_*\left(\frac{\hat{U}_{r\infty}^2}{2} + \hat{U}_{r\infty}\right) \tag{3.50}$$

where we have used Eq. (3.40). Thus, for fixed β_* and u_{r*}, Eqns. (3.50) and (3.42) can be numerically solved for $\hat{U}_{r\infty}$ and $\hat{U}_{rm}$. Once we have these, we solve Eq. (3.49) for $d\hat{U}_r/d\hat{x}$ and integrate the result from $\hat{U}_{r\infty}$ to $\hat{U}_r(\hat{x})$. Hence, the solution for the potential is given implicitly by

$$\hat{x} = \int_{\hat{U}_{r\infty}}^{\hat{U}_r(\hat{x})} \frac{(1+\hat{U}_r^{-1})\, d\hat{U}_r}{\left(2C_\infty + (1-\beta_*)\hat{U}_r^2 - 2\hat{U}_r(\beta_* - \log \hat{U}_r/u_{r*}) + \left(\log \hat{U}_r/u_{r*}\right)^2\right)^{1/2}}, \tag{3.51}$$

where

$$C_\infty = \beta_*(1-\beta_*)\frac{\hat{U}_{r\infty}^2}{2} + \beta_* \hat{U}_{r\infty}. \tag{3.52}$$

We integrate Eq. (3.51) numerically to obtain $\hat{U}_r(\hat{x})$. We then use Eqns. (3.38), (3.39), and (3.32) to find the density as a function of position.

By decreasing u_{r*}, we effectively decrease the temperature, and slowly turn off the pressure term. This can be seen through the definition of u_{r*} in Eq. (3.34),

$$u_{r*} = \frac{u_r \rho_\infty \exp(U_\infty/T)}{T\kappa_r^2}. \tag{3.53}$$

Since U_∞ is negative (see §3.2), as u_{r*} goes to zero, the temperature, T, will go to zero. In Fig. 3.6, we see that, as we decrease the temperature by decreasing the parameter u_{r*}, the $T \neq 0$ curves approach the cold solution, a cosine, in the limit where $T \to 0$. However, the approach only becomes apparent at extremely low values of T.

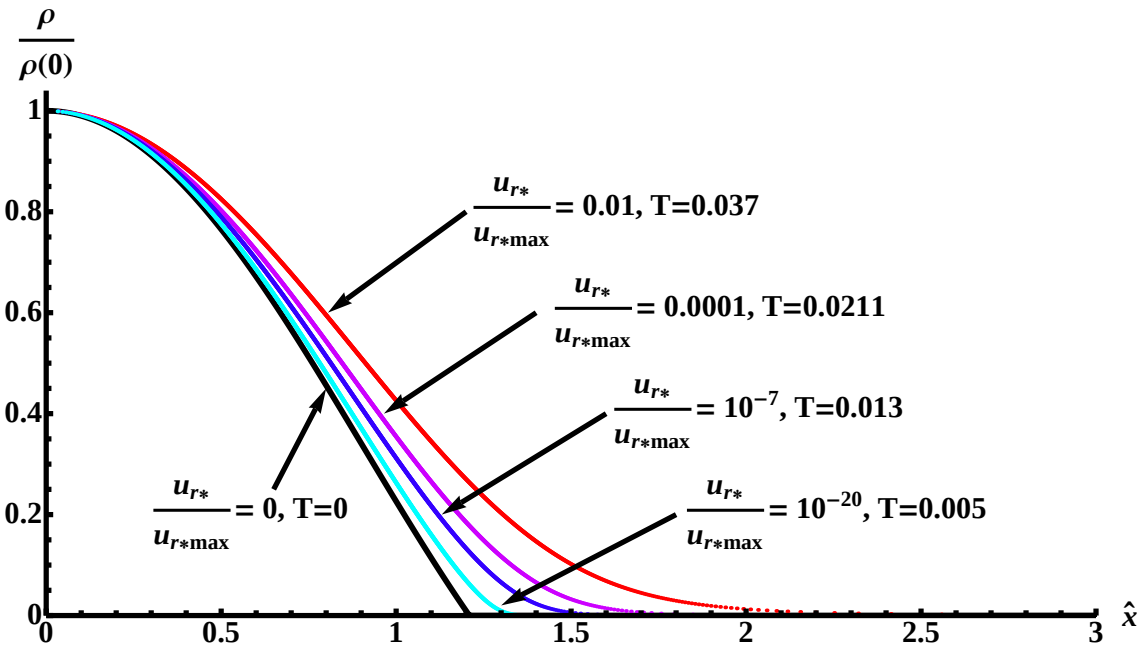

Figure 3.6: Correspondence to zero temperature limit with $\alpha_* = 0$, and $\beta_* = 4$. The convergence is convincing, but slow in u_{r*}.

3.3.2 Numerical Solutions for $\alpha_* \neq 0$

For the case of $\alpha_* \neq 0$, we must resort to numerical methods to find the density profile.

For this purpose, we now modify Eq. (3.6) by the introduction of a fictitious frictional force, νv, replacing the inertial term on the left-hand side,

$$\nu\, v = -\frac{\partial}{\partial x}\left(U_a + U_r\right) - \frac{T}{\rho}\frac{\partial}{\partial x}\rho, \tag{3.54}$$

where, as before, the velocity regulation term (proportional to τ^{-1}) has been omitted. We then numerically solve the time evolution for the system (with $\partial\rho/\partial t$ included); Eqns. (3.3), (3.4), (3.5), and (3.54). We find that numerical solutions of this fictitious dynamics produce solutions that rapidly relax to the equilibrium solutions. Using the method described in Appendix E, we evolve from a slightly perturbed initial constant density solution that is unstable according to Appendix C.

As we reduce the temperature, T, we are able to determine the nature of the approach to the cold solution. Figure 3.7(a) shows $\rho(x)$ versus x for successively smaller values of T. In the cold case, at the boundary of the flock, the density's derivative is a delta function. The approach to this situation is illustrated in Fig. 3.7(b) which shows $-d\rho/dx$ versus x for successively smaller values of T.

3.4 Discussion of Two and Three-Dimensional Equilibria

The main conclusions from our study of one-dimensional flock equilibria solutions of our continuum model are as follows.

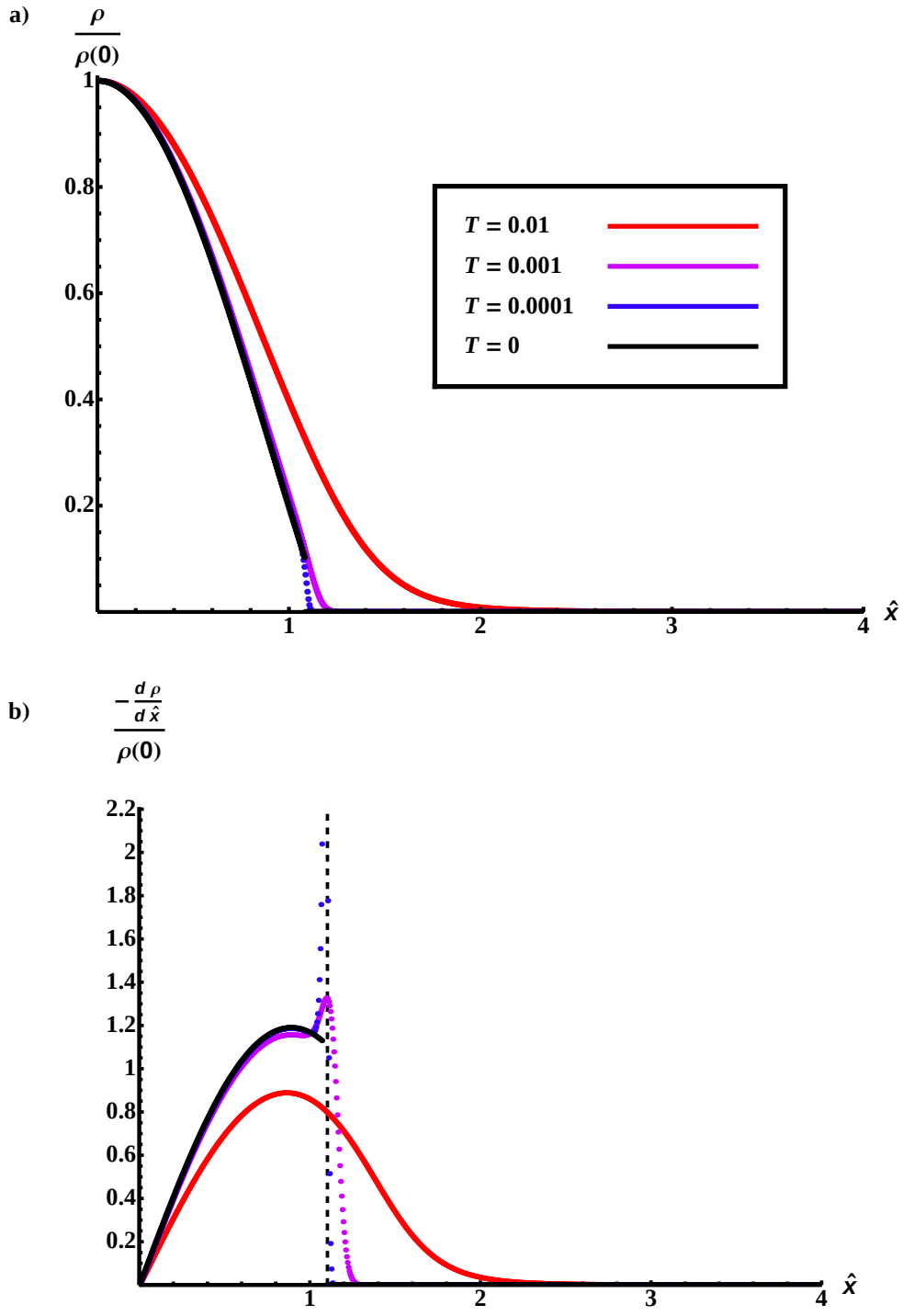

Figure 3.7: The correspondence to zero-temperature theory for $\alpha_* = 0.1$ and $\beta_* = 4$. T is labeled by color. a) $\rho/\rho(0)$ versus $\hat{x} = \kappa_a x$, b) $-(d\rho/d\hat{x})/\rho(0)$ versus $\hat{x}$.

1. In the absence of the isothermal pressure term (i.e., $T = 0$), we find equilibria with positive flock density in a finite region, $|x| < l$, and zero flock density in $|x| > l$.

2. For $T = 0$, the density at the flock edge, in general, jumps discontinuously to zero, $\rho(l^-) > 0$, $\rho(l^+) = 0$.

3. When an isothermal pressure is included ($T > 0$), the $T = 0$ solution is regularized in the sense that the discontinuity in $\rho(x)$ is removed and $\rho(x)$ now varies smoothly everywhere. However, now $\rho(x)$ remains positive for all x, decreasing monotonically from its maximum value to a positive (possibly small) value at $|x| = \infty$, $\rho(\pm\infty) = \rho_\infty > 0$.

In the next Chapter, we will show that conclusion (3) above also holds for another (non-isothermal) assumed form of the pressure $P(\rho)$. In the rest of this section, we argue that conclusions (1) – (3), obtained in our one-dimensional study, are also expected to apply for two-dimensional and three-dimensional equilibria.

To formulate models for flock equilibria in two-dimensions and in three-dimensions that are analogous to our one-dimensional model equations (Eqns. (3.1)–(3.4), (3.7)), we replace d/dx in Eq. (3.7) by the gradient operator, ∇, and we replace d^2/dx^2 in Eqns. (3.3) and (3.4) by the Laplacian operator, ∇^2. Denoting the radial coordinate in two-dimensions by $r = \sqrt{x^2 + y^2}$ and the radial coordinate in three-dimensions by

$R = \sqrt{x^2 + y^2 + z^2}$, we seek cylindrically- and spherically-symmetric flocks. Thus

$$\nabla = \begin{cases} \hat{\mathbf{r}} \dfrac{d}{dr} & \text{in two dimensions,} \\ \hat{\mathbf{R}} \dfrac{d}{dR} & \text{in three dimensions.} \end{cases} \tag{3.55}$$

$$\nabla^2 = \begin{cases} \dfrac{1}{r} \dfrac{d}{dr} r \dfrac{d}{dr} & \text{in two dimensions,} \\ \dfrac{1}{R^2} \dfrac{d}{dR} R^2 \dfrac{d}{dR} & \text{in three dimensions.} \end{cases} \tag{3.56}$$

With these choices, Eq. (3.9) becomes

$$U_{a,r} = \begin{cases} \int_0^\infty \hat{u}_{a,r}(r - r')\, \rho(r')\, 2\pi r'\, dr' \\ \qquad\qquad \text{in two dimensions,} \\ \int_0^\infty \hat{u}_{a,r}(R - R')\, \rho(R')\, 4\pi R'^2\, dR' \\ \qquad\qquad \text{in three dimensions,} \end{cases} \tag{3.57}$$

where

$$\hat{u}_{a,r} = \begin{cases} \mp \dfrac{u_{a,r}}{2\pi} K_0(\kappa_{a,r} r) & \text{in two dimensions} \\ \mp \dfrac{u_{a,r}}{4\pi R} \exp(-\kappa_{a,r} R) & \text{in three dimensions.} \end{cases} \tag{3.58}$$

Here $K_0(u)$ denotes a modified Bessel function of order zero ($K_0(u) \sim e^{-u}/\sqrt{u}$ for $u \gg 1$). Note that these choices for $\hat{u}_{a,r}$ correspond to the Green functions of the operator $(\nabla^2 - \kappa_{a,r}^2)$ in two and three dimensions, thus yielding Eqns. (3.3) and (3.4) with d^2/dx^2 replaced by ∇^2 (see, for example, [3] pg. 554).

We first outline how flock equilibria solutions can be obtained in the case $T = 0$ for two-dimensional, cylindrically-symmetric flocks and for three-dimensional, spherically-symmetric flocks. With $T = 0$, the analog of Eq. (3.7) is

$$\rho \nabla (U_a + U_r) = 0. \tag{3.59}$$

Thus, we can again seek solutions where $U_a + U_r = U_0 =$ constant (analogous to Eq. (3.8)) inside the flock ($r < l$ or $R < l$) and $\rho = 0$ outside the flock ($r > l$ or $R > l$). Equations (3.10) – (3.12) still apply with the replacement $d^2/dx^2 \to \nabla^2$. The analogs of the expressions for U_a and U_r, Eqns. (3.15) and (3.16), within the flock are

$$U_a = -\rho_0 \left[\frac{u_r - u_a}{\kappa_r^2 - \kappa_a^2} q J_0(\kappa r) + \frac{u_a}{\kappa_a^2}(1-q) \right], \tag{3.60}$$

$$U_r = \rho_0 \left[\frac{u_r - u_a}{\kappa_r^2 - \kappa_a^2} q J_0(\kappa r) + \frac{u_r}{\kappa_r^2}(1-q) \right], \tag{3.61}$$

in two dimensions, and

$$U_a = -\rho_0 \left[\frac{u_r - u_a}{\kappa_r^2 - \kappa_a^2} q \frac{\sin(\kappa R)}{R} + \frac{u_a}{\kappa_a^2}(1-q) \right], \tag{3.62}$$

$$U_r = \rho_0 \left[\frac{u_r - u_a}{\kappa_r^2 - \kappa_a^2} q \frac{\sin(\kappa R)}{R} + \frac{u_r}{\kappa_r^2}(1-q) \right], \tag{3.63}$$

in three dimensions where $J_0(u)$ denotes the Bessel function of order zero. Outside the flock, solutions of the equations for U_a and U_r with $\rho = 0$ (i.e., the modified Helmholtz equation, $\nabla^2 U_{a,r} - \kappa_{a,r}^2 U_{a,r} = 0$) show that, for $r > l$ or $R > l$, U_a and U_r behave like

$$U_{a,r}(r) \sim K_0(\kappa_{a,r} r), \tag{3.64}$$

$$U_{a,r}(R) \sim R^{-1} \exp(-\kappa_{a,r} R). \tag{3.65}$$

As before, we can now match the boundary conditions to obtain flock equilibria. The detailed analysis is not attempted here, but it can be expected that solutions qualitatively similar to our $T = 0$, one-dimensional analysis (e.g., Fig. 3.4) will result.

We now consider the introduction of the isothermal pressure term ($T > 0$). Since the term $T\nabla\rho$ is present in the equation analogous to Eq. (3.7), ρ cannot go discontinuously to zero, since this would imply a discontinuity in $U_a + U_r$, and such a discontinuity would be incompatible with Eqns. (3.57), which imply smooth variation of $U_{a,r}$ for bounded ρ. One might ask if it is possible to have a finite flock, $\int_0^\infty \rho(r)\, 2\pi r\, dr < \infty$ or $\int_0^\infty \rho(R)\, 4\pi R^2\, dR < \infty$. We note that these finite-ness conditions imply that $\rho \to 0$ as r or $R \to \infty$. However, this is not possible. In particular, since $\rho > 0$ everywhere for r or $R < \infty$, application of the force balance equation yields $\rho \sim \exp(-U/T)$. Thus, in order for $\rho \to 0$ as r or $R \to \infty$, we require that $U \to \infty$ as r or $R \to \infty$. But this is inconsistent with our integral equations for U_a and U_r for given bounded ρ, since, with our kernels, Eq. (3.58), these yield that U_a and U_r approach constants as r or $R \to \infty$ if the flock is confined ($\int_0^\infty \rho(r)\, 2\pi r\, dr < \infty$ or $\int_0^\infty \rho(R)\, 4\pi R^2\, dR < \infty$).

We conclude that the three major qualitative results applying for one-dimensional equilibria of our model, as listed at the beginning of this section, persist for equilibria in two or three dimensions.

3.5 Conclusions

If a pressure term is absent from the equilibrium flocking equations, we can solve explicitly for a solution. This solution generally exhibits a possible discontinuity at the edge of the flock. In addition, a specific region of phase space determines the only valid solutions for this type of equilibrium; $\beta_* > 1$, and $\alpha_*^2\beta_* < 1$, which

corresponds to long-range attraction and short-range repulsion.

In the second part of this chapter, we introduced a linear pressure, $P(\rho) = T\rho$. We find that this pressure regularizes the cold solution, i.e., the density becomes everywhere smooth. However, with finite temperature, the density does not decay to zero far from the flock, but instead approaches a (possibly small) constant value.

In the limit of a very short, repulsion length scale relative to the attractive length scale ($\alpha_* = \kappa_a/\kappa_r \to 0$), we find an analytical solution to the equilibrium equations with a pressure term and show that as the temperature is reduced, the solution approaches the cold solution. For non-zero α_*, we numerically converge on the equilibrium solution using a fictitious frictional dynamical process. These solutions also approach the cold solutions as the temperature is reduced. In this case (non-zero α_*), the zero-temperature density solution has a discontinuity, and the finite-temperature density solution has a sharper and sharper derivative near the flock boundary. In the next chapter, we find that, away from zero, larger temperatures give rise to multiple solution types, unlike the case for small temperatures.

Chapter 4

An Approach Toward Unifying Equilibria in Continuum Models for Flocking

4.1 Comparing two Models for Flocking

In this chapter, we investigate flock equilibria in two different continuum models of the interaction between members of the flock. In the first model there is an attractive potential between flock members and a pressure that depends nonlinearly on density that resists attraction. In the second model there is both an attractive and a repulsive potential as well as a pressure that depends linearly on density. We find that for some parameters, these two models coincide. Further, we show that both models admit solutions in the form of isolated flocks and nonlinear wave trains.

We first consider a nonlinear model with a flock pressure given by

$$P_{\mathrm{nl}}(\rho) = \frac{T\rho}{1-\rho/\rho_*}, \tag{4.1}$$

where $\rho < \rho_*$, and ρ_* is a constant upper bound on the density. As $\rho \to \rho_*$, the pressure diverges and the flock behaves incompressibly. The equations for a flock equilibrium are now (from Chapter 2)

$$\frac{d^2U}{dx^2} - \kappa_\rho^2 U = u_0\rho, \tag{4.2}$$

describing the attractive potential, and

$$\frac{dU}{dx} = -\frac{1}{\rho}\frac{dP_{\rm nl}}{dx} \tag{4.3}$$

describing force balance. Here the pressure is defined in Eq. (4.1).

We can rewrite these equations as a dimensionless set of equations with a single dimensionless parameter $\hat{\alpha}_{\rm nl}$ as

$$\frac{d^2\hat{U}}{d\hat{x}^2} - \hat{U} = \hat{\alpha}_{\rm nl}\hat{\rho}, \tag{4.4}$$

$$\frac{d\hat{U}}{d\hat{x}} = -\frac{1}{\hat{\rho}}\frac{d}{d\hat{x}}\left(\frac{\hat{\rho}}{1-\hat{\rho}}\right) \tag{4.5}$$

where $\hat{\rho} = \rho/\rho_*$, $\hat{x} = \kappa_\rho x$, $\hat{U} = U/T$, and

$$\hat{\alpha}_{\rm nl} = u_0\rho_*/\kappa_\rho^2 T. \tag{4.6}$$

This gives us the general form,

$$\frac{d^2\hat{U}}{d\hat{x}^2} - \hat{U} = \hat{\alpha}_{\rm nl}\hat{\rho}, \tag{4.7}$$

$$\frac{d\hat{U}}{d\hat{x}} = -\frac{1}{\hat{\rho}}\frac{d}{d\hat{x}}\hat{P}_{\rm nl}(\hat{\rho}) \tag{4.8}$$

with

$$\hat{P}_{\rm nl}(\hat{\rho}) = \frac{\hat{\rho}}{1-\hat{\rho}}. \tag{4.9}$$

We now compare the above formulation to the model we encountered in the last chapter (Eqns. (3.3) – (3.7)). There we considered a model for flocking that involved both a long-range attractive and short-range repulsive potential. The governing equilibrium equations in this model are

$$\frac{d^2U_a}{dx^2} - \kappa_a^2 U_a = u_{a0}\rho, \tag{4.10}$$

$$\frac{d^2U_r}{dx^2} - \kappa_r^2 U_r = -u_{r0}\rho, \tag{4.11}$$

and

$$\frac{d}{dx}\left(U_a + U_r\right) = -\frac{1}{\rho}\frac{d}{dx}P(\rho). \tag{4.12}$$

Here, U_a and U_r are the attractive and repulsive potentials respectively and $P(\rho) = T\rho$, an ideal-gas flock pressure. As before, the parameters u_{a0} and u_{r0} are the strengths of the potentials and κ_a^{-1} and κ_r^{-1} are the respective screening length scales. We are interested in the limit where the repulsive potential has a short-range compared with the attractive potential, i.e., $\kappa_a/\kappa_r \to 0$. In this limit the equations reduce to

$$\frac{d^2U_a}{d\hat{x}^2} - U_a = \frac{u_{a0}}{\kappa_a^2}\rho \tag{4.13}$$

$$U_r = \frac{u_{r0}}{\kappa_r^2}\rho \tag{4.14}$$

$$\frac{d}{d\hat{x}}\left(U_a + U_r\right) = -\frac{1}{\rho}\frac{d}{d\hat{x}}P_1(\rho). \tag{4.15}$$

where we have made the change of independent variable $\hat{x} = \kappa_a x$. Substituting Eq. (4.14) and $P_1(\rho) = T\rho$ into Eq. (4.15), we obtain

$$\frac{dU_a}{d\hat{x}} = -T\frac{1}{\rho}\frac{d\rho}{d\hat{x}} - \frac{u_{r0}}{\kappa_r^2}\frac{d\rho}{d\hat{x}}. \tag{4.16}$$

Here, similar to the nonlinear model, we may non-dimensionalize using $\hat{x} = \kappa_a x$, $\hat{U} = U_a/T$. We normalize the density such that

$$\hat{\rho} = \rho u_{r0}/2\kappa_r^2 T, \tag{4.17}$$

which results in the pair of equations,

$$\frac{d^2\hat{U}}{d\hat{x}^2} - \hat{U} = \hat{\alpha}_1\hat{\rho}, \tag{4.18}$$

and

$$\frac{d\hat{U}}{d\hat{x}} = -\frac{1}{\hat{\rho}}\frac{d\hat{\rho}}{d\hat{x}} - 2\frac{d\hat{\rho}}{d\hat{x}}, \tag{4.19}$$

where $\hat{\alpha}_{\rm l}$ is given by

$$\hat{\alpha}_{\rm l} = 2u_{a0}\kappa_r^2/u_{r0}\kappa_a^2. \tag{4.20}$$

From Eq. (4.19) we may identify an effective pressure,

$$\hat{P}_{\rm eff}(\hat{\rho}) = \hat{\rho} + \hat{\rho}^2, \tag{4.21}$$

such that

$$\frac{d\hat{U}}{d\hat{x}} = -\frac{1}{\hat{\rho}}\frac{d\hat{P}_{\rm eff}}{d\hat{x}}. \tag{4.22}$$

The choice of normalizing density in this model was made so that the effective pressure in this model corresponds to the low-density limit of the nonlinear pressure model, Eq. (4.9). This suggests the two models should agree in the low-density limit when $\hat{\alpha}_{\rm nl} = \hat{\alpha}_{\rm l}$, where $\hat{\alpha}_{\rm nl}$ and $\hat{\alpha}_{\rm l}$ are given by Eqns. (4.6) and (4.20).

Since we have reduced the two models to the same general form we can now analyze them together.

4.2 General Method

We solve for the flock density in a general class of one-dimensional models that contain a differentiable pressure and an attractive, pairwise potential. Suppose we have a model that can be expressed as the set of dimensionless differential equations

$$\frac{d^2U}{dx^2} - U = \alpha\rho \tag{4.23}$$

$$\frac{dU}{dx} = -\frac{1}{\rho}\frac{dP(\rho)}{dx}. \tag{4.24}$$

where the first equation describes the pairwise attraction between flock members and the second equation describes the force balance between this potential and the pressure. Here, ρ measures the number density of flock members, and the dimensionless parameter α measures relative strength of the pressure to the potential. To find a solution of this system, we write the second equation as

$$\frac{dU}{d\rho} = -\frac{1}{\rho}\frac{dP}{d\rho}. \tag{4.25}$$

Integrating this once we get

$$U = -\int^{\rho} \frac{1}{\rho}\frac{dP}{d\rho} d\rho + C_1 = U_\rho(\rho) + C_1. \tag{4.26}$$

with one constant of integration C_1. Additionally, we define U_ρ as

$$U_\rho = -\int^{\rho} \frac{1}{\rho}\frac{dP}{d\rho} d\rho. \tag{4.27}$$

We now solve the second-order differential equation, Eq. (4.23), by quadrature (see Appendix D). We rewrite Eq. (4.23) using the fundamental theorem of calculus and the chain rule to give

$$\frac{d}{dx}\frac{1}{2}\left(\frac{dU}{dx}\right)^2 = \frac{dU}{dx}\frac{d}{dU}\left(\frac{U^2}{2} + \alpha\int^{U} \rho\, dU\right). \tag{4.28}$$

This gives

$$\frac{d}{dx}\left[\frac{1}{2}\left(\frac{dU}{dx}\right)^2\right] = \frac{d}{dx}\left[\frac{U^2}{2} + \alpha\int^{U} \rho\, dU\right]. \tag{4.29}$$

Integrating once, we get

$$\frac{1}{2}\left(\frac{dU}{dx}\right)^2 = \frac{U^2}{2} + \alpha\int^{U} \rho dU + C_2, \tag{4.30}$$

where C_2 is another constant of integration. Using Eq. (4.25) we can rewrite the integral as

$$\alpha \int^{U} \rho dU = -\alpha \int^{\rho} \frac{dP(\rho)}{d\rho} d\rho = -\alpha P(\rho). \tag{4.31}$$

Substituting this back into Eq. (4.30), we get

$$\frac{1}{2}\left(\frac{dU}{dx}\right)^2 = \frac{U^2}{2} - \alpha P(\rho) + C_2. \tag{4.32}$$

We can express the derivative on the left-hand side using Eq. (4.25) as,

$$\frac{dU}{dx} = \frac{dU}{d\rho}\frac{d\rho}{dx} = -\frac{1}{\rho}\frac{dP}{d\rho}\frac{d\rho}{dx}, \tag{4.33}$$

which then gives us

$$\frac{1}{2}\left(\frac{1}{\rho}\frac{dP}{d\rho}\right)^2\left(\frac{d\rho}{dx}\right)^2 = \frac{U^2}{2} - \alpha P(\rho) + C_2. \tag{4.34}$$

If we isolate the derivative and using the definition of U, Eq. (4.26), we arrive at

$$\frac{1}{2}\left(\frac{d\rho}{dx}\right)^2 = \Phi(\rho;\alpha,C_1,C_2) \equiv \frac{\left[\left(U_\rho(\rho)+C_1\right)^2/2 - \alpha P(\rho) + C_2\right]\rho^2}{\left(dP/d\rho\right)^2}, \tag{4.35}$$

with $U_\rho(\rho)$ given by Eq. (4.27).

We have indicated the parametric dependence of the potential, Φ, on α, C_1, and C_2 by a semicolon. Equation (4.35) is a first-order, second-degree, nonlinear, autonomous differential equation that is formally identical to that of a particle moving in a one-dimensional potential, $-\Phi$. The density, ρ, plays the role of the position of the particle, and x acts as time. In the next section we explicitly integrate Eq. (4.35) for the two models introduced earlier in this chapter.

4.2.1 Boundary Conditions and Equilibria

In order to specify a unique potential, Φ, in Eq. (4.35), the three parameters α, C_1, and C_2 need to be specified. For the two specific models above, α is a dimensionless parameter that compares the strength of the attraction to that of the pressure and is determined by the properties of the members of the flock. The integration constants C_1 and C_2 are, in principle, determined by boundary conditions and the total number of individuals in the flock. Alternatively, if we consider two densities ρ_1 and ρ_2 that are roots of $\Phi = 0$, we can specify the constants C_1 and C_2 in terms of these densities. Through Eq. (4.35), we see that if at a density ρ_1, $\Phi(\rho_1) = 0$, then the derivative of the density is zero at the specific position, x, that corresponds to ρ_1. Hence, the densities ρ_1 and ρ_2 correspond to maxima and minima of the density profile.

To convert Eq. (4.35) from $\Phi(\rho; \alpha, C_1, C_2)$ to $\Phi(\rho; \alpha, \rho_1, \rho_2)$, we force Φ to be zero at these specific densities. First we choose

$$C_2(\rho_1, \rho_2) = -\frac{\left[U_\rho(\rho_1) + C_1(\rho_1, \rho_2)\right]^2}{2} + \alpha P(\rho_1), \tag{4.36}$$

so that $\Phi(\rho_1) = 0$. Similarly, we may plug this into Eq. (4.35), with $\rho = \rho_2$, to get a condition on C_1,

$$\frac{\left[U_\rho(\rho_2) + C_1(\rho_1, \rho_2)\right]^2}{2} - \alpha P(\rho_2) - \frac{\left[U_\rho(\rho_1) + C_1(\rho_1, \rho_2)\right]^2}{2} + \alpha P(\rho_1) = 0, \tag{4.37}$$

which gives

$$C_1(\rho_1, \rho_2) = \frac{U_\rho(\rho_1)^2/2 - U_\rho(\rho_2)^2/2 - \alpha P(\rho_1) + \alpha P(\rho_2)}{U_\rho(\rho_2) - U_\rho(\rho_1)}. \tag{4.38}$$

Equation (4.38) applies to the case where ρ_1 and ρ_2 are distinct. The solutions for $\rho(x)$ in this case are of the form of nonlinear waves where $\rho(x)$ varies periodically between ρ_1 and ρ_2. Because the potential has a simple root at these densities, the distance between the maxima and minima is finite. For a solution to have a single maximum, the value of density as $x \to \infty$ must correspond to a double root of Φ. Thus, when $\rho_1 = \rho_2 = \rho_\infty$, we can solve for the constants

$$C_{1\,\infty}(\alpha, \rho_\infty) = -\alpha\rho_\infty - U_\rho(\rho_\infty), \tag{4.39}$$

$$C_{2\,\infty}(\alpha, \rho_\infty) = -\frac{(\alpha\rho_\infty)^2}{2} + \alpha P(\rho_\infty), \tag{4.40}$$

where ρ_∞ is the double root of Φ.

An example of the potential in the form of a plot of $d\rho/dx = \sqrt{2\Phi}$ is shown in Fig. 4.1 for the nonlinear pressure model (Eq. (4.9)). In this figure, $\rho_1 = \rho_2 = 0.1$ and several values of α are considered. Note that in this case, depending on the value of α, there are a number of other values of ρ where $\Phi(\rho)$ vanishes. These values will be important in determining the nature of the solution, $\rho(x)$.

Determination of the density profile, $\rho(x)$, requires integrating the square root of Eq. (4.35) over a range of ρ values for which $\Phi(\rho) > 0$,

$$(x - x_0) = \pm \int_\rho^{\rho_c} \frac{d\rho}{(2\Phi(\rho; \alpha, \rho_1, \rho_2))^{1/2}}. \tag{4.41}$$

Equation (4.41) must then be inverted to find $\rho(x - x_0)$. Here ρ_c is a root of $\Phi(\rho)$; an upper endpoint for a region of positive $\Phi(\rho)$. The value of x_0 is arbitrary because the solution of the autonomous differential equation, Eq. (4.35), may be shifted with respect to the x coordinate resulting in another solution.

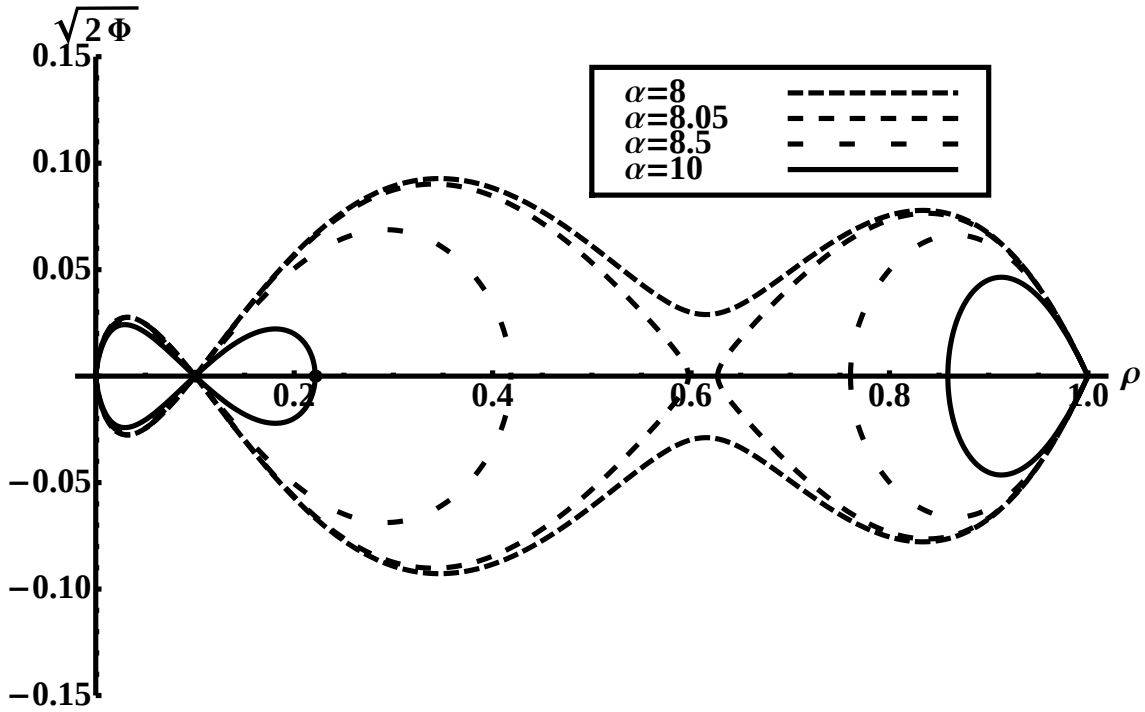

Figure 4.1: This shows several valid potentials, $\sqrt{2\Phi}$, for a model with a nonlinear pressure. Here we have chosen $\rho_1 = \rho_2 = \rho_\infty = 0.1$.

In general, a solution is generated by integrating Eq. (4.41) from one root of Φ to another root of Φ in a region of positive Φ. The nature of the solution depends on the way $\Phi \to 0$ as ρ approaches a root of Φ.

One of two types of endpoints can be encountered. First, if the limit

$$x = \lim_{R \to \rho_c^-} \int_\rho^R \frac{d\rho}{\left(2\Phi(\rho; \alpha, \rho_1, \rho_2)\right)^{1/2}} \tag{4.42}$$

converges, then the position coordinate, x, will be finite and the density will reach ρ_c in finite spatial extent. This coordinate can, without loss of generality, be taken as the origin. We will call these endpoints 'convergent'.

If the limit diverges, then the density takes an infinite spatial extent to reach ρ_c. In this case we refer to these endpoints as 'divergent'.

In practice, we start the integration in the middle of two endpoints, integrate away from the midpoint, and piece the solution together depending on the types of endpoints.

There are, in general, four types of non-constant, bounded solutions, enumerated by **dc**, **dd**, **cd**, and **cc**. These are shown in Fig. 4.2, and we will briefly describe them below.

dc This type of equilibrium, seen in Fig. 4.2 (a), consists of a divergent endpoint at a lower density and a convergent endpoint at a higher density. This produces a type of solution that reaches the higher density in finite spatial extent. Hence, without loss of generality, solutions of this form will start at the lower density at $x = -\infty$, and reach the higher density at the origin. At this classical turning point, the solution the descends back down to the lower value of ρ at $x = \infty$.

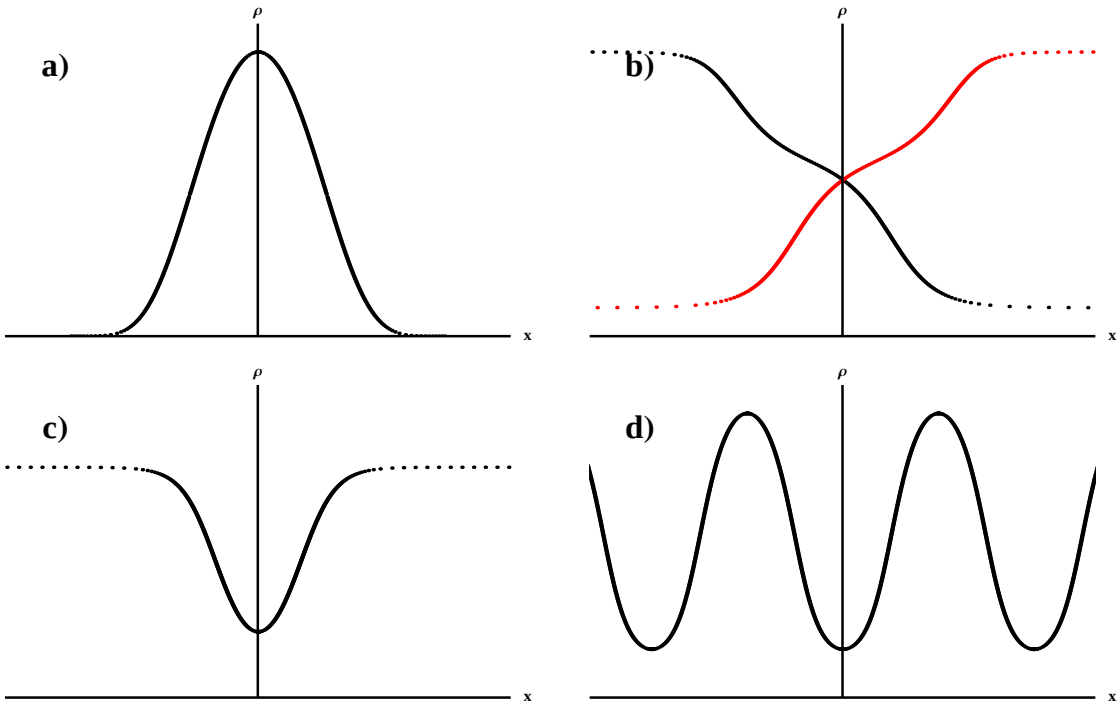

Figure 4.2: The four density profile solution types. a) This solution has a divergent lower endpoint and a convergent upper endpoint. b) This solution is a shock produced from a divergent endpoint at both the upper and lower endpoint densities. The red curve is the equivalent solution using the other sign of the square root. c) This solution is a depression in the middle of a constant density solution. The upper endpoint is divergent whereas the lower endpoint is convergent. d) This solution produces waves generated by a convergent upper endpoint and a convergent lower endpoint.

The descending part of the equilibrium is obtained by taking the negative root when separating Eq. (4.35). A solution of this type with the divergent endpoint at $\rho = 0$ is technically a solution to the differential equation, but not a physical solution because the potential U must, necessarily, go to infinity where the density goes to zero for this type of solution. A physical attractive potential must go to a constant, so solutions with lower endpoints of $\rho = 0$ are unphysical.

dd This type of equilibrium, seen in Fig. 4.2 (b), starts at a lower divergent endpoint at $x = -\infty$, pass through the midpoint of the endpoints at $x = 0$, and approach the upper divergent endpoint at $x = \infty$. Conversely, there is another solution that starts at the upper endpoint and descends to the lower endpoint.

cd This type of equilibrium, seen in Fig. 4.2 (c), is very similar to **dc** in that it is composed of a convergent and a divergent endpoint, but in this case, the convergent endpoint is lower than the divergent endpoint. This means that solutions of this form start at the upper endpoint at $x = -\infty$, and descend to the lower density endpoint at the origin. At this classical turning point, the solution ascends till $x = \infty$, approaching the upper endpoint.

cc This is perhaps the most interesting type of equilibrium. At both upper and lower density endpoints, the solution has two classical turning points, one at the lower density, and one at the upper density. The solution oscillates between these turning points, representing waves within the flock equilibrium.

An example of this can be seen in Fig. 4.2 (d).

Although it seems plausible that a solution might exist that starts in one region between two endpoints, reaches a convergent endpoint in finite extent, and then continues through the convergent endpoint point into a higher (or lower) region of solution space; this does not occur. The reason for this is as follows. In order for the integral to converge at that point, Φ must cross through the root, and cannot stay positive past the root. If it were to be a root of Φ and also stay positive past the root, it must be at least quadratic near the root, and thus the integral of $1/\sqrt{2\Phi}$ would diverge at this point.

Given a set of parameters, Φ might have several roots, and thus a variety of solution types might be possible at different densities.

Below, we explore the two one-dimensional models we introduced in the beginning of the chapter. The first was a model with a nonlinear pressure.

4.3 Nonlinear Pressure

Using the general procedure, we identify U_ρ as

$$U_\rho = -\int^\rho \frac{1}{\rho}\frac{dP_{\rm nl}}{d\rho}d\rho = -\int \frac{1}{\rho}\frac{d}{d\rho}\left(\frac{\rho}{1-\rho}\right)d\rho \tag{4.43}$$

using the dimensionless form for the pressure,

$$P_{\rm nl} = \frac{\rho}{1-\rho}, \tag{4.44}$$

where we have dropped the ˆs. We can integrate this by parts to get an explicit expression for $U_\rho(\rho)$,

$$U_\rho(\rho) = -\int \frac{1}{\rho}\frac{d}{d\rho}\left(\frac{\rho}{1-\rho}\right) d\rho \tag{4.45}$$

$$= -\frac{1}{\rho}\left(\frac{\rho}{1-\rho}\right)\Bigg|^{\rho} + \int \frac{1}{\rho^2}\left(\frac{\rho}{1-\rho}\right) d\rho \tag{4.46}$$

$$= -\left(\frac{1}{1-\rho}\right)\Bigg|^{\rho} - \int \left(\frac{1}{\rho} + \frac{1}{1-\rho}\right) d\rho \tag{4.47}$$

$$= -\left(\frac{1}{1-\rho} + \log\left(\frac{\rho}{1-\rho}\right)\right). \tag{4.48}$$

Using

$$\frac{\partial}{\partial\rho}\frac{\rho}{1-\rho} = \frac{1}{(1-\rho)^2} \tag{4.49}$$

we now explicitly write the potential Φ for this model. Plugging in the appropriate definitions into Eq. (4.35), we get

$$\Phi_{\rm nl}(\rho;\alpha,\rho_1,\rho_2) = \left[\frac{\left(U_\rho(\rho) + C_1(\rho_1,\rho_2)\right)\right)^2}{2} - \alpha\frac{\rho}{1-\rho} + C_2(\rho_1,\rho_2)\right]\rho^2(1-\rho)^4, \tag{4.50}$$

with

$$U_\rho(\rho) = -\left(\frac{1}{1-\rho} + \log\left(\frac{\rho}{1-\rho}\right)\right). \tag{4.51}$$

Examples of this potential for various parameters (α, ρ_1, and ρ_2) can be seen in Fig. 4.1.

In Fig. 4.3, 4.4, 4.5, and 4.6, we see various slices of parameter space. The regions in parameters space correspond to the number of solution regions.

Most of the richness of solutions can be seen in the subspace where $\rho_1 = \rho_2$. In this case, we use $C_{1\infty}$ and $C_{2\infty}$ from Eqns. (4.39) and (4.40). For what follows,

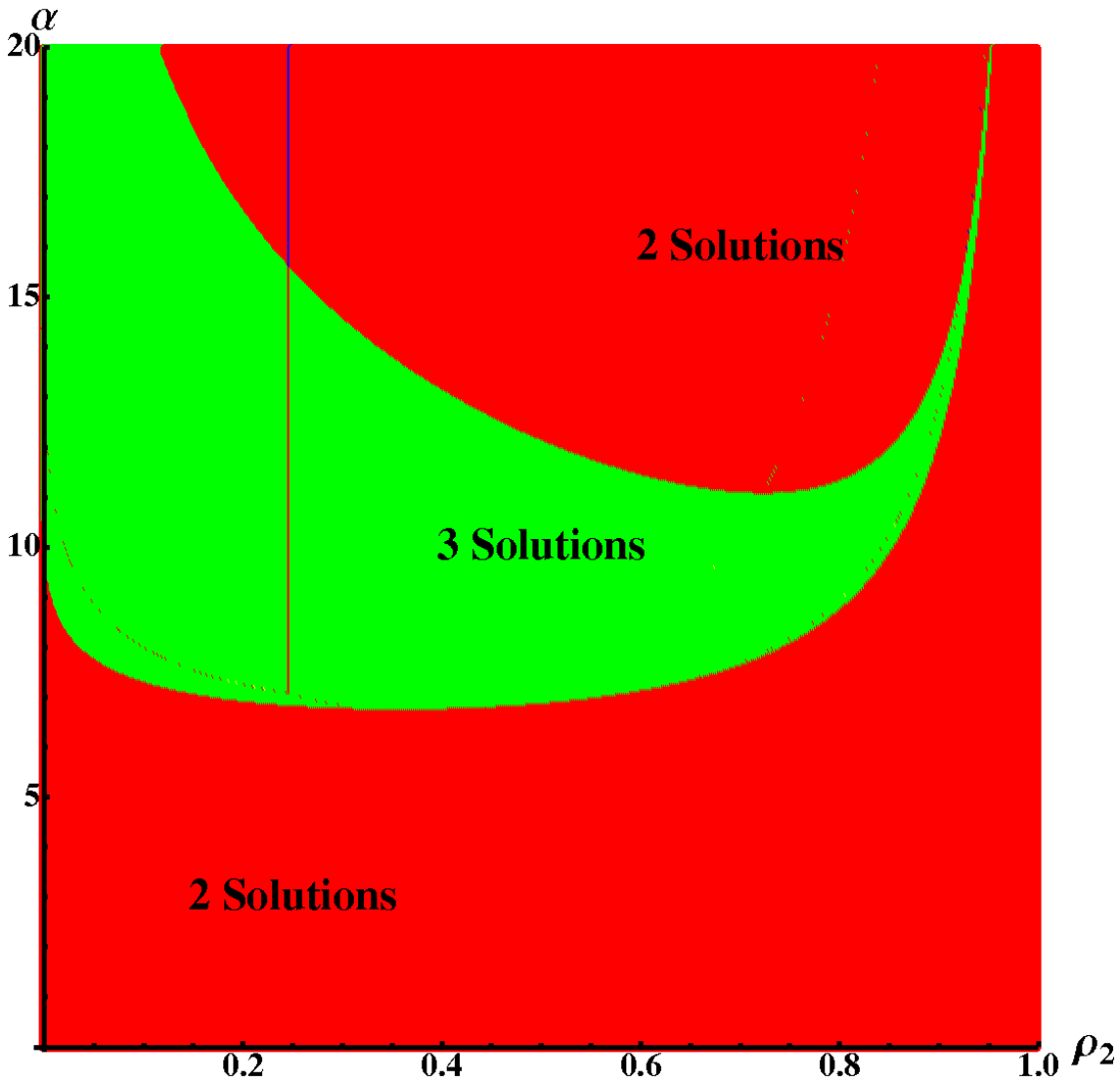

Figure 4.3: Cross section of parameter space of nonlinear model where $\rho_1 = 0.25$. The vertical axis is the parameter $\alpha = \hat{\alpha}_{\rm nl} = u_0\rho_*/\kappa_\rho^2 T$ (Eq. (4.6)), and the horizontal axis is ρ_2. Black corresponds to no solutions, blue corresponds to one solution, red corresponds to two solutions, and green corresponds to three solutions present for the parameter set.

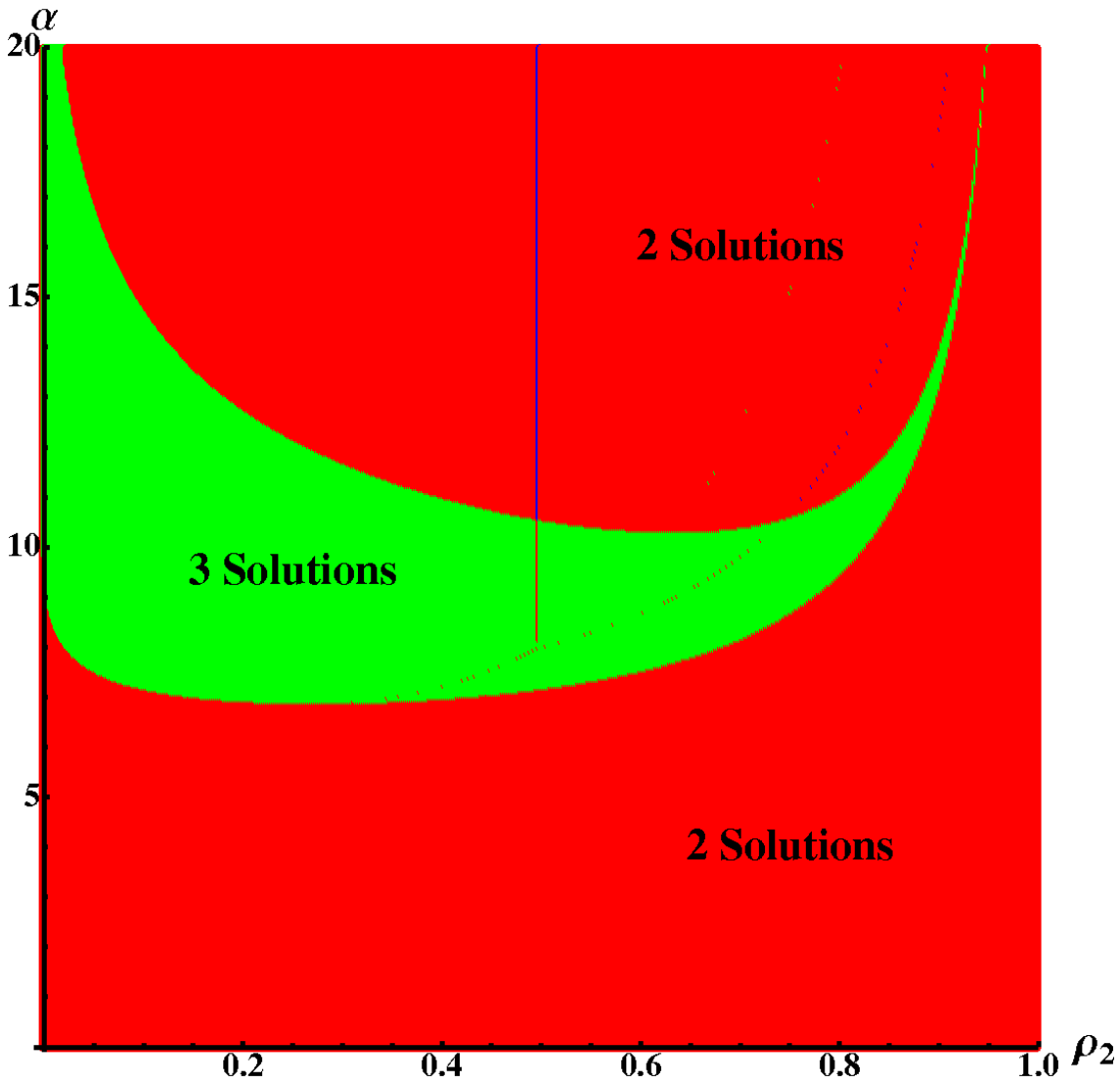

Figure 4.4: Cross section of parameter space of nonlinear model where $\rho_1 = 0.5$. The vertical axis is the parameter $\alpha = \hat{\alpha}_{\rm nl} = u_0\rho_*/\kappa_\rho^2 T$ (Eq. (4.6)), and the horizontal axis is ρ_2. Black corresponds to no solutions, blue corresponds to one solution, red corresponds to two solutions, and green corresponds to three solutions present for the parameter set.

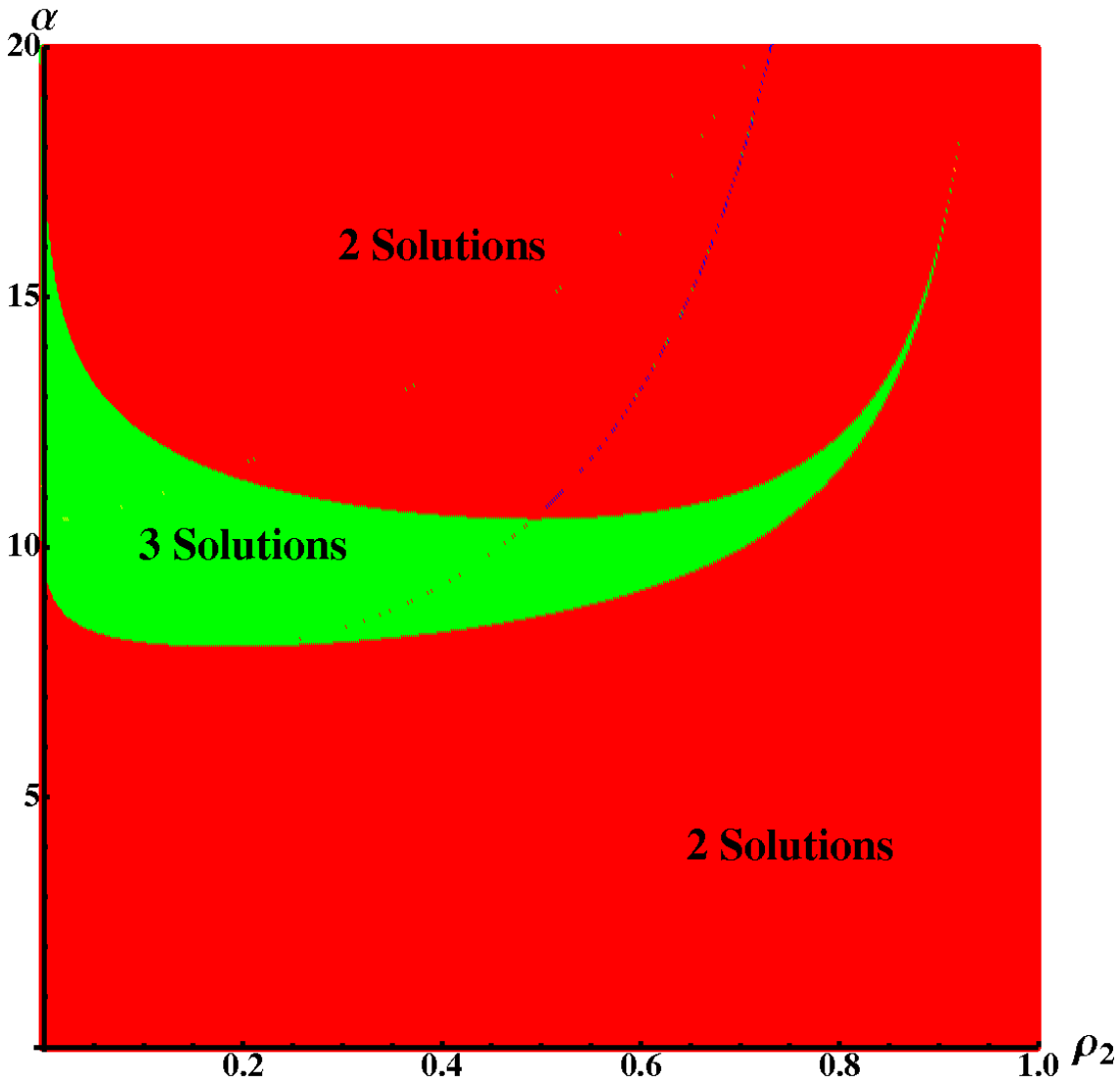

Figure 4.5: Cross section of parameter space of nonlinear model where $\rho_1 = 0.75$. The vertical axis is the parameter $\alpha = \hat{\alpha}_{\rm nl} = u_0\rho_*/\kappa_\rho^2 T$ (Eq. (4.6)), and the horizontal axis is ρ_2. Black corresponds to no solutions, blue corresponds to one solution, red corresponds to two solutions, and green corresponds to three solutions present for the parameter set.

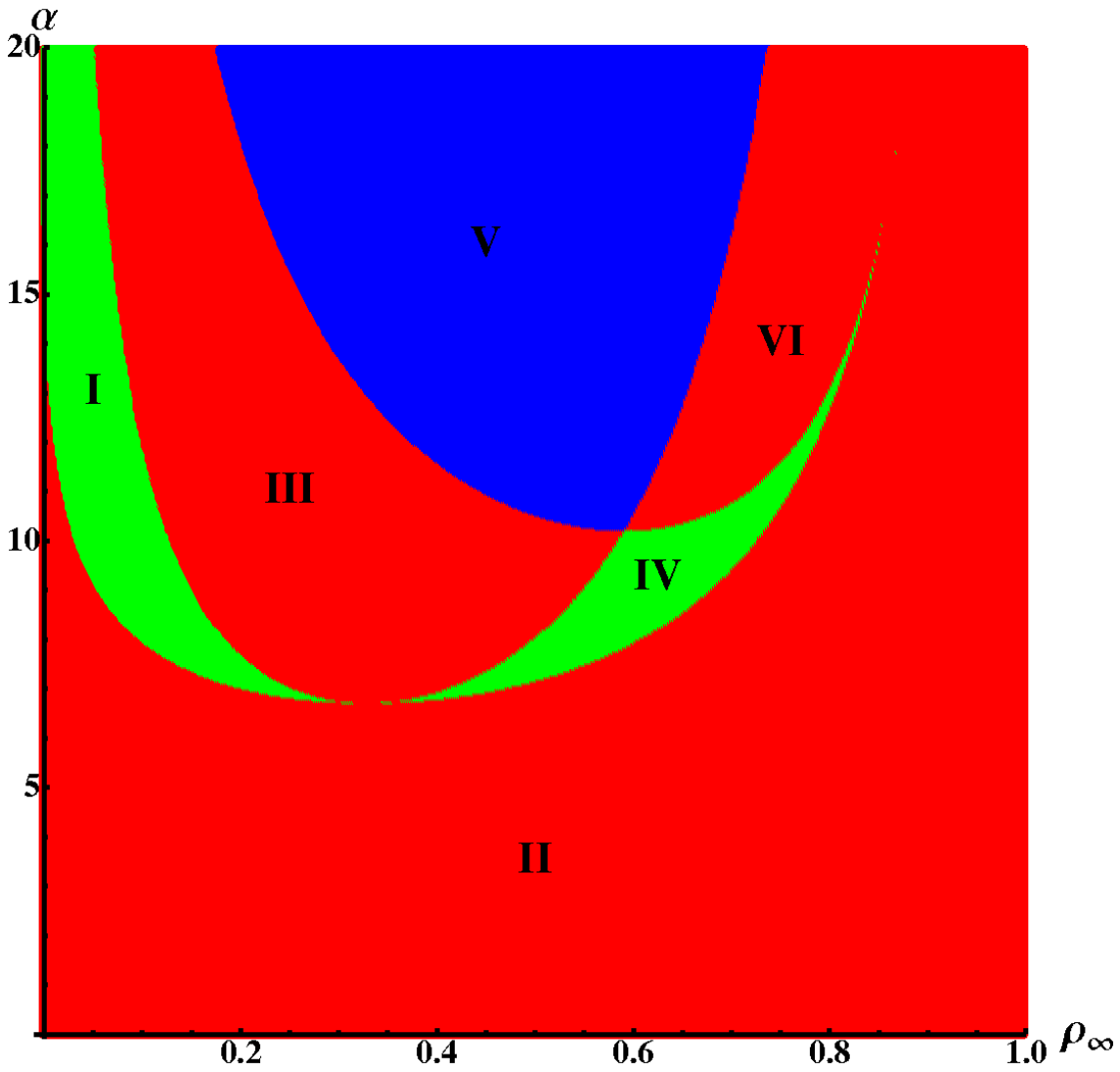

Figure 4.6: Cross section of parameter space of nonlinear model where $\rho_1 = \rho_2 = \rho_\infty$. The vertical axis is the parameter $\alpha = \hat{\alpha}_{\rm nl} = u_0\rho_*/\kappa_\rho^2 T$ (Eq. (4.6)), and the horizontal axis is ρ_∞. Black corresponds to no solutions, blue corresponds to one solution, red corresponds to two solutions, and green corresponds to three solutions present for the parameter set. Regions I-VI are labeled for identification purposes.

we analyze this special case. Examples of the potentials and the corresponding equilibria for each region of parameter space can be seen in Figs. 4.7 and 4.8. The only type of solution not found in this parameter space is the **cc** type. That case will be treated shortly.

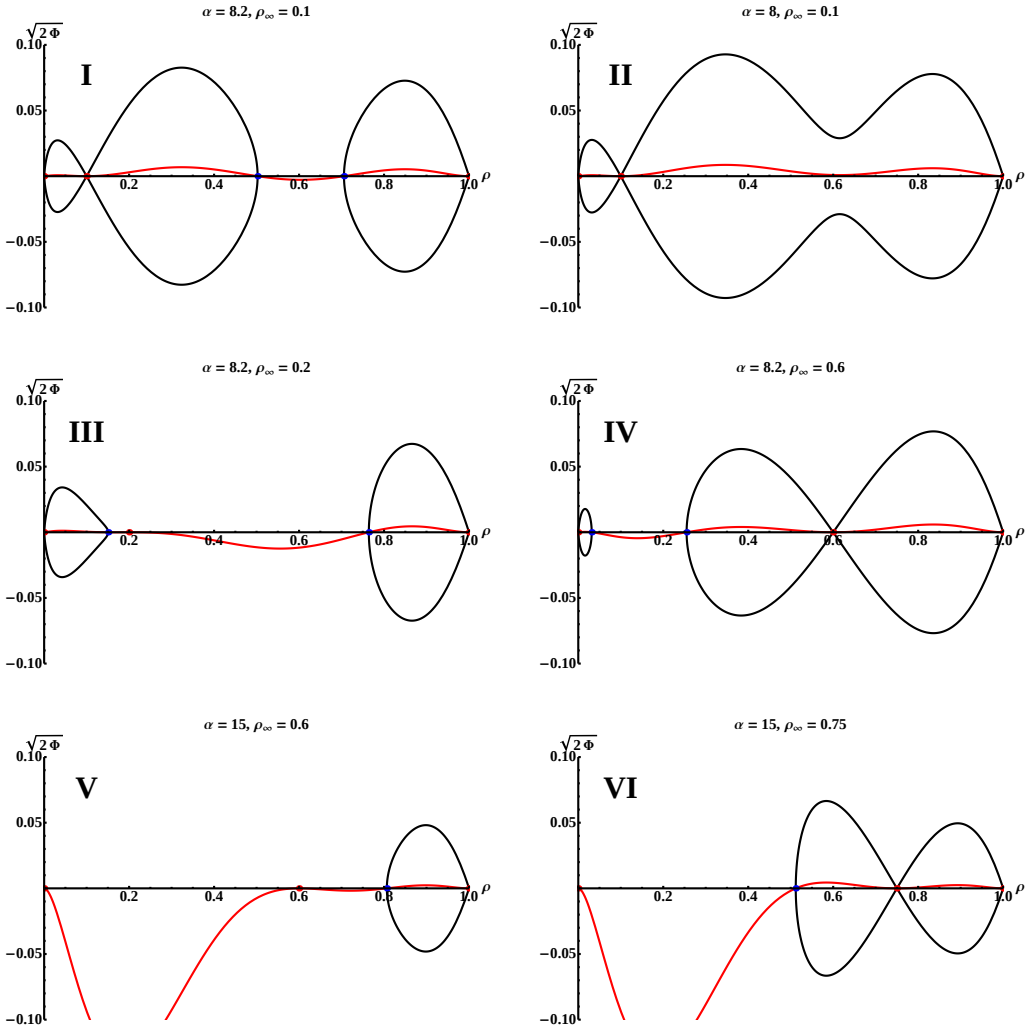

Figure 4.7: Plots of representative potentials $\sqrt{2\Phi}$, (black curves), and Φ, (red curves), for the regions of nonlinear model parameter space identified in Fig. 4.6. The potentials within a single region are fundamentally the same in that they produce similar solution types.

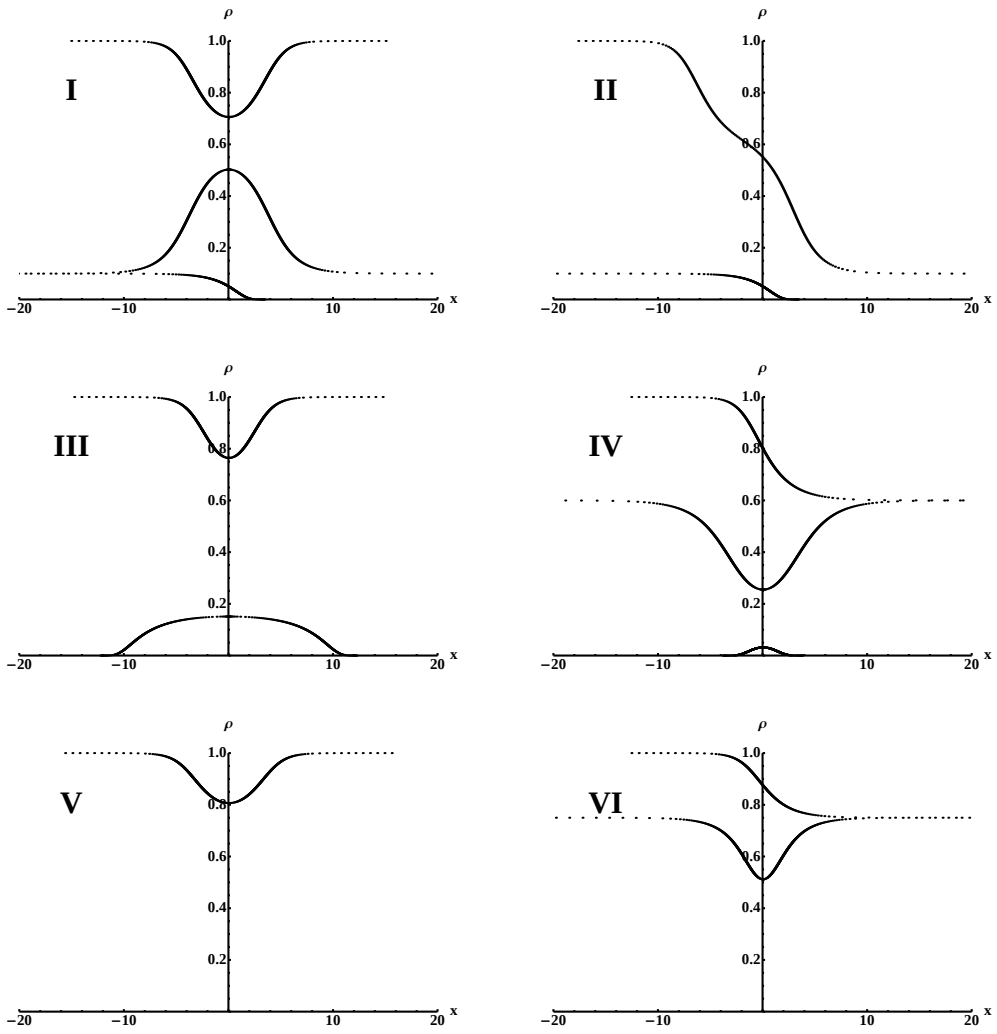

Figure 4.8: Plots of solutions for the potentials in the nonlinear case in Fig. 4.7. This shows which solutions are possible within the regions labeled in Fig. 4.6.

For each root of $\Phi_{\rm nl}$, including $\rho = 0$ and $\rho = 1$, we must determine if it is convergent or divergent. Recall that we fix one double root at ρ_∞. One way to check divergence is to find Taylor series near those roots. If this cannot be done, asymptotic expansions are used. We can do this analytically for the whole phase space for the case of $\rho = 0$, $\rho = \rho_\infty$, and $\rho = 1$. All are divergent points, and we list these expansions below.

The reciprocal of the integrand in Eq. (4.41) near 0, ρ_∞, and 1 behave like

$$\sqrt{2\Phi_{\rm nl}(\delta\rho)} \sim \sqrt{2\left[\frac{\alpha\rho_\infty}{1-\rho_\infty} - \frac{\alpha^2\rho_\infty^2}{1} + \frac{1}{2}\left(\frac{\rho_\infty(\alpha - 1 - \alpha\rho_\infty)}{1-\rho_\infty} + \log\frac{(1-\rho_\infty)\delta\rho}{\rho_\infty}\right)^2\right]}\,\delta\rho \tag{4.52}$$

$$\sqrt{2\Phi_{\rm nl}(\rho_\infty + \delta\rho)} \sim \sqrt{1 - \alpha\rho_\infty + 2\alpha\rho_\infty^2 - \alpha\rho_\infty^3}\,\delta\rho \tag{4.53}$$

$$\sqrt{2\Phi_{\rm nl}(1 - \delta\rho)} \sim -\delta\rho, \tag{4.54}$$

where $\delta\rho$ is a small quantity. The endpoints other than these three endpoints are found to be convergent roots. Using an asymptotic expansions of $\sqrt{2\Phi}$ given numerically by the well- ordered scale functions $\phi_n = (\rho - \rho_c)^{n/2}$, we find that at these points

$$\sqrt{2\Phi_{\rm nl}(\rho_c - \delta\rho)} \sim a_1(\delta\rho)^{1/2} + a_2(\delta\rho)^{2/2} + a_3(\delta\rho)^{3/2} + \cdots, \tag{4.55}$$

where ρ_c is the root found by numerically solving $\Phi_{\rm nl}(\rho) = 0$ near ρ_c. The numerical scheme to find the coefficients was that given by [18]. This asymptotic expansion ensures that the integral of the reciprocal of $\sqrt{2\Phi_{\rm nl}(\rho)}$ in Eq. (4.41) will converge, and thus the endpoints are convergent.

The only type of solution not found in this special case is **cc**. This is the

case where two convergent endpoints are the bounds of the integral in Eq. (4.41). An example of this type of behaviour can be found in the fully three dimensional parameter space. For an example of this, see Fig. 4.9.

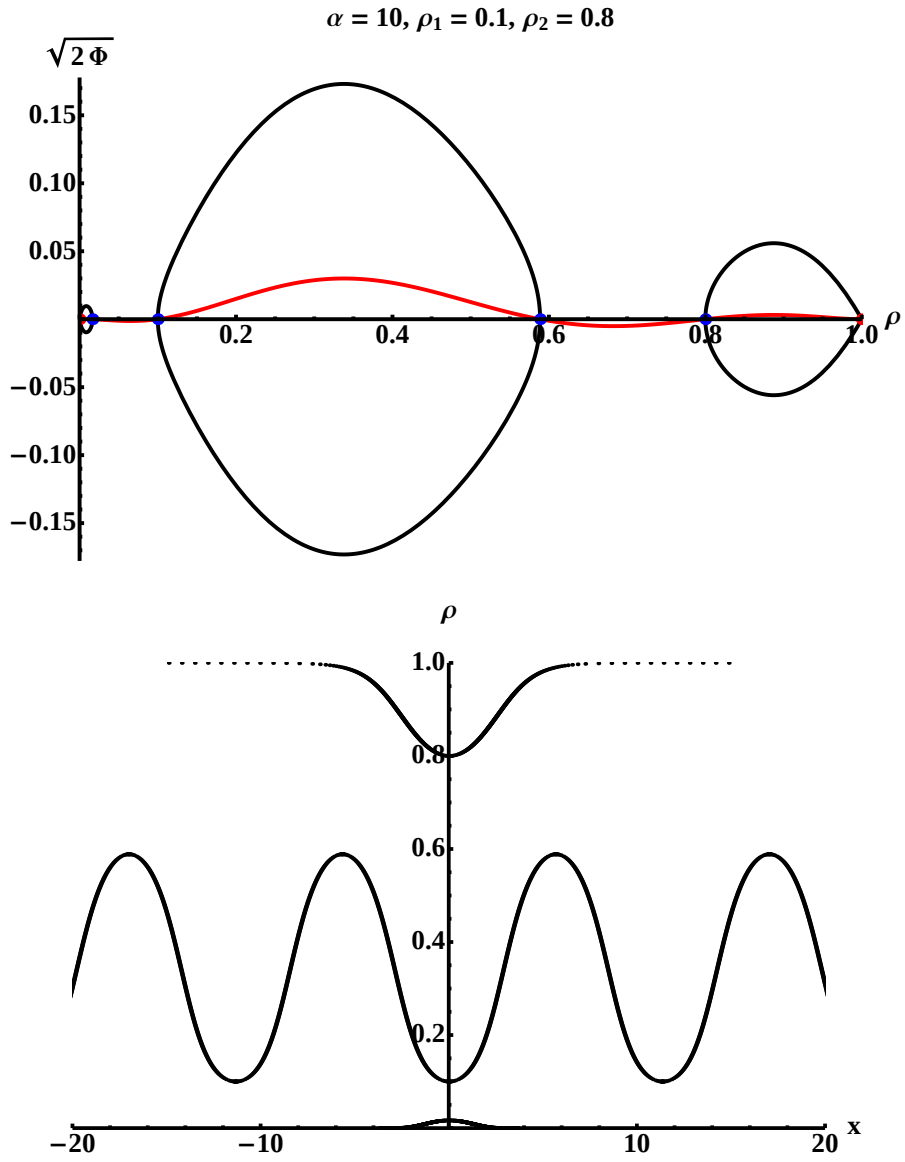

Figure 4.9: A graph of the potential $\sqrt{2\Phi}$ (black curve), Φ (red curve), and corresponding solution for $\alpha = \hat{\alpha}_1 = 2u_{a0}\kappa_r^2/u_{r0}\kappa_a^2 = 10$ (Eq. (4.20)), $\rho_1 = 0.1$, and $\rho_2 = 0.8$. This illustrates the wave-type solution in the nonlinear model.

4.4 Linear Pressure with a Repulsive Potential

Plugging Eq. (4.21) directly into the general procedure from above gives

$$\Phi_{\rm l}(\rho;\alpha,\rho_1,\rho_2)=\frac{\left[\left(U_\rho(\rho)+C_1(\rho_1,\rho_2)\right)^2/2-\alpha(\rho+\rho^2)+C_2(\rho_1,\rho_2)\right]\rho^2}{(1+2\rho)^2}, \tag{4.56}$$

with

$$U_\rho(\rho)=-\int^\rho\frac{1}{\rho}\frac{dP_{\rm l}}{d\rho}d\rho=-\left(\log\rho+2\rho\right), \tag{4.57}$$

where we have dropped the $\tilde{}$'s, and all quantities are dimensionless. Examples of this potential, $\Phi_{\rm l}$, for various parameters (α, ρ_1, and ρ_2) can be seen in Fig. 4.10.

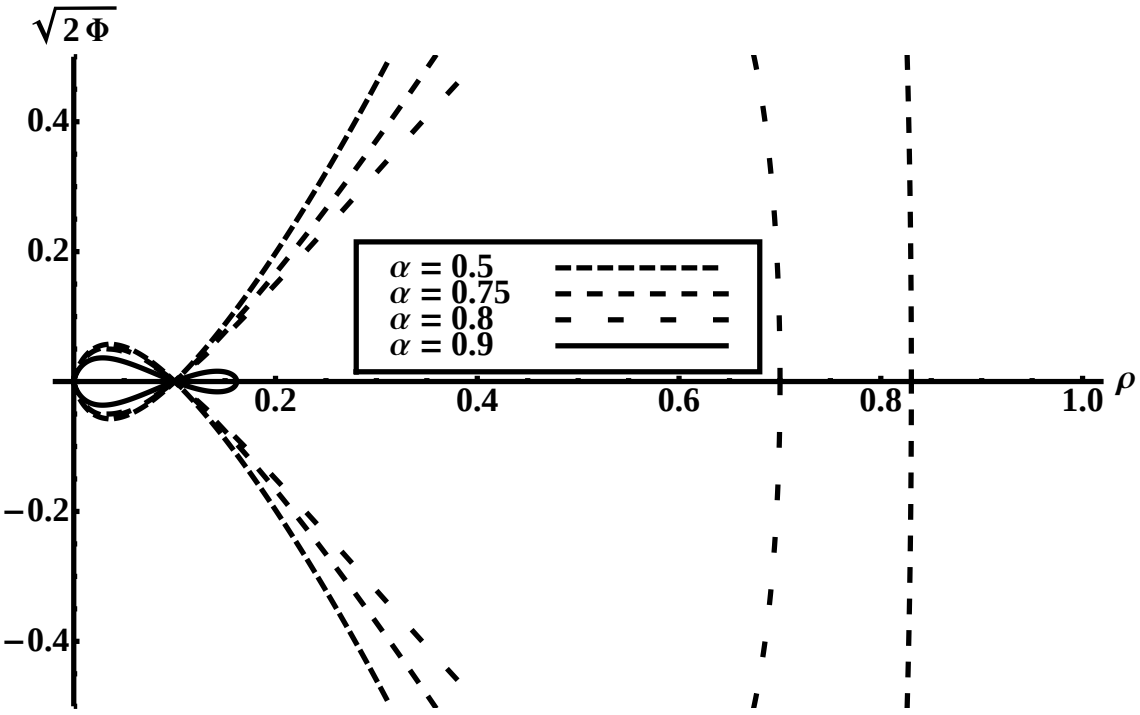

Figure 4.10: This shows several valid potentials, $\sqrt{2\Phi}$, for the linear pressure case where $\rho_1=\rho_2=\rho_\infty=0.1$ for various $\alpha=\hat{\alpha}_{\rm l}=2u_{a0}\kappa_r^2/u_{r0}\kappa_a^2$ (Eq. (4.20)). Because the parameters α and ρ_∞ are unbounded, the plots are compressed according to $\alpha=\tan(\pi/2\ \alpha)$ and $\rho_\infty=\tan(\pi/2\ \rho_\infty)$ to force a range between 0 and 1 for both parameters.

We use the same restriction as the nonlinear model and pick $\rho_1 = \rho_2 = \rho_\infty$ to illustrate the solutions of the linear pressure model. The parameter space, Fig. 4.11, is a lot less complicated than the nonlinear case, and examples of the solutions from these regions can be seen in Fig. 4.12. Since low temperature corresponds to the upper-right side of Fig. 4.11, the black region, corresponding to the region with no solutions, is consistent with the boundary of Region II and Region IV of Fig. 3.3. Additionally, the solutions obtained in the blue region (region B of Fig. 4.11) corresponding to one solution type are those found in Chapter 3 for the zero-temperature correspondence. Note that solutions similar to the nonlinear case are found in the linear model. In the next section, we compare parameter regions where the solutions match. If we relax the restriction that $\rho_1 = \rho_2 = \rho_\infty$, the wave-type solutions are also seen (see Fig. 4.13).

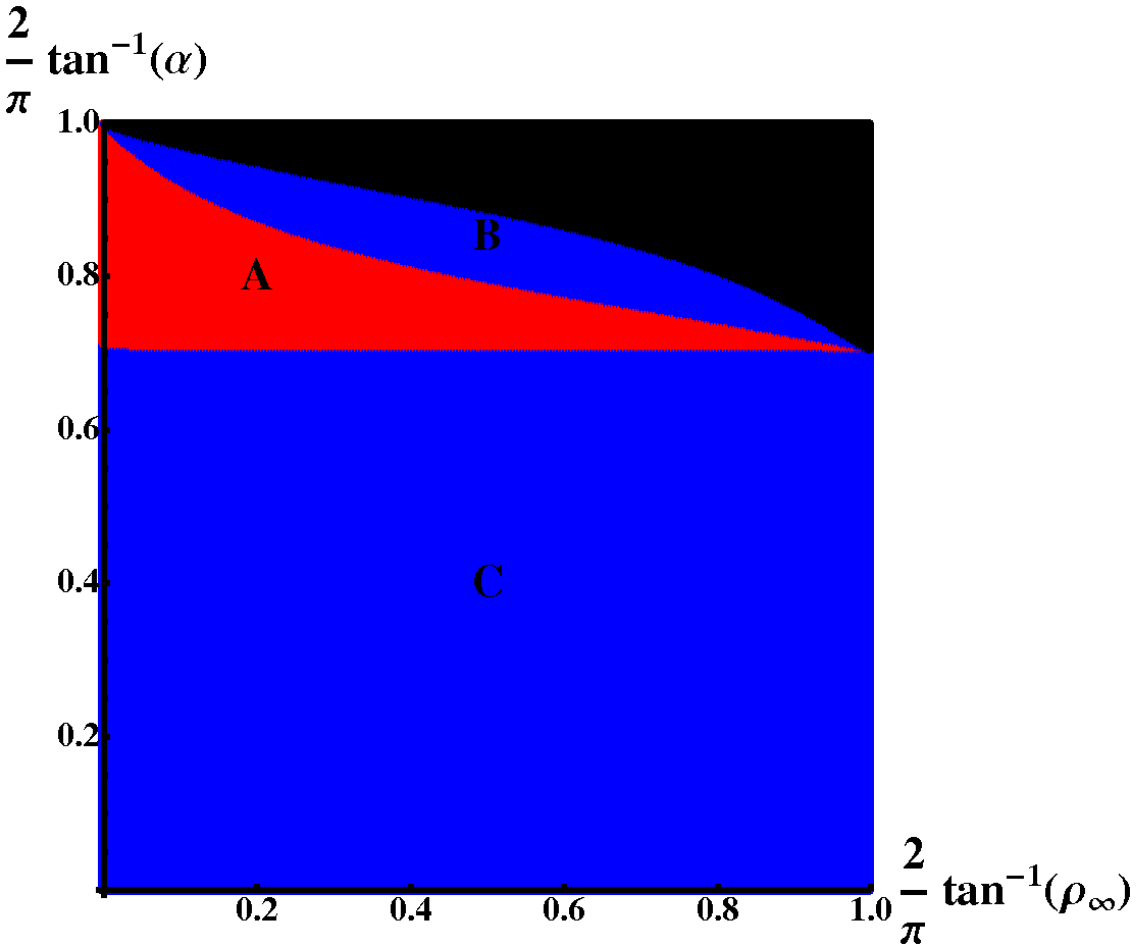

Figure 4.11: Cross section of parameter space of the linear model where $\rho_1 = \rho_2 = \rho_\infty$. The vertical axis is the parameter $(2/\pi)\arctan(\alpha)$, and the horizontal axis is $(2/\pi)\arctan(\rho_\infty)$. Black corresponds to no solutions, blue corresponds to one solution, red corresponds to two solutions. Additionally, labels A-C are included to identify the regions of parameter space. Here, $\alpha = \hat{\alpha}_1 = 2u_{a0}\kappa_r^2/u_{r0}\kappa_a^2$ (Eq. (4.20))

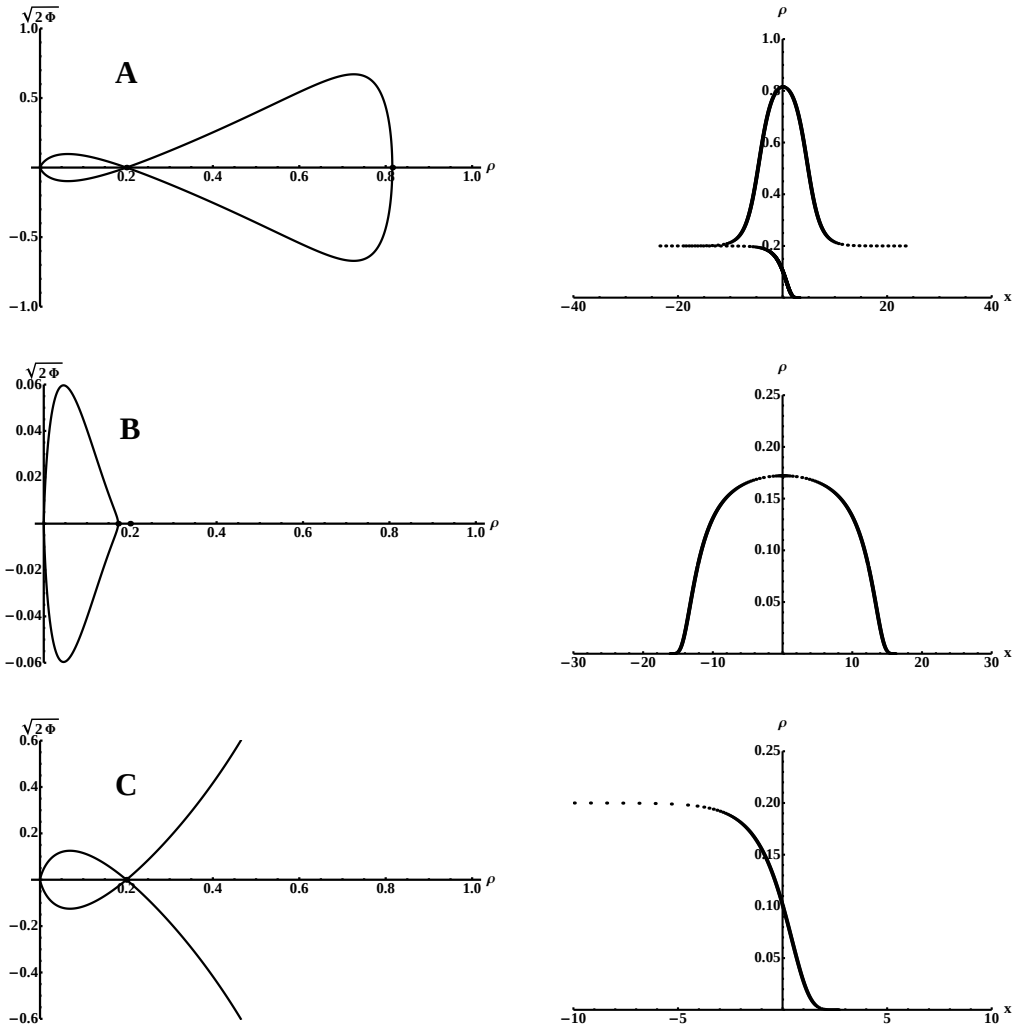

Figure 4.12: Plot the potential $\sqrt{2\Phi_l}$ and equilibrium density solution for several choices of model parameters. A) $\rho_\infty = \tan(\pi/2\ 0.2)$, $\alpha = \tan(\pi/2\ 0.8)$ shows the typical solutions of Region A of Fig. 4.11. B) $\rho_\infty = \tan(\pi/2\ 0.2)$, $\alpha = \tan(\pi/2\ 0.88)$, shows the typical solutions of Region B of Fig. 4.11. C) $\rho_\infty = \tan(\pi/2\ 0.2)$, $\alpha = \tan(\pi/2\ 0.5)$, shows the typical solutions of Region C of Fig. 4.11.

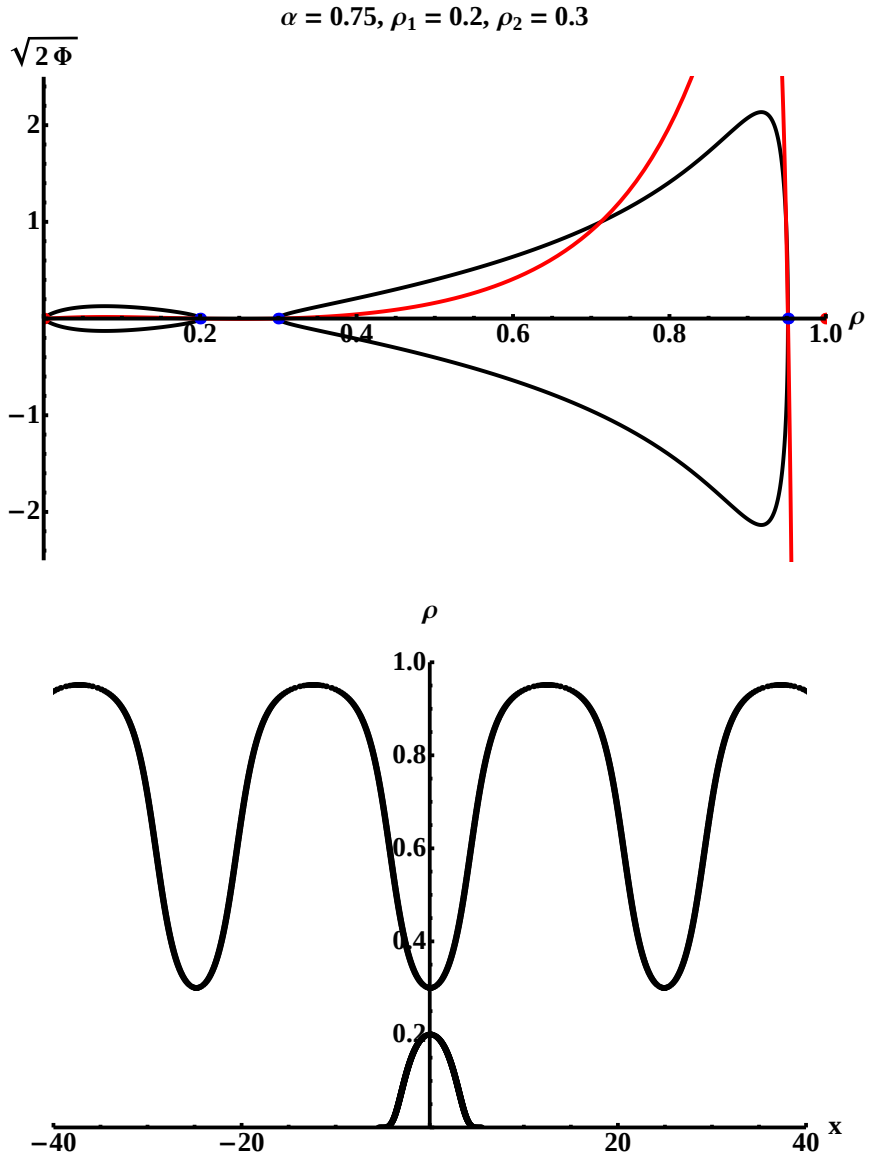

Figure 4.13: A graph of the potential $\sqrt{2\Phi}$ (black curve), Φ (red curve), and corresponding solution for $\alpha = \tan(\pi/2\ 0.75)$, $\rho_1 = \tan(\pi/2\ 0.2)$, and $\rho_2 = \tan(\pi/2\ 0.3)$. This illustrates the existence of the wave-type solution in the linear model.

4.5 Comparison of Nonlinear Model to Linear Model

We would like to compare these two models to see when they produce the same equilibrium. This would tell us when a repulsive potential could act like a pressure term in fluid models of flocking. Here we restrict our attention to the region of phase space where a double root of the potential Φ is labeled by ρ_∞.

If we take the small density limit in the nonlinear case, and compare Eqns. (4.44) and (4.21) in this limit, we see that we need $\rho_* = 2\kappa_r^2 T/u_{r0}$. Additionally, the α parameters are then identical. For this expansion to be valid, all densities for both models must be small with respect to the critical density ρ_* given in the nonlinear model. The potentials Φ_{nl} and Φ_{l} are identical under this expansion to first order.

To obey this expansion, the maximum density must be also small with respect to ρ_*. Figure 4.14 shows the maximum density versus ρ_∞ for several values of α for the nonlinear model. Picking a value for α large enough ensures that for some ρ_∞, we can find a maximum value of $\rho = \rho_0$ small enough to satisfy the condition that all densities must be much smaller than ρ_*. Additionally, large α is consistent with the condition for the derivation of the linear model from Eqns. (4.10) - (4.12), and corresponds to long-range attraction and short-range repulsion.

If we compare both models by keeping the number of flock members, N, fixed, and define N by

$$N \equiv \int_{-\infty}^{\infty} (\rho(x) - \rho_\infty)\, dx, \tag{4.58}$$

where these quantities have dimensions, we see that the models are in agreement

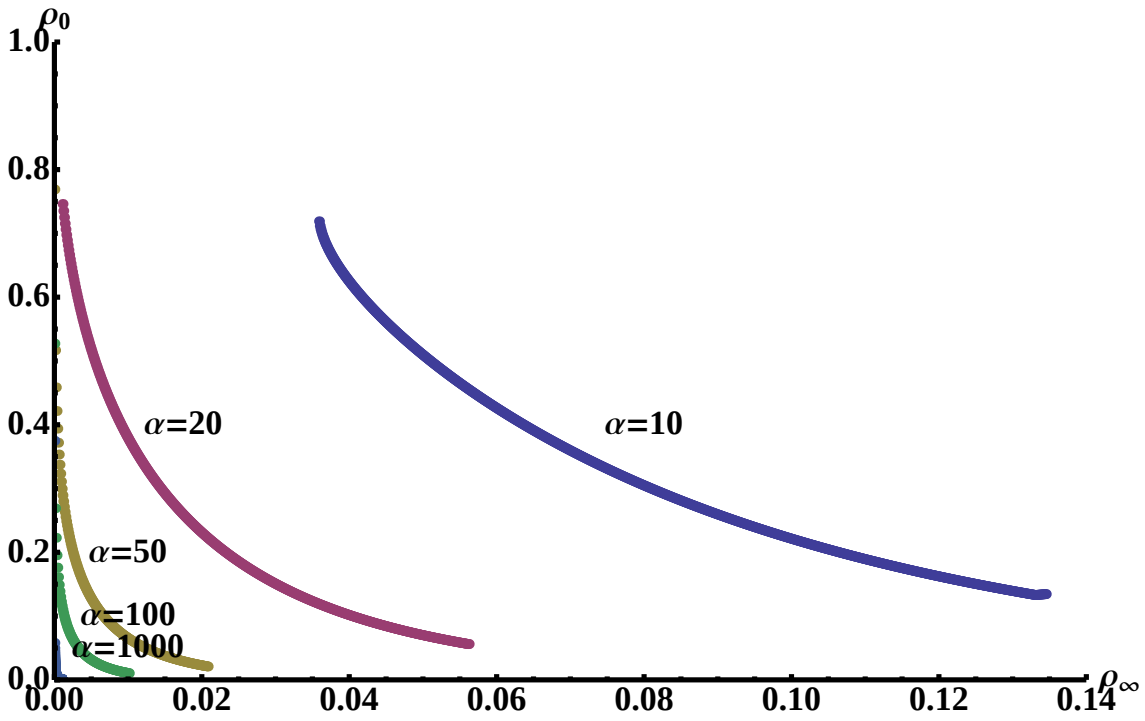

Figure 4.14: Plots of the maximum density vs. the lower density endpoint ρ_∞ for various choices of α in the nonlinear model (Eq. (4.6)).

for large α, small ρ_∞, and $\rho_* = 2\kappa_r^2 T/u_{r0}$. See Fig. 4.15 for an illustration of this comparison.

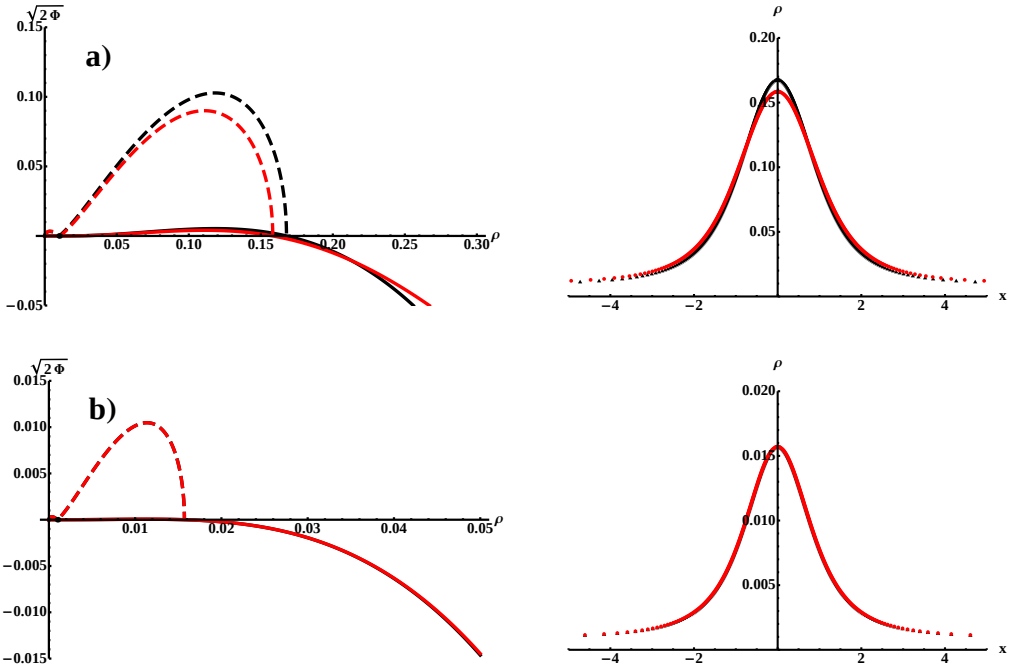

Figure 4.15: Plots of the comparison between the linear and nonlinear model with $\rho_* = 2\kappa_r^2 T/u_{r0}$. a) The number of flock individuals was held fixed, $\alpha = \tan(\pi/2\ 0.98)$. The red curves are nonlinear, the solid curves are Φ, and the dashed curves are $\sqrt{2\Phi}$. b) $\alpha = \tan(\pi/2\ 0.998)$. The red curves are nonlinear. Here, the equilibria are almost identical.

4.6 Conclusion

In this chapter, we describe a procedure for producing an equilibrium density profile for a one-dimensional flock given a differentiable flock pressure. We show that multiple solution types are possible given a fixed set of flock parameters. Two models, a model with a nonlinear pressure and a model with a linear pressure and

a repulsive potential are examined in detail. Parameter spaces for both models are investigated. Conditions for similar solutions correspond to long-range attraction and short-range repulsion (large α). Additionally, in the limit of small densities compared to ρ_* and large α, the models are equivalent. Thus, even though the two models produce different equilibria in general, they produce identical equilibria in the above limiting cases.

Chapter 5

Dispersion of Waves and Stability in Constant and Non-Constant Density Solutions

Here we analyze stability in the full model for flocking introduced in Chapter 2. We use a linear stability analysis to identify stable and unstable constant density solutions. We find that these stability regions depend on the constant density and the parameter α, but are insensitive to the other parameters over several orders of magnitude. The non-constant densities of Chapter 4 are briefly mentioned and contrasted with the constant density solutions.

5.1 Flocking Equations and Constant Density Solution

Starting from basic continuum equations for flocking

$$\frac{\partial \mathbf{v}}{\partial t} + \mathbf{v} \cdot \nabla \mathbf{v} = \frac{1}{\tau}\left(1 - \frac{v^2}{v_0^2}\right)\mathbf{v} - \frac{1}{\rho}\nabla P(\rho) - \nabla U - \mathbf{W}(\mathbf{v}) \tag{5.1}$$

$$\frac{\partial \rho}{\partial t} + \nabla \cdot (\rho \mathbf{v}) = 0, \tag{5.2}$$

with a specific form of the pressure given by

$$P(\rho) = \frac{T\rho}{1 - \rho/\rho_*}, \tag{5.3}$$

we may linearize about an equilibrium to determine the types of waves present from the linear dispersion relation. Here, as in Chapter 2, we choose specific forms for

the attractive potential U and for the velocity viscosity $\mathbf{W}$. We have

$$U = \int u(\mathbf{x}, \mathbf{x}')\rho(\mathbf{x}')d\mathbf{x}' \tag{5.4}$$

$$\mathbf{W} = \int w(\mathbf{x}, \mathbf{x}')(\mathbf{v}' - \mathbf{v})d\mathbf{x}' \tag{5.5}$$

where the kernels u and w satisfy

$$\nabla^2 u - \kappa_\rho^2 u = u_0 \delta(\mathbf{x} - \mathbf{x}') \tag{5.6}$$

$$\nabla^2 w - \kappa_w^2 w = w_0 \delta(\mathbf{x} - \mathbf{x}'). \tag{5.7}$$

5.2 Linear Dispersion with Constant Density Equilibrium

With a constant density solution, we may address the issue of waves propagating through this medium to complete the dispersion analysis started in Chapter 2. If we write the density and velocity near equilibrium as

$$\mathbf{v} = \mathbf{a} + \delta\mathbf{v} \tag{5.8}$$

$$\rho = \rho_0 + \delta\rho, \tag{5.9}$$

where $\mathbf{a}$ is the equilibrium velocity for a constant density solution ($a^2 = v_0^2$), we can substitute this back into the main equations. Doing so, and keeping only the linear terms in the perturbed quantities, we get

$$\frac{\partial}{\partial t}\delta\rho + \nabla \cdot (\rho_0 \delta\mathbf{v}) + \nabla \cdot (\delta\rho\mathbf{a}) = 0 \tag{5.10}$$

$$\frac{\partial}{\partial t}\delta\mathbf{v} + \mathbf{a} \cdot \nabla\delta\mathbf{v} = -\frac{1}{\rho_0}\nabla\delta P - \nabla\delta U - \delta\mathbf{W} - \frac{2\mathbf{a} \cdot \delta\mathbf{v}}{\tau\mathbf{v}_0}\mathbf{a}. \tag{5.11}$$

Where the linearized quantities (δU, $\delta\mathbf{W}$, and δP) are defined as perturbations about their equilibrium quantities similar to the density and velocity perturbations.

Taking a Fourier Transform in space and time gives an expression for the constant-density dispersion relation. Here the Fourier Transforms are defined by

$$\tilde{f}(k) = \mathrm{FT}\left[f(k)\right] = \frac{1}{\sqrt{2\pi}} \int f(x) e^{-ikx} dx \tag{5.12}$$

$$\tilde{g}(\omega) = \mathrm{FT}\left[g(\omega)\right] = \frac{1}{\sqrt{2\pi}} \int g(t) e^{i\omega t} dt \tag{5.13}$$

$$\tag{5.14}$$

where x is a spatial coordinate and t is time. Taking Fourier Transforms of Eqns. (5.3) in all three spatial dimensions, (5.6), and (5.7) give

$$\delta\tilde{P} = \frac{\partial P}{\partial \rho}\delta\tilde{\rho} = \frac{T}{(1-\rho_0/\rho_*)^2}\delta\tilde{\rho} = c_s^2 \delta\tilde{\rho} \tag{5.15}$$

$$\tilde{u} = -\frac{u_0}{(2\pi)^{3/2}\left(k^2+\kappa_\rho^2\right)} \tag{5.16}$$

$$\tilde{w} = -\frac{w_0}{(2\pi)^{3/2}\left(k^2+\kappa_w^2\right)}. \tag{5.17}$$

where $k^2 = k_x^2 + k_y^2 + k_z^2$, and we have defined $c_s^2 = \partial P/\partial\rho$. Using the convolution theorem, we calculate $\delta\tilde{U}$ and $\delta\tilde{\mathbf{W}}$ to give

$$\delta\tilde{U} = (2\pi)^{3/2}\,\tilde{u}\delta\tilde{\rho} \tag{5.18}$$

$$\delta\tilde{W} = \mathrm{FT}\left[\int w(\mathbf{x}-\mathbf{x}')\delta\mathbf{v}(\mathbf{x}')d\mathbf{x}'\right] - \mathrm{FT}\left[\delta\mathbf{v}(\mathbf{x})\int w(\mathbf{x}-\mathbf{x}')d\mathbf{x}'\right] \tag{5.19}$$

$$= (2\pi)^{3/2}\,\tilde{w}(k)\delta\tilde{\mathbf{v}}(\mathbf{k}) - \frac{1}{(2\pi)^{3/2}}\int \delta\tilde{\mathbf{v}}(\mathbf{k}-\mathbf{k}')\mathrm{FT}\left[\int w(\mathbf{x}-\mathbf{x}')\cdot 1 d\mathbf{x}'\right](\mathbf{k}')d\mathbf{k}'$$

$$\tag{5.20}$$

$$= (2\pi)^{3/2}\,\tilde{w}(k)\delta\tilde{\mathbf{v}}(\mathbf{k}) - (2\pi)^{3/2}\int \delta\tilde{\mathbf{v}}(\mathbf{k}-\mathbf{k}')\tilde{w}(\mathbf{k}')\delta(\mathbf{k}')d\mathbf{k}' \tag{5.21}$$

$$= (2\pi)^{3/2}\left(\tilde{w}(k)-\tilde{w}(0)\right)\delta\mathbf{v}(\mathbf{k}) = \nu_w(k)\delta\mathbf{v}(\mathbf{k}), \tag{5.22}$$

where

$$\nu_w(k) = (2\pi)^{3/2}\left(\tilde{w}(k) - \tilde{w}(0)\right) = \left(\frac{w_0}{\kappa_w^2}\right)\frac{k^2}{k^2+\kappa_w^2}, \tag{5.23}$$

calculated from Eq. (5.17).

Thus we can take a Fourier Transform in space and time of Eqns. (5.10) and (5.10) using our definitions above to give

$$-i\omega\delta\tilde{\rho} + i\mathbf{k}\cdot\delta\tilde{\mathbf{v}}\rho_0 + i\mathbf{k}\cdot\mathbf{a}\delta\tilde{\rho} = 0 \tag{5.24}$$

$$-i\omega\delta\tilde{\mathbf{v}} + i\mathbf{a}\cdot\mathbf{k}\delta\tilde{\mathbf{v}} = -\frac{i\mathbf{k}}{\rho_0}c_s^2\delta\tilde{\rho} - i\mathbf{k}\,(2\pi)^{3/2}\,\tilde{u}(k)\delta\tilde{\rho} - \nu_w(k)\delta\tilde{\mathbf{v}} - \frac{2\mathbf{a}\cdot\delta\tilde{\mathbf{v}}}{\tau v_0^2}\mathbf{a}. \tag{5.25}$$

The dispersion relation for waves within this medium satisfy these equations. We may solve for an single equation that defines $\omega(k)$ implicitly as follows. For notational ease, we define the following function of k

$$\bar{c}^2(k) = c_s^2 + (2\pi)^{3/2}\,\tilde{u}(k)\rho_0. \tag{5.26}$$

We dot Eq. (5.25) with the vectors $\mathbf{a}$, $\mathbf{k}$, and $\mathbf{k}\times\mathbf{a}$ to get a total of four scalar equations

$$\frac{\delta\tilde{\rho}}{\rho_0} = \frac{\mathbf{k}\cdot\delta\tilde{v}}{\omega - \mathbf{k}\cdot\mathbf{a}} \tag{5.27}$$

$$\left(-i\omega + i\mathbf{k}\cdot\mathbf{a}\right)\delta\tilde{\mathbf{v}}\cdot\mathbf{a} = -i\mathbf{k}\cdot\mathbf{a}\bar{c}^2\frac{\delta\tilde{\rho}}{\rho_0} - \nu_w\delta\tilde{\mathbf{v}}\cdot\mathbf{a} - \frac{2\mathbf{a}\cdot\delta\tilde{\mathbf{v}}}{\tau} \tag{5.28}$$

$$\left(-i\omega + i\mathbf{k}\cdot\mathbf{a}\right)\delta\tilde{\mathbf{v}}\cdot\mathbf{k} = -ik^2\bar{c}^2\frac{\delta\tilde{\rho}}{\rho_0} - \nu_w\delta\tilde{\mathbf{v}}\cdot\mathbf{k} - \frac{2\mathbf{a}\cdot\delta\tilde{\mathbf{v}}}{\tau v_0^2}\mathbf{k}\cdot\mathbf{a} \tag{5.29}$$

$$\left(-i\omega + i\mathbf{a}\cdot\mathbf{k}\right)\delta\tilde{\mathbf{v}}\cdot\mathbf{k}\times\mathbf{a} = -\nu_w\delta\tilde{\mathbf{v}}\cdot\mathbf{k}\times\mathbf{a}. \tag{5.30}$$

We solve this system of equations by substitution. From Eqns. (5.27) and (5.28) we get

$$\left[-i\left(\omega - \mathbf{k}\cdot\mathbf{a}\right) + \nu_w + \frac{2}{\tau}\right]\delta\tilde{\mathbf{v}}\cdot\mathbf{a} = -\frac{i\bar{c}^2\mathbf{k}\cdot\mathbf{a}}{\omega - \mathbf{k}\cdot\mathbf{a}}\delta\tilde{\mathbf{v}}\cdot\mathbf{k}, \tag{5.31}$$

and from Eqns. (5.27) and (5.29) we get

$$\left[-i\left(\omega-\mathbf{k}\cdot\mathbf{a}\right)+\nu_w+\frac{i\bar{c}^2k^2}{\omega-\mathbf{k}\cdot\mathbf{a}}\right]\delta\tilde{\mathbf{v}}\cdot\mathbf{k}=-\frac{2\mathbf{k}\cdot\mathbf{a}}{\tau v_0^2}\delta\tilde{\mathbf{v}}\cdot\mathbf{a}. \tag{5.32}$$

Combining these, we get, with some rearrangement,

$$\left[\left(\omega-\mathbf{k}\cdot\mathbf{a}+i\nu_w\right)\left(\omega-\mathbf{k}\cdot\mathbf{a}\right)-k^2\bar{c}^2\right]\left[\omega-\mathbf{k}\cdot\mathbf{a}+i\nu_w+i\frac{2}{\tau}\right]=-\frac{2i\bar{c}^2}{\tau v_0^2}\left(\mathbf{k}\cdot\mathbf{a}\right)^2. \tag{5.33}$$

Along with Eq. (5.30), we have the complete dispersion relation. To find regions of parameter space that are either stable or unstable, it is convenient to write this in a dimensionless form. Here we choose dimensionless quantities, denoted by hats, according to

$$\hat{\mathbf{k}}=\mathbf{k}/\kappa_\rho,\quad \hat{\kappa_w}=\kappa_w/\kappa_\rho,\quad \hat{\omega}=\omega/(u_0\rho_*)^{1/2},\quad \hat{\nu_w}=\hat{\beta}\hat{k}^2/(\hat{k}^2+\hat{\kappa_w}^2), \tag{5.34}$$

$$\hat{\delta\tilde{\rho}}=\delta\tilde{\rho}/\rho_*,\quad \hat{\delta\tilde{\mathbf{v}}}=\delta\tilde{\mathbf{v}}\kappa_\rho/(u_0\rho_*)^{1/2},\quad \hat{\bar{c}}^2=\hat{\Gamma}/\hat{\alpha}-\hat{\rho}_0/(\hat{k}^2+1), \tag{5.35}$$

$$\hat{\alpha}=u_0\rho_*/\kappa_\rho^2T,\quad \hat{\beta}=w_0/\kappa_\rho^2(u_0\rho_*)^{1/2},\quad \hat{\gamma}=2/\tau(u_0\rho_*)^{1/2}, \tag{5.36}$$

$$\hat{\rho}_0=\rho_0/\rho_*,\quad \hat{\Gamma}=1/\left(1-\hat{\rho}_0\right)^2,\quad \hat{v_0}^2=v_0^2\kappa_\rho^2/u_0\rho_*,\quad \hat{\mathbf{a}}=\mathbf{a}\kappa_\rho/(u_0\rho_*)^{1/2}. \tag{5.37}$$

Accordingly, the dispersion relation becomes

$$\left[\left(\omega-\mathbf{k}\cdot\mathbf{a}+i\nu_w\right)\left(\omega-\mathbf{k}\cdot\mathbf{a}\right)-k^2\bar{c}^2\right]\left[\omega-\mathbf{k}\cdot\mathbf{a}+i\nu_w+i\gamma\right]=-i\gamma\frac{\bar{c}^2}{v_0^2}\left(\mathbf{k}\cdot\mathbf{a}\right)^2, \tag{5.38}$$

and

$$\left(\omega-\mathbf{k}\cdot\mathbf{a}+i\nu_w\right)\delta\tilde{\mathbf{v}}\cdot\mathbf{k}\times\mathbf{a}=0 \tag{5.39}$$

where there is a $\hat{}$ on every quantity that has been dropped and that will be implied for the rest of the chapter.

In the frame of the flock ($\omega \to \omega - \mathbf{k}\cdot\mathbf{a}$), we see that the dispersion has a particularly clean looking dispersion relation

$$\left[\left(\omega + i\nu_w\right)\omega - k^2\bar{c}^2\right]\left[\omega + i\nu_w + i\gamma\right] = -i\gamma\frac{\bar{c}^2}{v_0^2}\left(\mathbf{k}\cdot\mathbf{a}\right)^2, \tag{5.40}$$

and

$$\left(\omega + i\nu_w\right)\delta\tilde{\mathbf{v}}\cdot\mathbf{k}\times\mathbf{a} = 0 \tag{5.41}$$

In Figure 5.1 we see examples of this dispersion relation for a choice of dimensionless parameters. Notice that for some k we may have some negative imaginary parts for the frequency. This represents an instability for that wavelength.

By plotting all of the different combinations of α, β, γ, ρ_0, and κ_w, we have a 5 dimensional parameter space. We can set $k_y = k_z = 0$ and restrict our attention to k_x. Low-k stability will be exhibited with or without waves perpendicular to the direction of the flock.

In Figure 5.2, we see a parameter- space plot identifying regions of parameter space where the constant density solution is unstable. The parameter space is almost completely independent of β, and γ, and has the slightest dependence on κ_w. Stability of the constant density solution depends solely on α and ρ_0. This is primarily due to the compressibility of the system changing sign. When $\bar{c}^2 < 0$, we have growing modes. Hence, when

$$\bar{c}^2 = \frac{\Gamma}{\alpha} - \frac{\rho_0}{k^2+1} < 0 \Rightarrow \alpha > \frac{1}{\rho_0(1-\rho_0)^2}, \tag{5.42}$$

we have an instability for some k. This corresponds to a boundary of Fig. 4.6 and is plotted in Fig. 5.3. This indicates that constant densities inside the shaded region are unstable.

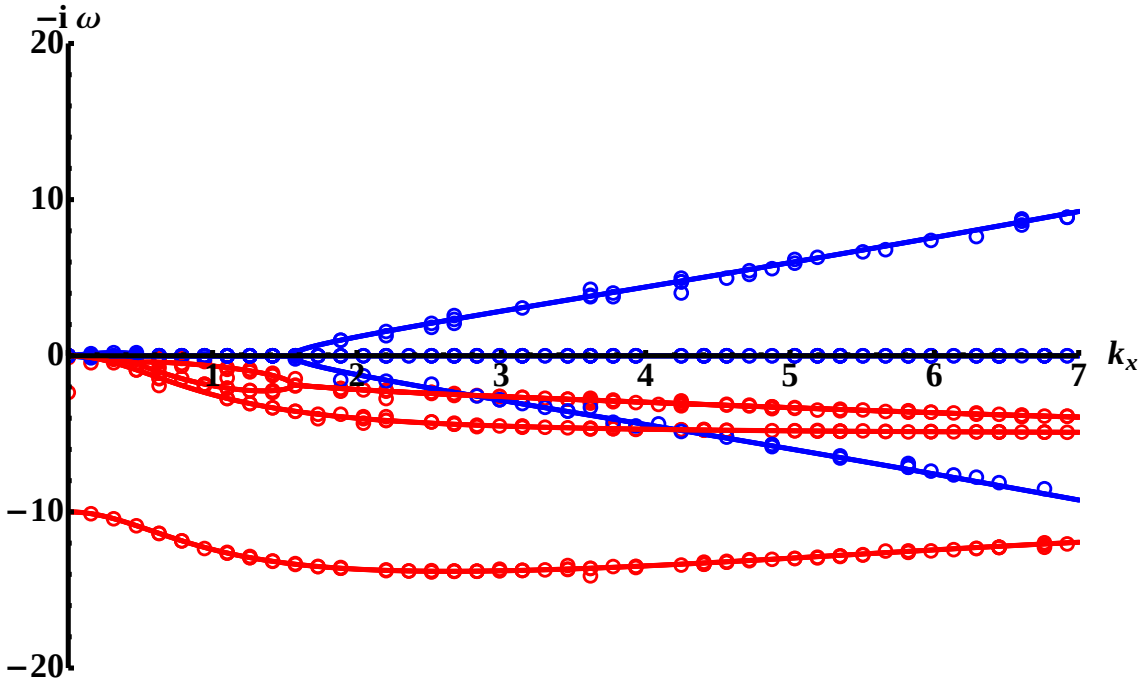

Figure 5.1: The solid curves represent the dimensionless frequency $-i\omega$ as a function of k_x described by Eq. (5.40). Here the circles are the numerical values obtained using the procedure in Appendix G. Red is the real part of $-i\omega$, and blue is the imaginary part of $-i\omega$. The parameters are $\alpha = 10$, $\beta = 5$, $\gamma = 10$, $\kappa_w = 1$, $k_y = k_z = 0$, $a_x = 1$, $a_y = 1$, $\rho_0 = 0.8$, $x_{max} = 20$, $n_x = 801$, using periodic boundary conditions and periodic kernels.

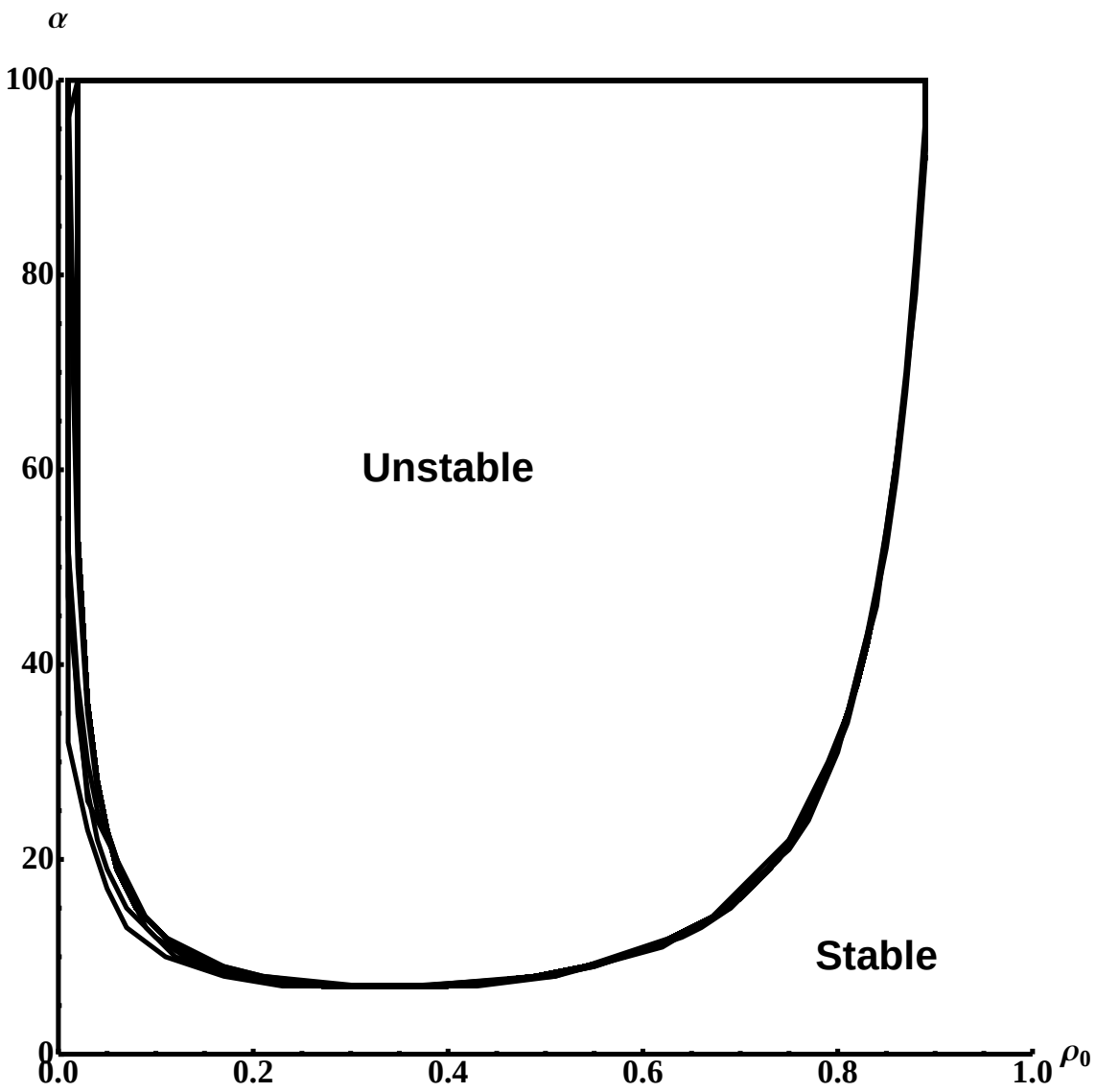

Figure 5.2: A plot of α versus ρ_0 showing the boundary between stability and instability for all combinations of $\kappa_w \in \{0.01, 0.1, 1, 10\}$, $\beta \in \{0.01, 0.1, 1, 10, 100\}$, and $\gamma \in \{0.01, 0.1, 1, 10, 100\}$. The slight variations in the boundary are due to low κ_w (0.01) and high β (10 and 100). The rest of parameter space is virtually independent of β, and γ. Here we have $k_y = k_z = 0$ and $a_x = a_y = 1$.

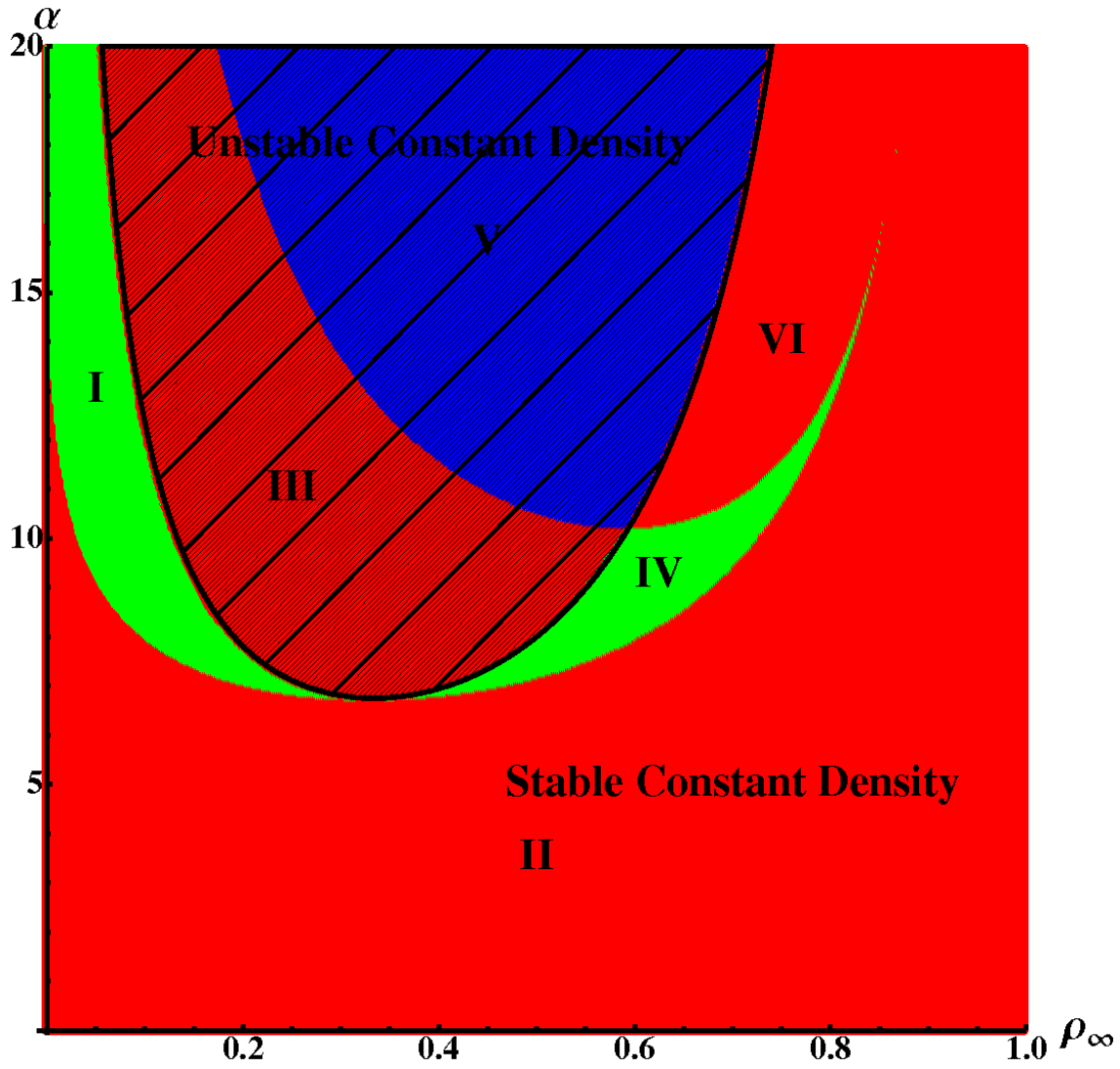

Figure 5.3: A plot of α versus ρ_∞ showing the boundary between stability and instability for constant density solutions on top of the parameter space from Chapter 4. The underlying figure is Fig. 4.6 from Chapter 4. Different colors depict the number of solutions given the parameters α and $\rho_0 = \rho_{\text{inf}}$. Here we have $k_y = k_z = 0$ and $a_x = a_y = 1$.

5.3 Non-Constant Equilibrium Analysis and Stability

Now we are prepared to begin to compare the constant-density theory to the nontrivial solutions found in Chapter 4. For computational simplicity, we again specialize the full equations to a one-dimensional flock so that we may eventually analyze the equilibria of Chapter 4. Accordingly, our picture of a flock is a density profile along the x-direction, and uniform in density along the y and z-directions. This can be visualized as a wall of flocking individuals with the normal vector to the wall is parallel to the x-axis.

If we denote an equilibrium solution as $\rho_0(\mathbf{x})$, and $\mathbf{a}$, we may linearize Eqns. (5.1) and (5.2) around this equilibrium by expressing the physical density and velocity (not dimensionless) as

$$\mathbf{v} = \mathbf{a} + \delta\mathbf{v}(x) \exp\left(-i\omega t + ik_y y + ik_z z\right) \tag{5.43}$$

$$\rho = \rho_0(\mathbf{x}) + \delta\rho(x) \exp\left(-i\omega t + ik_y y + ik_z z\right), \tag{5.44}$$

where we have kept the explicit dependence on the coordinate x out of the expression for the moment. Additionally, a sinusoidal dependence in the y and z directions is attempted. This will test the sensitivity of perturbations along the y and z directions. Using this *ansatz* we plug our expressions back into Eqns. (5.1) and (5.2). Following the analysis in the previous section, we keep only first-order terms.

If we replace the existing dimensional variables with dimensionless variables, we get

$$-i\omega\delta\rho(x) = -\frac{d}{dx}\left(\rho_0(x)\delta v_x(x)\right) - ik_y\rho_0(x)\delta v_y(x) - ik_z\rho_0(x)\delta v_z(x) \tag{5.45}$$

$$\begin{aligned}-i\omega\delta v_x(x) = &-\frac{1}{\rho_0(x)}\frac{d}{dx}\frac{\Gamma(x)}{\alpha}\delta\rho(x) - \frac{d}{dx}U\left[\delta\rho(x)\right] - \beta W_x\left[\delta v_x(x)\right] \\ &- \gamma\frac{a_x}{a_x^2+a_y^2}\left(\mathbf{a}\cdot\delta\mathbf{v}(x)\right) + \frac{1}{\alpha}\frac{\delta\rho(x)}{\rho_0(x)^2}\frac{d}{dx}\left(\frac{\rho_0(x)}{1-\rho_0(x)}\right)\end{aligned} \tag{5.46}$$

$$\begin{aligned}-i\omega\delta v_y(x) = &-ik_y\left(\frac{\Gamma(x)}{\rho_0(x)\alpha}\delta\rho(x) + U\left[\delta\rho(x)\right]\right) - \beta W_y\left[\delta v_y(x)\right] \\ &- \gamma\frac{a_y}{a_x^2+a_y^2}\left(\mathbf{a}\cdot\delta\mathbf{v}(x)\right) + i\frac{k_y}{\alpha}\frac{\delta\rho(x)}{\rho_0(x)(1-\rho_0(x))}\end{aligned} \tag{5.47}$$

$$\begin{aligned}-i\omega\delta v_z(x) = &-ik_z\left(\frac{\Gamma(x)}{\rho_0(x)\alpha}\delta\rho(x) + U\left[\delta\rho(x)\right]\right) - \beta W_z\left[\delta v_z(x)\right] \\ &+ i\frac{k_z}{\alpha}\frac{\delta\rho(x)}{\rho_0(x)(1-\rho_0(x))}\end{aligned} \tag{5.48}$$

Here we have $x = \kappa_\rho x$, in addition to the other dimensionless variables mentioned above in Eqns. (5.34) to (5.37). Additionally, we use the one-dimensional kernels that satisfy Eqns. (5.6) and (5.7), so that the dimensionless U and $\mathbf{W}$ are defined by

$$U\left[\delta\rho\right] = \frac{-1}{2\sqrt{k_y^2+k_z^2+1}}\int_{-\infty}^{\infty} e^{-\sqrt{k_y^2+k_z^2+1}|x-x'|}\delta\rho(x')dx' \tag{5.49}$$

$$\mathbf{W}\left[\delta\mathbf{v}\right] = \frac{-1}{2\sqrt{k_y^2+k_z^2+\kappa_w^2}}\int_{-\infty}^{\infty} e^{-\sqrt{k_y^2+k_z^2+\kappa_w^2}|x-x'|}\left(\delta\mathbf{v}(x') - \delta\mathbf{v}(x)\right)dx'. \tag{5.50}$$

Also note that we have chosen, without loss of generality in these equations, that the equilibrium velocity $\mathbf{a}$ is in the x-y plane.

We would like to investigate the eigenfunctions $\delta\rho(x)$ and $\delta\mathbf{v}(x)$ for stability of various equilibria. To do this, we analyze this set of equations numerically. First, we discretize all functions of x and approximate the derivatives in x by their central difference counterparts. Further, we create an concatenated vector of $\delta\rho(x)$ and

$\delta\mathbf{v}(x)$ of length $4n$ where n is the discretization size,

$$\mathbf{s} = \begin{pmatrix} \delta\rho \\ \delta v_x \\ \delta v_y \\ \delta v_z \end{pmatrix}. \tag{5.51}$$

We can then express Eqns. (5.45) through (5.48) as a matrix eigenvalue equation

$$\mathbf{A}\,\mathbf{s} = -i\omega\,\mathbf{s} \tag{5.52}$$

where $\mathbf{A}$ is the finite-difference approximation to the integro-differential equations Eqns. (5.45) through (5.48), and ω are possible eigenvalues. The explicit form for $\mathbf{A}$ can be seen in Appendix G. We take the boundary conditions to be flux-conserving in the x-direction at the edges of the integration domain. Additionally, we explicitly set δv_y and δv_z to zero at the boundaries of the domain. However, because of the nature of the integral equations in the system, the specific form for the boundary conditions are not important (see Appendix G).

We test the numerical framework with the constant density solution. Here the specific form for the density profile is a constant. We can reconstruct the wave number, k, from the discretized eigenfunctions by taking the discrete Fourier Transform. This will give us a set of ω versus k to compare with the analytical results. The numerical results are plotted along with the analytical work in Fig. 5.1.

Using a specific equilibrium in Chapter 4, Region I, we can in principle identify stable equilibria with this scheme. However, it is not as simple as the constant density solution. For example, if $\kappa_w = 1$, $\beta = 1$, $\gamma = 1$, the most unstable eigenvalue

is numerically found to be $-i\omega = 0.0552$, which represents instability. However, if $\kappa_w = .001$, $\beta = 1$, and $\gamma = 1$, the most unstable eigenvalue is numerically found to be $-i\omega = -4.207 \times 10^{-10}$ which is stable.

5.4 Conclusions

Here we examine the stability of a nonlinear model for flocking. Constant density solutions to the equations are investigated for stability. It is found that only the flock parameters α and the density are important for the determination of stability implying that the main source of instability comes from negative compressibility.

Stability of a non-constant density is more complicated, but both stable and unstable regions exists for a specific equilibrium.

Future work would investigate the correlation of stability in the constant density regions and its predictive power for non-constant density solutions. A further picture for stability of non-constant densities would provide a method for identifying which equilibria are more likely to be found in natural flocks.

Appendix A

Analytic Derivation of Disturbance Characteristics

A.1 Derivation of $\delta\rho/\rho_0$, the Height, and the Width of the Disturbance

We derive the density perturbation $\delta\rho/\rho_0$, the height, $\mathcal{H}$, and the width, $\mathcal{W}$, via a direct computation of the integral Eq. (2.36). To evaluate the integral, we consider the following special case. First, we take $\mathbf{v}_r = \mathbf{v}_0$. This implies that $\psi = 0$. Also, as in the main body of the paper,

$$\bar{c} \approx \lim_{k\to\infty} \bar{c}(k) = c_s, \tag{A.1}$$

$$\nu_w \approx \lim_{k\to\infty} \nu_w(k) = \frac{w_0}{\kappa_w^2}, \tag{A.2}$$

and we define $\epsilon = \nu_w/2\bar{c}$ and $\gamma = v_0/\bar{c}$. With these approximations we can write the integral (2.36) in rectangular coordinates,

$$\frac{\delta\rho(r,\theta)}{\rho_0} = -\frac{\eta_0\pi l^2}{\bar{c}^2\left(2\pi\right)^2}\int_{-\infty}^{\infty} e^{ik_x x}e^{-\frac{l^2}{4}k_x^2}\int_{-\infty}^{\infty}\frac{k_y^2 e^{ik_y y-\frac{l^2}{4}k_y^2}}{k_y^2 - k_x^2\gamma^2 + \frac{i\nu_w\gamma}{\bar{c}}k_x}dk_y dk_x. \tag{A.3}$$

Let us do the k_y integral first. We shift the path of integration up in the complex k_y plane to $\mathrm{Im}(k_y) = i2y/l^2$ so as to go through the saddle point in the complex plane giving,

$$\frac{\delta\rho(r,\theta)}{\rho_0} = -\frac{\eta_0 l^2}{4\bar{c}^2\pi}\int_{-\infty}^{\infty} e^{ik_x x}e^{-\frac{l^2}{4}k_x^2}\left(\int_{-\infty}^{\infty}\frac{\left(u+i\frac{2y}{l^2}\right)^2 e^{-\frac{l^2}{4}u^2}}{\left(u-\hat{u}_1\right)\left(u-\hat{u}_2\right)}du\right)dk_x, \tag{A.4}$$

where the integral is over real u, we have factored the denominator, and we define

$$\hat{u}_1 = -\gamma k_x \sqrt{1 - \frac{i2\epsilon}{\gamma k_x}} - \frac{i2y}{l^2}, \tag{A.5}$$

$$\hat{u}_2 = \gamma k_x \sqrt{1 - \frac{i2\epsilon}{\gamma k_x}} - \frac{i2y}{l^2}. \tag{A.6}$$

Using

$$\int \frac{(u+ia)^2 e^{-b^2u^2}}{(u-u_1)(u-u_2)} du = -\frac{i\pi}{u_1 - u_2} \left[(a - iu_1)^2 w(bu_1) + (a - iu_2)^2 w(-bu_2) \right] + \frac{\sqrt{\pi}}{b} \tag{A.7}$$

along the contour given in Fig. A.1, we can explicitly evaluate the u integral in terms of the complex error function w, given by (see [1])

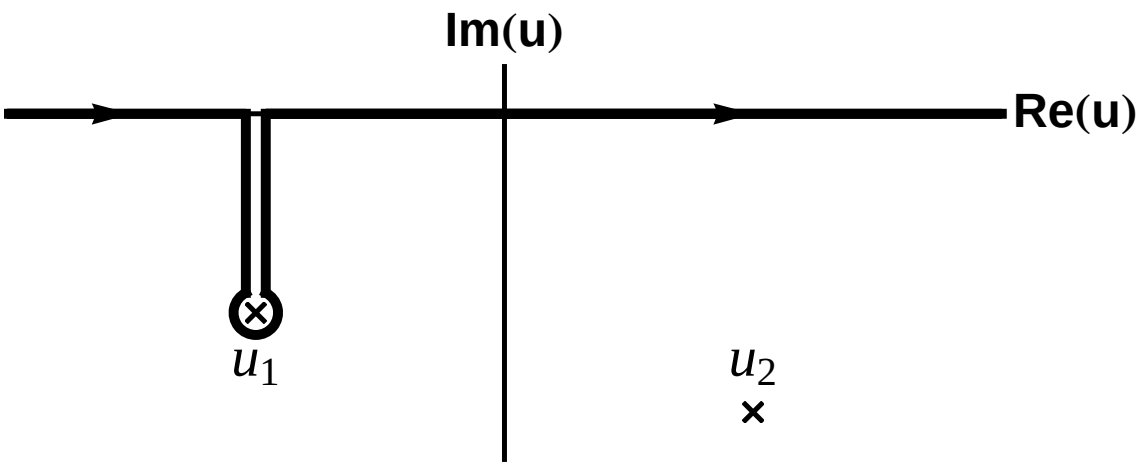

Figure A.1: Contour in the complex plane for the integral in Eq. (A.7). This contour is forced by causality and from $y \to -y$ symmetry.

$$w(z) = \frac{i}{\pi} \int_{-\infty}^{\infty} \frac{e^{-t^2}}{z - t}\, dt = e^{-z^2} \mathrm{erfc}(-iz) \quad \text{if } \mathrm{Im}(z) > 0 \tag{A.8}$$

and defined for the negative imaginary z by analytic continuation.

Expanding Eq. (A.5) and Eq. (A.6) as Taylor series in $(\epsilon/\gamma k_x)$, we obtain from Eq. (A.4)

$$\frac{\delta\rho}{\rho_0} = -\frac{\eta}{\bar{c}^2}e^{-\frac{(x^2+y^2)}{l^2}} + A(x)e^{-B[y-y_0(x)]^2}\left(\int_{-\infty}^{\infty} e^{-w^2} f_+ dw\right) + A(x)e^{-B[y+y_0(x)]^2}\left(\int_{-\infty}^{\infty} e^{-w^2} f_- dw\right) \tag{A.9}$$

where

$$f_\pm(w) = C_\pm(w)\mathrm{erfc}(F_\pm(w)), \tag{A.10}$$

and

$$y_0 = \frac{1}{\gamma}\left(x - \frac{l^2}{2\gamma}\epsilon\right) \tag{A.11}$$

$$A(x) = \frac{\eta_0 l}{4\bar{c}^2\sqrt{1+\gamma^2}}\exp\left[-\frac{\epsilon}{\gamma}(x - \frac{l^2}{4\gamma}\epsilon)\right] \tag{A.12}$$

$$B = \frac{\gamma^2}{(1+\gamma^2)l^2} \tag{A.13}$$

$$C_\pm(w) = i\frac{2\gamma}{l\sqrt{1+\gamma^2}}w - \frac{\gamma(x - \frac{l^2}{2\gamma}\epsilon)}{\frac{l^2}{2}(1+\gamma^2)} \pm \frac{\gamma^2 y}{\frac{l^2}{2}(1+\gamma^2)} \tag{A.14}$$

$$F_\pm(w) = i\frac{\gamma}{\sqrt{1+\gamma^2}}w - \frac{\gamma(x - \frac{l^2}{2\gamma}\epsilon)}{l(1+\gamma^2)} \mp \frac{y}{l(1+\gamma^2)}. \tag{A.15}$$

We now approximate the integral over w using, for example, integration formula 25.4.46 on pg. 890 of [1], to obtain an analytic expression for $\delta\rho/\rho_0$. All non-numerical plots and images are composed via this method (using $n = 10$). We can further use

$$\mathrm{erf}(u+iv) \approx \mathrm{erf}(u) + \frac{e^{-u^2}}{2\pi u}\left[(1-\cos(2uv)) + i\sin(2uv)\right] \approx \mathrm{erf}(u) \tag{A.16}$$

from pg. 299, of the same text, to approximate the integrand. For large enough x, if we change variables and shift the origin in the y direction to the center of the

wedge, y_0, we see that the real part of the argument of the error function is

$$-\frac{y_0(x)}{l} - \frac{\bar{y}}{l(1+\gamma^2)}, \tag{A.17}$$

where $y = y_0 + \bar{y}$. Since for modest values of x this is typically far from zero, the error function is approximately constant and equal to 2. This gives (near the center of the wedge for fixed x)

$$A(x)e^{-B\bar{y}^2}\int_{-\infty}^{\infty} e^{-w^2} f_+(w)dw \approx A(x)e^{-B\bar{y}^2}\frac{4\gamma^2\sqrt{\pi}}{l^2(1+\gamma^2)}(\bar{y}) \tag{A.18}$$

where we have integrated a Gaussian, and neglected the imaginary part, since the final integral must be real. Thus, the height, $\mathcal{H}$ ($\delta\rho/\rho_0$ at maximum), and width, $\mathcal{W}$ (distance between maximum and minimum) defined in Fig. 2.4, are given in the main body of the thesis (Eq. (2.40) and Eq. (2.41)) as

$$\mathcal{H}(x) = \frac{\eta_0\gamma}{\bar{c}^2(1+\gamma^2)}\sqrt{\frac{\pi}{2}}\exp\left[-\frac{1}{2} + \frac{\epsilon^2 l^2 - 4x\gamma\epsilon}{4\gamma^2}\right]$$
$$\mathcal{W} = \frac{2}{\sqrt{2}}\frac{\sqrt{1+\gamma^2}}{\gamma}l.$$

Appendix B

Lambert -W Function

The Lambert-W function, also known as the Product Log function, is defined implicitly as

$$z = W(z)\, e^{W(z)}, \tag{B.1}$$

where z is a complex number, and $W(z)$ is the Lambert-W. Despite its innocuous appearance, the use of the Lambert-W function provides an elegant approach to solving certain classes of transcendental equations in terms of the tabulated $W(z)$.

An expansion for W can be found using Lagrange's Inversion Theorem, stated here because it is so amazing (see for instance [46], this notation from Wikipedia)

Theorem 1 (Lagrange's Inversion Theorem) *[47] Suppose the dependence between the variables w and z is implicitly defined by an equation of the form*

$$f(w) = z,$$

where f is analytic at a point a and $f'(a) \neq 0$. It is possible to invert f to give

$$w = g(z),$$

where g is analytic at the point $b = f(a)$. The series expansion of g is [48]

$$g(z) = a + \sum_{n=1}^{\infty} \frac{d^{n-1}}{dw^{n-1}} \left(\frac{w-a}{f(w)-b} \right)^n \Bigg|_{w=a} \frac{(z-b)^n}{n!}.$$

Accordingly, we can use this to find the series expansion around zero. Here $a = b = 0$, and

$$W(z) = \sum_{n=1}^{\infty} \frac{\mathrm{d}^{n-1}}{\mathrm{d}W^{n-1}} \left(\frac{W}{f(W)} \right)^n \Big|_{W=0} \frac{(z)^n}{n!}.$$

Our f is $f(W) = W\, e^W$, so that $\frac{W}{f(W)} = e^{-W}$. This gives us

$$W(z) = \sum_{n=1}^{\infty} \frac{\mathrm{d}^{n-1}}{\mathrm{d}W^{n-1}} \left(e^{-n\,W} \right) \Big|_{W=0} \frac{(z)^n}{n!}.$$

If we note that the $(n-1)^{\text{st}}$ derivative of $e^{-n\,W}$ is $(-n)^{n-1}\, e^{-n\,W}$, we can finish the expansion. Evaluating at $W = 0$, we get

$$W(z) = \sum_{n=1}^{\infty} (-n)^{n-1} \frac{(z)^n}{n!}.$$

Even though the Lambert-W has a fascinating structure as a multivalued, complex function of a complex variable, for physical purposes I will only consider where the Lambert-W is real valued. The Lambert-W has one real value for real arguments greater than or equal to zero. It has two real values for real arguments in the range $[-1/e, 0)$. In general, however, W is multivalued everywhere in all regions of the complex plane.

An example is in order to show the power of expressing the a problem in terms of the Lambert W. Consider the transcendental equation

$$(ax + b)^n = e^{cx+d}. \tag{B.2}$$

If we can arrange it so that this equation has the same form as Eqn. B.1, we can use the definition to invert the equation, as well as find conditions on when a real root exists. First we take an n^{th} root of both sides and divide through by a,

$$x + \frac{b}{a} = \frac{1}{a} \omega_m \left(e^{cx+d} \right)^{1/n} = \frac{\omega_m}{a} e^{(c/n)x + (d/n)} \tag{B.3}$$

where ω_m is the m^{th} root of unity, $\omega_m = \exp(2im\pi/n)$, where $0 \leq m < n$, and $1/n$ signifies the principle root. If we now rearrange algebraically, we arrive at

$$\left(-\frac{c}{n}x - \frac{cb}{na}\right)\exp\left(-\frac{c}{n}x - \frac{cb}{na}\right) = -\frac{c\omega_m}{na}\exp\left(\frac{d}{n} - \frac{cb}{na}\right). \tag{B.4}$$

The crucial observation here is that we may use the definition of W to express our root. If we identify

$$Y = \left(-\frac{c}{n}x - \frac{cb}{na}\right),$$

we then get the equation

$$Ye^Y = -\frac{c\omega_m}{na}\exp\left(\frac{d}{n} - \frac{cb}{na}\right). \tag{B.5}$$

If we compare with the definition of the Lambert-W, Eqn. (B.1), we see that

$$Y = W[-\frac{c\omega_m}{na}\exp\left(\frac{d}{n} - \frac{cb}{na}\right)] \quad \Rightarrow \quad x = \frac{W[-\frac{c\omega_m}{na}\exp\left(\frac{d}{n} - \frac{cb}{na}\right)] + \frac{cb}{na}}{\frac{-c}{n}}. \tag{B.6}$$

This same technique may be used to solve equations of the form

$$p^{ax+b} = (cx+d)^n$$

using the same basic procedure as above and the fact that

$$p^{ax+b} = e^{\ln p(ax+b)}.$$

Other than these particular uses for solving transcendental algebraic equations, the general spirit of the approach is what I think is important. That a tabulated function can be used as means of finding solutions of transcendental equations is a needed alternative to the standard iterative procedures, especially if there are any undetermined parameters in the problem.

Appendix C

Stability of Constant Density Solutions of Chapter 3

Perturbing Eqns. (3.5) and (3.6) about a constant density, ρ_0, and constant velocity, v_0, according to

$$\rho = \rho_0 + \rho_1 \exp(ikx) \exp(st) \tag{C.1}$$

$$\rho = v_0 + v_1 \exp(ikx) \exp(st), \tag{C.2}$$

we arrive at

$$\rho_0 v_1 s + ikv_1 \rho_0 v_0 = -ik\rho_1 T - \rho_0 ik \left(\frac{u_a \rho_1}{-\kappa_a^2} + \frac{u_r \rho_1}{\kappa_r^2} \right) \tag{C.3}$$

$$\rho_1 s + ik \left(\rho_0 v_1 + \rho_1 v_0 \right) = 0, \tag{C.4}$$

where we have neglected higher-order terms and we have used the long-wavelength approximations for U_a and U_r (from Eqns. (3.3) and (3.4))

$$U_{a,r} = \mp \frac{u_{a,r}}{\kappa_{a,r} + k^2} \rho \approx \mp \frac{u_{a,r}}{\kappa_{a,r}} \rho. \tag{C.5}$$

We eliminate v_1 from Eqns. (C.3) and (C.4), and cancel ρ_1 from the resulting equation to get a quadratic for s

$$s^2 + 2ikv_0 s + k^2 \left[T + \rho_0 \left(\frac{u_r}{\kappa_r^2} - \frac{u_a}{\kappa_a^2} \right) - v_0^2 \right] = 0. \tag{C.6}$$

Solving for s we get

$$s = -ikv_0 \pm k \sqrt{\rho_0 \frac{u_a}{\kappa_a^2} - \left(T + \rho_0 \frac{u_r}{\kappa_r^2} \right)}. \tag{C.7}$$

For an unstable constant-density solution at large wavelengths, the term under the square root symbol is positive. Physically, this corresponds to the attractive potential overcoming the combined repulsive effects of temperature and the repulsive potential. In the case of stability, the square root term yields a real frequency (imaginary contribution to s), and acts similarly to a sound wave. In terms of the dimensionless quantity $\beta_* = \kappa_r^2 u_a / \kappa_a^2 u_r$, the condition for instability is

$$\rho_0 > \frac{T\kappa_r^2}{u_r}\left(\frac{1}{\beta_* - 1}\right) = \rho_c. \tag{C.8}$$

Thus a density above a critical value is unstable. Below that value, the constant density solution is stable to long-wavelength perturbations. Thus, if ρ_0 is too large, according to Eq. (C.8), we expect small inhomogeneities to evolve into growing localized clumps that may be regarded as the early evolution toward the development of flocks. On the other hand, our flock equilibria solutions with finite pressure have $\rho_\infty > 0$, and thus for their stability we require that ρ_∞ not exceed the limit set by Eq. (C.8).

Appendix D

Quadrature of Second Order Ordinary Differential Equations

Given a second-order differential equation

$$\frac{d^2 f(x)}{d^2 x} = g(f(x)), \tag{D.1}$$

we may write the solution via direct integration. Writing the second derivative as a repeated derivative, we get

$$\frac{d}{dx}\frac{df}{dx} = g(f(x)). \tag{D.2}$$

Since

$$\frac{d}{dx} = \frac{df}{dx}\frac{d}{df}, \tag{D.3}$$

we may write Eq. D.1 as

$$\frac{df}{dx}\frac{d}{df}\left(\frac{df}{dx}\right) = g(f). \tag{D.4}$$

Using the chain rule, we may further write this as

$$\frac{d}{df}\left(\frac{1}{2}\left(\frac{df}{dx}\right)^2\right) = g(f), \tag{D.5}$$

which gives

$$\frac{1}{2}\left(\frac{df}{dx}\right)^2 = \int g(f)\, df. \tag{D.6}$$

Appendix E

Numerical Algorithm for Computation of Density Solution

E.1 Cell Stretch Algorithm

The basic equations that we want to solve are Eqns. (3.3), (3.4), and (3.7).

In order to do this, we introduce a fictitious linear friction term into the left-hand side of Eq. (3.7). The velocity is then defined by

$$\nu\, v(x) = -\frac{\partial}{\partial x}\left(U_a(x) + U_r(x)\right) - \frac{T}{\rho(x)}\frac{\partial}{\partial x}\rho(x). \tag{E.1}$$

At equilibrium, the velocity will be zero, and force balance achieved. We solve the fictitious dynamics given by Eqns. (E.1), (3.3), (3.4), and continuity, Eq. (3.5). The algorithm is as follows. Starting with a one-dimensional density profile, we break the domain into a series of equally-spaced "cells", each having a certain amount of area equal to the integral of the density within a cell. During a step in the algorithm, we use the density to update the potentials and velocity according to the above equations. Then, using the updated velocity, the boundary of the cells move according to the velocity. Thus, the boundaries of the cells move to accommodate the new area flowing in or out of the cell. If the velocity is outward from a cell, the area goes down to according to the continuity equation. Once the new boundaries are calculated, continuity is maintained, and the new density is defined. Due to fidelity issues, we could not simply update the density according to this simple formula.

We needed to redistribute the density to its neighbors according to a triangular weighting centered around the current cell. Once a new density is completed, we can now updated the potentials and velocity and continue till an equilibrium is converged upon.

Specifically, the algorithm is

1) Set up discretized potential and redistribution ODEs using second-order central difference with Neumann boundary conditions, and solve for the inverses using LU decomposition ([32])

   a) $-\beta_* \left(\alpha_*^2 \frac{d^2}{d\hat{x}^2} \hat{U}_r(\hat{x}) - \hat{U}_r(\hat{x}) \right) = \hat{\rho}(\hat{x})$

   b) $\frac{d^2}{d\hat{x}^2} \hat{U}_a(\hat{x}) - \hat{U}_a(\hat{x}) = \hat{\rho}(\hat{x})$

   c) $\hat{\rho}_{\text{old}} = \hat{\rho}_{\text{new}} + \alpha_{\text{redist}} D_{\text{trap}} \left(\frac{d^2 \hat{\rho}_{\text{new}}}{d\hat{x}^2} \right)$

2) Update everything for the first time using an unstable constant density initial condition. Determine velocity from a discretized version of Eq. (E.1).

3) For i = 1 to End Condition

   a) Move boundaries using v: $x_{j+1/2} = x_{j+1/2} - \Delta t v_{j+1/2}$

   b) Integrate between old cell walls, and update new density to maintain continuity.

   c) Use back substitution to get new density using triangular redistribution into neighboring cells of some of the density

   d) Update both potentials using back substitution, and update new velocity using the current density

e) Check End Condition

E.2 Parameters

The specific parameters we used were

1. $\Delta t = .0001$
2. number of grid points $= 1000$
3. $\alpha_{\text{redist}} = .99995$
4. $\nu = 10$
5. $x_{\max} = 5$
6. $x_{\min} = 0$
7. $D_{\text{trap}} = \frac{1}{8}$

Appendix F

Fourier Transform Conventions

Here I record conventions for the Fourier Transform and associated identities used in this work.

F.1 Spatial Fourier Transform

The Fourier Transform (FT) of a function $f(x)$ is defined by

$$\mathrm{FT}\left[f(x)\right] = \tilde{f}(k) = \frac{1}{\sqrt{2\pi}} \int_{-\infty}^{\infty} f(x) e^{-ikx} dx. \tag{F.1}$$

Related identities follow from Eq. (F.1). The inverse FT is

$$\mathrm{FT}^{-1}\left[\tilde{f}(k)\right] = f(x) = \frac{1}{\sqrt{2\pi}} \int_{-\infty}^{\infty} \tilde{f}(k) e^{ikx} dk. \tag{F.2}$$

For functions $f(x)$ and $g(x)$, the convolution and the auto-correlation are

$$\left(f * g\right)(x) = \frac{1}{\sqrt{2\pi}} \int_{-\infty}^{\infty} f(x') g(x - x') dx' \tag{F.3}$$

$$\left(f \star g\right)(x) = \frac{1}{\sqrt{2\pi}} \int_{-\infty}^{\infty} f(x')^* g(x + x') dx'. \tag{F.4}$$

where f^* is the complex conjugate of the function f. It follows from the definition of the FT (via the convolution theorem) that

$$\mathrm{FT}\left[f * g\right] = \tilde{f}\tilde{g} \quad \leftrightarrow \quad f * g = \mathrm{FT}^{-1}\left[\tilde{f}\tilde{g}\right] \tag{F.5}$$

$$\mathrm{FT}\left[fg\right] = \tilde{f} * \tilde{g} \quad \leftrightarrow \quad fg = \mathrm{FT}^{-1}\left[\tilde{f} * \tilde{g}\right]. \tag{F.6}$$

Additionally, since

$$f(x) = \frac{1}{2\pi}\int_{-\infty}^{\infty} e^{ikx}\int_{-\infty}^{\infty} e^{-ikx'}f(x')dx'dk = \int_{-\infty}^{\infty} f(x')\left(\frac{1}{2\pi}\int_{-\infty}^{\infty} e^{-ik(x'-x)}dk\right)dx' \tag{F.7}$$

$$\leftrightarrow \delta(x-x') = \frac{1}{2\pi}\int_{-\infty}^{\infty} e^{-ik(x'-x)}dk, \tag{F.8}$$

where $\delta(x-x')$ is a Dirac delta function centered at $x = x'$, we also have that

$$\mathrm{FT}\left[\delta(x)\right] = \frac{1}{\sqrt{2\pi}} \quad \text{and} \quad \mathrm{FT}\left[\frac{1}{\sqrt{2\pi}}\right] = \delta(k). \tag{F.9}$$

Finally, using integration by parts, we get the important relation

$$\mathrm{FT}\left[f'(x)\right] = ik\tilde{f}(k). \tag{F.10}$$

F.2 Temporal Fourier Transform

Similar to the spatial FT, the definition of the FT for a function of time $f(t)$ is defined by

$$\mathrm{FT}\left[f(t)\right] = \tilde{f}(\omega) = \frac{1}{\sqrt{2\pi}}\int_{-\infty}^{\infty} f(t)e^{i\omega t}dt. \tag{F.11}$$

Related identities follow from Eq. (F.11). The inverse FT is

$$\mathrm{FT}^{-1}\left[\tilde{f}(\omega)\right] = f(t) = \frac{1}{\sqrt{2\pi}}\int_{-\infty}^{\infty} \tilde{f}(\omega)e^{-i\omega t}d\omega. \tag{F.12}$$

For functions $f(t)$ and $g(t)$, the convolution and the auto-correlation are identical to their spatial counterparts,

$$\left(f * g\right)(t) = \frac{1}{\sqrt{2\pi}}\int_{-\infty}^{\infty} f(t')g(t-t')dt' \tag{F.13}$$

$$\left(f \star g\right)(t) = \frac{1}{\sqrt{2\pi}}\int_{-\infty}^{\infty} f(t')^* g(t+t')dt'. \tag{F.14}$$

The identities involving the FT of the convolution are unchanged and can be seen in Eqns. (F.5) and (F.6).

We also have

$$f(t) = \frac{1}{2\pi}\int_{-\infty}^{\infty} e^{-i\omega t}\int_{-\infty}^{\infty} e^{i\omega t'} f(t')dt'd\omega = \int_{-\infty}^{\infty} f(t')\left(\frac{1}{2\pi}\int_{-\infty}^{\infty} e^{i\omega(t'-t)}d\omega\right)dt' \tag{F.15}$$

$$\leftrightarrow \delta(t-t') = \frac{1}{2\pi}\int_{-\infty}^{\infty} e^{i\omega(t'-t)}d\omega, \tag{F.16}$$

where $\delta(t-t')$ is a Dirac delta function centered at $t = t'$. From this we also have that

$$\mathrm{FT}\left[\delta(t)\right] = \frac{1}{\sqrt{2\pi}} \quad \text{and} \quad \mathrm{FT}\left[\frac{1}{\sqrt{2\pi}}\right] = \delta(\omega). \tag{F.17}$$

Finally, using integration by parts, we get the important relation

$$\mathrm{FT}\left[f'(t)\right] = -i\omega\tilde{f}(\omega). \tag{F.18}$$

For completeness, we prove the convolution theorem for the case of a two functions $f(t)$ and $g(t)$.

$$\mathrm{FT}\left[f * g\right] = \frac{1}{2\pi}\int_{-\infty}^{\infty}\int_{-\infty}^{\infty} f(t')g(t-t')dt'e^{i\omega t}dt \tag{F.19}$$

$$= \frac{1}{2\pi}\int_{-\infty}^{\infty}\left(\int_{-\infty}^{\infty} g(t-t')e^{i\omega t}dt\right)f(t')dt' \tag{F.20}$$

$$= \frac{1}{\sqrt{2\pi}}\int_{-\infty}^{\infty} f(t')\left(\frac{1}{\sqrt{2\pi}}\int_{-\infty}^{\infty} g(y)e^{i\omega y}dy\right)e^{i\omega t'}dt' = \tilde{f}\tilde{g}. \tag{F.21}$$

For further information please see (for example) [3].

Appendix G

Numerical Procedure for Stability of Equilirium

Using the dispersion relation Eqns. (5.45) through (5.48), we can set up the matrix **A** in Eq. (5.52) using a discretization procedure along the x direction.

If $x_{\max}$ is the position of the boundary along x, we define

$$x_i = -x_{\max} + i\Delta, \quad \text{with} \quad \Delta = \frac{2x_{\max}}{n_x - 1}, \tag{G.1}$$

where n_x is the number of points representing the physical quantities, and Δ is defined for a non-periodic domain (if it were periodic, the spacing would be different with n_x points). Therefore, a function of x is represented within the domain $(-x_{\max}, x_{\max})$ by

$$f(x) \approx f(x_i) = f_i. \tag{G.2}$$

Using the first-order central difference approximation for the derivative, we have the

following definitions:

$$DU_{i,j} = \frac{U_{i+1,j} - U_{i-1,j}}{2} \quad \rightarrow \quad -\frac{d}{dx}U = -\sum_{j=0}^{n_x-1} DU_{i,j}\delta\rho_j, \tag{G.3}$$

$$W_x = \Delta \sum_{j=0}^{n_x-1} W_{i,j}\left(\delta v_{xj} - \delta v_{xi}\right) = \Delta \sum_{j=0}^{n_x-1} W_{i,j}\delta v_{xj} - \delta SW_i \delta v_{xi}, \tag{G.4}$$

$$\text{with} \quad SW_i = \sum_{j=0}^{n_x-1} W_{i,j}, \tag{G.5}$$

$$U_i = \Delta \sum_{j=0}^{n_x-1} U_{i,j}\delta\rho_j, \tag{G.6}$$

$$U_{i,j} = \frac{-1}{2\sqrt{k_y^2 + k_z^2 + 1}} e^{-\sqrt{k_y^2+k_z^2+1}|x_i - x_j|}, \tag{G.7}$$

$$W_{i,j} = \frac{-1}{2\sqrt{k_y^2 + k_z^2 + \kappa_w^2}} e^{-\sqrt{k_y^2+k_z^2+\kappa_w^2}|x_i - x_j|}, \tag{G.8}$$

$$\Gamma_i = \frac{1}{\left(1 - \rho_{0\,i}\right)^2}, \tag{G.9}$$

$$P_{0\,i} = \frac{\rho_{0\,i}}{1 - \rho_{0\,i}}. \tag{G.10}$$

The matrix **A** is then constructed from 16 sub-matrices from Eq. (5.52),

$$-i\omega \begin{pmatrix} \delta\rho \\ \delta v_x \\ \delta v_y \\ \delta v_z \end{pmatrix} = \begin{pmatrix} \text{RR} & \text{RVX} & \text{RVY} & \text{RVZ} \\ \text{VXR} & \text{VXVX} & \text{VXVY} & \text{VXVZ} \\ \text{VYR} & \text{VYVX} & \text{VYVY} & \text{VYVZ} \\ \text{VZR} & \text{VZVX} & \text{VZVY} & \text{VZVZ} \end{pmatrix} \begin{pmatrix} \delta\rho \\ \delta v_x \\ \delta v_y \\ \delta v_z \end{pmatrix}, \tag{G.11}$$

where the sub-matrices are

$$\mathrm{RR}_{i,j} = 0, \quad \mathrm{VXVZ}_{i,j} = 0, \quad \mathrm{VZVX}_{i,j} = 0, \quad \mathrm{VZVY}_{i,j} = 0, \tag{G.12}$$

$$\mathrm{VYVZ}_{i,j} = 0 \quad \mathrm{RVX}_{i,j} = -\frac{1}{2\Delta}\rho_{0\,i+1}\delta_{i+1,j} + \frac{1}{2\Delta}\rho_{0\,i-1}\delta_{i-1,j}, \tag{G.13}$$

$$\mathrm{RVY}_{i,j} = -ik_y\rho_{0\,i}\delta_{i,j}, \quad \mathrm{RVZ}_{i,j} = -ik_z\rho_{0\,i}\delta_{i,j}, \tag{G.14}$$

$$\begin{aligned}\mathrm{VXR}_{i,j} = &-\frac{1}{2\Delta\alpha\rho_{0\,i}}\left(\Gamma_{i+1}\delta_{i+1,j} - \Gamma_{i-1}\delta_{i-1,j}\right) - DU_{i,j} \\ &+ \frac{1}{2\Delta\alpha\rho_{0\,i}^2}\left(P_{0\,i+1}\delta_{i+1,j} - P_{0\,i-1}\delta_{i-1,j}\right),\end{aligned} \tag{G.15}$$

$$\mathrm{VXVX}_{i,j} = -\beta\Delta W_{i,j} + \beta\Delta\, SW_i\delta_{i,j} - \gamma\frac{a_x^2}{a^2}\delta_{i,j}, \tag{G.16}$$

$$\mathrm{VXVY}_{i,j} = -\gamma\frac{a_y a_x}{a^2}\delta_{i,j}, \quad \mathrm{VYVX}_{i,j} = -\gamma\frac{a_x a_y}{a^2}\delta_{i,j}, \tag{G.17}$$

$$\mathrm{VYR}_{i,j} = -\frac{ik_y}{\alpha\rho_{0\,i}}\Gamma_i\delta_{i,j} - i\Delta\, k_y U_{i,j} + \frac{ik_y}{\alpha\rho_{0\,i}^2}P_{0\,i}\delta_{i,j}, \tag{G.18}$$

$$\mathrm{VYVY}_{i,j} = -\beta\Delta\, W_{i,j} + \beta\Delta\, SW_i\delta_{i,j} - \gamma\frac{a_y^2}{a^2}\delta_{i,j}, \tag{G.19}$$

$$\mathrm{VZR}_{i,j} = -\frac{ik_z}{\alpha\rho_{0\,i}}\Gamma_i\delta_{i,j} - ik_z\Delta\, U_{i,j} + \frac{ik_z}{\alpha\rho_{0\,i}^2}P_{0\,i}\delta_{i,j}, \tag{G.20}$$

$$\mathrm{VZVZ}_{i,j} = -\beta\Delta\, W_{i,j} + \beta\Delta\, SW_i\delta_{i,j}. \tag{G.21}$$

Here, $\delta_{i,j}$ is the Kronecker Delta which is 1 if $i = j$, and 0 otherwise. In all sub-matrices both i and j run from 0 to $n_x - 1$. However, on the boundaries 0 and $n_x - 1$, the value of the sub-matrix is set to zero according to the schematic in Fig. G.1. This ensures both zero flux along the x direction, as well enforcing localized perturbation eigenvectors (i.e. the perturbed quantities are going to zero at the boundary). The exact form for the boundary conditions does not affect the eigenvalues for legitimate eigenvectors. For example, if we use the above scheme for a boundary condition, or we replace the 0s with random numbers chosen uniformly between 0 and 1, a random eigenvalue changes only slightly as seen in Fig. G.2. Independent of the boundary

conditions imposed on the matrix, the system will have some symmetric-type eigenvectors and some asymmetric-type eigenvectors. The difficulty arises because of the non-local boundary condition in the underlying problem.

0	0	0	0	0	0	0	0	0	0	0	0	0	0	0	0	0	0	0	0
0	x	x	x	0	x	x	x	x	x	0	x	x	x	0	0	x	x	x	0
0	x	x	x	0	x	x	x	x	x	0	x	x	x	0	0	x	x	x	0
0	x	x	x	0	x	x	x	x	x	0	x	x	x	0	0	x	x	x	0
0	0	0	0	0	0	0	0	0	0	0	0	0	0	0	0	0	0	0	0
0	x	x	x	0	x	x	x	x	x	0	x	x	x	0	0	x	x	x	0
0	x	x	x	0	x	x	x	x	x	0	x	x	x	0	0	x	x	x	0
0	x	x	x	0	x	x	x	x	x	0	x	x	x	0	0	x	x	x	0
0	x	x	x	0	x	x	x	x	x	0	x	x	x	0	0	x	x	x	0
0	x	x	x	0	x	x	x	x	x	0	x	x	x	0	0	x	x	x	0
0	0	0	0	0	0	0	0	0	0	0	0	0	0	0	0	0	0	0	0
0	x	x	x	0	x	x	x	x	x	0	x	x	x	0	0	x	x	x	0
0	x	x	x	0	x	x	x	x	x	0	x	x	x	0	0	x	x	x	0
0	x	x	x	0	x	x	x	x	x	0	x	x	x	0	0	x	x	x	0
0	0	0	0	0	0	0	0	0	0	0	0	0	0	0	0	0	0	0	0
0	0	0	0	0	0	0	0	0	0	0	0	0	0	0	0	0	0	0	0
0	x	x	x	0	x	x	x	x	x	0	x	x	x	0	0	x	x	x	0
0	x	x	x	0	x	x	x	x	x	0	x	x	x	0	0	x	x	x	0
0	x	x	x	0	x	x	x	x	x	0	x	x	x	0	0	x	x	x	0
0	0	0	0	0	0	0	0	0	0	0	0	0	0	0	0	0	0	0	0

Figure G.1: Schematic of the boundary conditions imposed on the matrix **A**. Here shown for $n_x = 5$. The quantities x are those that may be non-zero according to Eqns. (G.12) to (G.21).

Zero BCs **Random BCs**

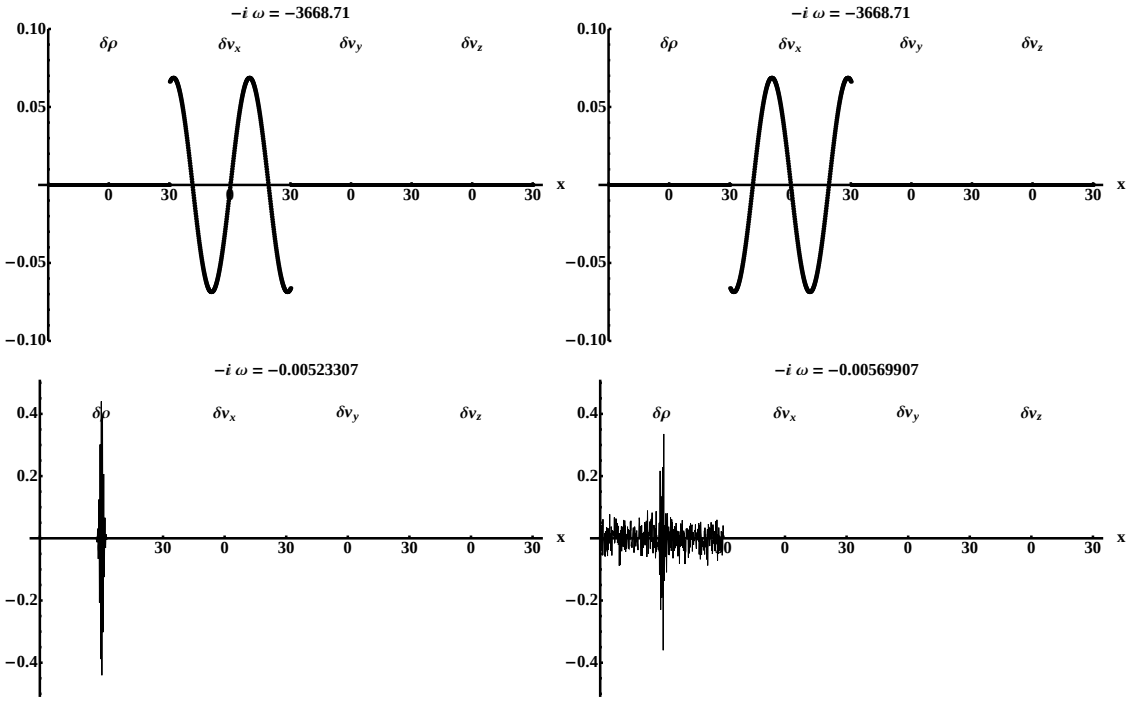

Figure G.2: Calculation of two specific eigenvectors and their corresponding eigenvalues for random boundary conditions and for zero boundary conditions. The parameters are $\alpha = 8.2$, $\beta = 10$, $\gamma = 0$, $\kappa_w = 0.05$, $k_y = k_z = 0$, $a_x = 1$, $a_y = 1$, $\rho_0 = 0.8$, $x_{max} = 30$, $n_x = 401$

Bibliography

[1] Milton Abramowitz and Irene A. Stegun. *Handbook of Mathematical Functions with Formulas, Graphs, and Mathematical Tables*. Dover, New York, ninth dover printing, tenth gpo printing edition, 1964.

[2] R. Aditi Simha and Sriram Ramaswamy. Hydrodynamic fluctuations and instabilities in ordered suspensions of self-propelled particles. *Phys. Rev. Lett.*, 89(5):058101, Jul 2002.

[3] George B. Arfken and Hans J. Weber. *Mathematical Methods For Physicists*. Academic Press, June 2005.

[4] Eshel Ben-Jacob, Inon Cohen, Andrs Czirk, Tams Vicsek, and David L. Gutnick. Chemomodulation of cellular movement, collective formation of vortices by swarming bacteria, and colonial development. *Physica A: Statistical and Theoretical Physics*, 238(1-4):181 – 197, 1997.

[5] C. M. Breder, Jr. Equations descriptive of fish schools and other animal aggregations. *Ecology*, 35(3):361–370, July 1954.

[6] Hsuan-Yi Chen and Kwan-tai Leung. Rotating states of self-propelling particles in two dimensions. *Physical Review E*, 73:056107, 2006.

[7] Iain D. Couzin, Jens Krause, Richard James, Graeme D. Ruxton, and Nigel R. Franks. Collective Memory and Spatial Sorting in Animal Groups. *Journal of Theoretical Biology*, 218:1–11, 2002.

[8] András Czirók, Albert-László Barabási, and Tamás Vicsek. Collective motion of self-propelled particles: Kinetic phase transition in one dimension. *Phys. Rev. Lett.*, 82(1):209–212, Jan 1999.

[9] M. R. D'Orsogna, Y. L. Chuang, A. L. Bertozzi, and L. S. Chayes. Self-Propelled Particles with Soft-Core Interactions: Patterns, Stability, and Collapse. *Physical Review Letters*, 96(10):104302–+, March 2006.

[10] Udo Erdmann and Werner Ebeling. Collective motion of brownian particles with hydrodynamic interactions. *Fluctuation and Noise Letters*, 3(2):L145–L154, 2003.

[11] Udo Erdmann, Werner Ebeling, and Vadim S. Anishchenko. Excitation of rotational modes in two-dimensional systems of driven brownian particles. *Phys. Rev. E*, 65(6):061106, Jun 2002.

[12] Udo Erdmann, Werner Ebeling, and Alexander S. Mikhailov. Noise-induced transition from translational to rotational motion of swarms. *Phys. Rev. E*, 71(5):051904, May 2005.

[13] T. E. Faber. *Fluid dynamics for physicists*. Cambridge University Press, Cambridge, 1995.

[14] Toni Feder. Statistical physics is for the birds. *Physics Today*, 60(10):28–30, 2007.

[15] G. Flierl, D. Grunbaum, S. Levins, and D. Olson. From individuals to aggregations: the interplay between behavior and physics. *Journal of Theoretical Biology*, 196(4):397 – 454, 1999.

[16] V. Gazi and K. M. Passino. Stability analysis of swarms. *Automatic Control, IEEE Transactions on*, 48(4):692–697, 2003.

[17] Dirk Helbing. Traffic and related self-driven many-particle systems. *Rev. Mod. Phys.*, 73(4):1067–1141, Dec 2001.

[18] Mark H. Holmes. *Introduction to Perturbation Methods*. Springer, New York, second printing corrected edition, 1995.

[19] Tien-Ruey Hsiang, Esther M. Arkin, Michael A. Bender, Sandor P. Fekete, and Joseph S.B. Mitchell. *Algorithmic Foundations of Robotics V*, chapter Algorithms for Rapidly Dispersing Robot Swarms in Unknown Environments, pages 77–94. Springer, Berlin / Heidelberg, 2007.

[20] A. Jadbabaie, J. Lin, and A. Morse. Coordination of groups of mobile autonomous agents using nearest neighbor rules, 2002.

[21] V. L. Kulinski, V. I. Ratushnaya, A. V. Zvelindovsky, and D. Bedeaux. Hydrodynamic model for a system of self-propelling particles with conservative kinematic constraints. *Europhys. Lett.*, 71(2):207, 2005.

[22] S.-H. Lee. Predator's attack-induced phase-like transition in prey flock. *Physics Letters A*, 357(4-5):270 – 274, 2006.

[23] S. H. Lee, J. H. Park, T. S. Chon, and H. K. Pak. Prey-flock deformation under a predator's attack. *Journal of the Korean Physical Society*, 48:S236–S240, Feb 2006.

[24] N.E. Leonard and E. Fiorelli. Virtual leaders, artificial potentials and coordinated control of groups. In *Decision and Control, 2001. Proceedings of the 40th IEEE Conference on*, volume 3, pages 2968–2973 vol.3, 2001.

[25] Herbert Levine, Wouter-Jan Rappel, and Inon Cohen. Self-organization in systems of self-propelled particles. *Phys. Rev. E*, 63(1):017101, Dec 2000.

[26] Yao li Chuang, Maria R. D'Orsogna, Daniel Marthaler, Andrea L. Bertozzi, and Lincoln S. Chayes. State transitions and the continuum limit for a 2d interacting, self-propelled particle system. *Physica D: Nonlinear Phenomena*, 232(1):33 – 47, 2007.

[27] Alexander S. Mikhailov and Damián H. Zanette. Noise-induced breakdown of coherent collective motion in swarms. *Phys. Rev. E*, 60(4):4571–4575, Oct 1999.

[28] Peter Miller. Swarm Theory. National Geographic, July 2007.

[29] A. Mogilner, L. Edelstein-Keshet, L. Bent, and A. Spiros. Mutual interactions, potentials, and individual distance in a social aggregation. *Journal of Mathematical Biology*, 47:353–389, 2003.

[30] A. Okubo. Dynamical aspects of animal grouping: swarms, schools, flocks, and herds. *Adv Biophys*, 22:1–94, 1986.

[31] A. Okubo and S. A. Levin. *Diffusion and Ecological Problems*. Springer, New York, 2nd edition, 2001.

[32] William H. Press, Saul A. Teukolsky, William T. Vetterling, and Brian P. Flannery. *Numerical Recipes in C++: The Art of Scientific Computing*. Cambridge University Press, February 2002.

[33] V. I. Ratushnaya, V. L. Kulinski, A. V. Zvelindovsky, and D. Bedeaux. Hydrodynamic model for the system of self propelling particles with conservative kinematic constraints; two dimensional stationary solutions. *Physica A*, 366:107–114, July 2006.

[34] J. W. S. Rayleigh. *The Theory of Sound*, volume 1. MacMillan, London, 2nd edition edition, 1894.

[35] J. Reif and H. Wang. Social potential fields: A distributed behavioral control for autonoomous robots, 1995.

[36] Craig W. Reynolds. Flocks, herds and schools: A distributed behavioral model. In *SIGGRAPH '87: Proceedings of the 14th annual conference on Computer graphics and interactive techniques*, pages 25–34, New York, NY, USA, 1987. ACM.

[37] Naohiko Shimoyama, Ken Sugawara, Tsuyoshi Mizuguchi, Yoshinori Hayakawa, and Masaki Sano. Collective motion in a system of motile elements. *Phys. Rev. Lett.*, 76(20):3870–3873, May 1996.

[38] H. G. Tanner, A. Jadbabaie, and G. J. Pappas. Flocking in fixed and switching networks. *Automatic Control, IEEE Transactions on*, 52(5):863–868, May 2007.

[39] J. Toner, Y. Tu, and S. Ramaswamy. Hydrodynamics and phases of flocks. *Annals of Physics*, 318:170–244, July 2005.

[40] John Toner and Yuhai Tu. Long-range order in a two-dimensional dynamical *xy* model: How birds fly together. *Phys. Rev. Lett.*, 75(23):4326–4329, Dec 1995.

[41] John Toner, Yuhai Tu, and Sriram Ramaswamy. Hydrodynamics and phases of flocks. *Annals of Physics*, 318:170–244, 2005.

[42] Chad M. Topaz and Andrea L. Bertozzi. Swarming patterns in a two-dimensional kinematic model for biological groups. *SIAM Journal on Applied Mathematics*, 65(1):152–174, 2004.

[43] Tamás Vicsek, András Czirók, Eshel Ben-Jacob, Inon Cohen, and Ofer Shochet. Novel type of phase transition in a system of self-driven particles. *Phys. Rev. Lett.*, 75(6):1226–1229, Aug 1995.

[44] Tams Vicsek, Andrs Czirk, Ills J. Farkas, and Dirk Helbing. Application of statistical mechanics to collective motion in biology. *Physica A: Statistical Mechanics and its Applications*, 274(1-2):182 – 189, 1999.

[45] Jürgen Vollmer, Attila Gergely Vegh, Christoph Lange, and Bruno Eckhardt. Vortex formation by active agents as a model for daphnia swarming. *Physical Review E (Statistical, Nonlinear, and Soft Matter Physics)*, 73(6):061924, 2006.

[46] E. T. Whittaker and G. N. Watson. *A Course of Modern Analysis*. Cambridge University Press, fourth edition, 1927. Reprinted 1990.

[47] Wikipedia. Lagrange Inversion Theorem, 2009. [Online; accessed 24-October-2009].

[48] Wikipedia. Lambert W Function, 2009. [Online; accessed 24-October-2009].

[49] M. Zheng, Y. Kashimori, O. Hoshino, K. Fujita, and T. Kambara. Behavior pattern (innate action) of individuals in fish schools generating efficient collective evasion from predation. *Journal of Theoretical Biology*, 235(2):153 – 167, 2005.